ELECTRON TRANSPORT IN MOLECULAR WIRES WITH TRANSITION METAL CONTACTS

by

Hugh Dalgleish

B. Sc., Simon Fraser University
in association with the
University College of the Fraser Valley, 1999

THESIS SUBMITTED IN PARTIAL FULFILLMENT
OF THE REQUIREMENTS FOR THE DEGREE OF
DOCTOR OF PHILOSOPHY
IN THE DEPARTMENT
OF
PHYSICS

SIMON FRASER UNIVERSITY
Summer 2006

APPROVAL

Name: Hugh Dalgleish

Degree: Doctor of Philosophy

Title of Thesis: Electron Transport in Molecular Wires with Transition Metal Contacts

Examining Committee: Dr. I. Herbut (Chair)

Dr. G. Kirczenow (Senior Supervisor)

Dr. R. Hill
Professor, Department of Chemistry, SFU

Dr. B. Johnson
Professor, Department of Physics,
Western Washington University

Dr. M. Kennett
Assistant Professor, Department of Physics, SFU

Dr. S. Ulloa (External Examiner)
Professor, Department of Physics and Astronomy,
Ohio University

Date Approved: August 2, 2006

SIMON FRASER UNIVERSITY library

DECLARATION OF PARTIAL COPYRIGHT LICENCE

The author, whose copyright is declared on the title page of this work, has granted to Simon Fraser University the right to lend this thesis, project or extended essay to users of the Simon Fraser University Library, and to make partial or single copies only for such users or in response to a request from the library of any other university, or other educational institution, on its own behalf or for one of its users.

The author has further granted permission to Simon Fraser University to keep or make a digital copy for use in its circulating collection, and, without changing the content, to translate the thesis/project or extended essays, if technically possible, to any medium or format for the purpose of preservation of the digital work.

The author has further agreed that permission for multiple copying of this work for scholarly purposes may be granted by either the author or the Dean of Graduate Studies.

It is understood that copying or publication of this work for financial gain shall not be allowed without the author's written permission.

Permission for public performance, or limited permission for private scholarly use, of any multimedia materials forming part of this work, may have been granted by the author. This information may be found on the separately catalogued multimedia material and in the signed Partial Copyright Licence.

The original Partial Copyright Licence attesting to these terms, and signed by this author, may be found in the original bound copy of this work, retained in the Simon Fraser University Archive.

Simon Fraser University Library
Burnaby, BC, Canada

Abstract

A molecular wire is an organic molecule that forms a conducting bridge between electronic contacts. Single molecules are likely to be the smallest entities to conduct electricity and thus molecular wires present many interesting challenges to fundamental science as well as enormous potential for nanoelectronic technological applications. A particular challenge stems from the realization that the properties of molecular wires are strongly influenced by the *combined* characteristics of the molecule and the metal contacts. While gold has been the most studied contact material to date, interest in molecular wires with transition metal contacts that are electronically more complex than gold is growing.

This thesis presents a theoretical investigation of electron transport and associated phenomena in molecular wires with transition metal contacts. An appropriate methodology is developed on the basis of Landauer theory and *ab initio* and semi-empirical considerations and new, physically important systems are identified. Spin-dependent transport mechanisms and device characteristics are explored for molecular wires with ferromagnetic iron contacts, systems that have not been considered previously, either theoretically or experimentally. Electron transport between iron point contacts bridged by iron atoms is also investigated. Spin-dependent transport is also studied for molecules bridging nickel contacts and a possible explanation of some experimentally observed phenomena is proposed. A novel physical phenomenon termed *strong spin current rectification* and a new controllable negative differential resistance mechanism with potential applications for molecular electronic technology are introduced. The phenomena predicted in this thesis should be accessible to present day experimental techniques and this work is intended to stimulate experiments directed at observing them.

Keywords: molecular electronics; spintronics; electron transport; interface states.

This thesis is dedicated in memory of my grandfather.

Acknowledgments

I would first like to thank my supervisor George Kirczenow for his invaluable guidance, and for the countless ideas and helpful suggestions he offered during the course of my research. I would also like to thank him for taking an interest in my development, as not only a scientist, but as a professional. I also extend my thanks to supervisory committee members Ross Hill and Brad Johnson for many insightful questions and rewarding discussions.

I also thank my predecessor Eldon Emberly who left behind a beautifully written thesis that has served me nicely as a text on theoretical molecular electronics. My thesis is in many ways an extension of his seminal research.

Next I would like to express my appreciation to the Canadian Institute for Advanced Research (CIAR) for hosting many rewarding meetings and summer schools. I learned much about Nanoelectronics and Nanotechnology, and always returned home with new ideas and enthusiasm for research. I would also like to thank CIAR for taking me on as program reporter and coordinator/chair of the Molecular Electronics Summer School, from which I have gained valuable experience.

I will always be very grateful to my wife Melanie for her endless support, encouragement and understanding. Lastly, I would like to thank the rest of my family for their continual encouragement and support, and for enduring as I talked on (and sometimes on) about my most recent progress and new ideas.

Contents

Approval ii

Abstract iii

Dedication iv

Acknowledgments v

Contents vi

List of Figures ix

1 Introduction 1

2 Electron Transport in Molecular Wires with Transition Metal Contacts 9

2.1 Introduction 9
2.2 Landauer Theory for Calculating Electronic Current in Mesoscopic Systems 10
2.3 Quantum Chemistry and the Many-Body Schrödinger Equation 11
2.4 Density Functional Theory 15
2.5 Extended-Hückel Theory 17
2.6 Tight-binding Formalism for Molecular Wires with Transition Metal Contacts 18
2.7 Modeling Transition Metal Electrodes 20
2.8 Quantum Transport in Molecular Wires with Transition Metal Electrodes . 24
2.9 Finite Bias and the Electrostatic Potential 28
2.10 Mulliken Analysis 30

3 Spin-dependent Transport in Atomic Fe Nanocontacts 31
- 3.1 Introduction 31
- 3.2 Julliére Model for Spin-dependent Transport 34
- 3.3 Tight-binding Model and Applicability to Nanoscale Geometries 36
- 3.4 Fe Nanocontacts Bridged by Fe Atoms in a BCC Nearest-Neighbor Geometry 41
- 3.5 Spin-Dependent Transport for More General Junction Geometries 48
  - 3.5.1 Structural Considerations: Bulk and Relaxed Geometries 48
  - 3.5.2 Generalizing the Tight-Binding Model 49
  - 3.5.3 SDT in Fe Nanocontacts Bridged by Fe Atoms in a Linear Geometry 50
  - 3.5.4 Dependence of Spin Transport on the Separation Between Tip Atoms and Dangling Bond Formation 53
  - 3.5.5 Vacuum Tunneling Between Fe Nanocontacts 56
- 3.6 Conclusions 58

4 Molecular Spintronics: Spin-dependent Transport in Molecular Wires 59
- 4.1 Introduction 59
- 4.2 Modelling the Geometry and Electronic Structure of BDT Molecular Wires 61
  - 4.2.1 Structural Considerations: Atomic Details of the Metal- Molecule Interface 61
  - 4.2.2 Electronic Considerations: Modification of Extended-Hückel 64
- 4.3 Spin-dependent Transport in Molecular Wires with Fe Contacts 67
  - 4.3.1 Conducting Fe-Molecular Wires: BDT 67
  - 4.3.2 Insulating Fe-Molecular Wires: Octane-dithiolate 74
- 4.4 Spin-dependent Transport in Asymmetric Molecular Wires with Ni Contacts 78
- 4.5 Effective Spin Polarizations of Molecular Wires 84
- 4.6 Conclusions 86

5 Interface States, NDR and Rectification in Molecular Wires with Transition Metal Contacts 88
- 5.1 Introduction 88
- 5.2 Interface States in Molecular Wires with Transition Metal Contacts 91
  - 5.2.1 Nature of the Interface State Transmission 91
  - 5.2.2 Evolution as Molecule is Contacted 94

5.2.3 Dependence on Surface Orientation and Binding Site 97
5.2.4 Dependence on Length of the Molecule 99
5.3 Bias-Dependence of Interface State Transmission 100
5.4 Negative Differential Resistance in Molecular Wires with Transition Metal Contacts 105
5.4.1 NDR in Molecular Wires with Symmetric Transition Metal Contacts 105
5.4.2 NDR in Molecular Wires with Asymmetric Transition Metal Contact Materials 107
5.5 Rectification in Molecular Wires with Transition Metal Contacts 113
5.6 Conclusions 115

6 Spin Current Rectification in Molecular Wires 117
6.1 Introduction 117
6.2 Spin Current Rectification in Molecular Wires with Fe Contacts 119
6.2.1 Au/OT/Fe Molecular Wires 119
6.2.2 Au/ODT/Fe and Pd/OT/Fe Molecular Wires 125
6.3 Spin Current Rectification in Molecular Wires with Ni Contacts: Au/OT/Ni 126
6.4 Conclusions 128

7 Summary and Outlook 129

Appendices 132

A Application of Energy Shift for Non-orthogonal Bases 132

B Basis State Orthogonalization by Changing Hilbert Spaces 133

C Green's Functions for Semi-infinite One-dimensional Leads 135

D Factorization of Transmission Functions for Asymmetric Molecular Wires and Effective Spin Polarizations 137

E Two-level Quantum Model of Interface State Transmission 140

Bibliography 143

List of Figures

2.1 Extended molecule: Schematic partitioning of a molecular wire 13
2.2 Energy level diagram for an electron scattering through a molecular wire . . 25

3.1 Bulk and surface densities of states vs. energy for Fe 39
3.2 Calculated magnetic moments per atom for Fe nanoclusters 41
3.3 Extended molecule for an Fe QPC in a BCC nearest-neighbor geometry . . 42
3.4 Spin-dependent transmission for an Fe QPC in a BCC geometry 43
3.5 Currents and magnetoresistance for an Fe QPC in a BCC geometry 45
3.6 Resonant energy level alignment for an Fe QPC under bias 47
3.7 Extended molecule for an Fe QPC in a linear contact geometry 49
3.8 Spin-dependent transport for an Fe QPC in a linear geometry 51
3.9 Spin-dependent transport for an Fe QPC vs. separation of the tip atoms . . . 54
3.10 Spin-dependent transport for vacuum tunneling between Fe nanocontacts . 57

4.1 Optimized geometry of a 1,4 benzene-dithiol molecule 62
4.2 Energy eigenvalue spectrum of isolated 1,4 benzene-dithiol 66
4.3 Extended molecule for a Fe-BDT molecular wire 67
4.4 Spin-dependent transport for an Fe-BDT molecular wire 68
4.5 Representative hybridized energy eigenstates of the Fe-BDT molecular wire under bias 70
4.6 Extended molecule for a Fe-ODT molecular wire 75
4.7 Spin-dependent transport for an Fe-ODT molecular wire 76
4.8 Extended molecule for a Ni-OT molecular wire 79
4.9 Spin-dependent transport for a Ni/OT/Ni molecular wire 80

4.10 Spin-dependent transmission for symmetric Ni-molecular wires 82
4.11 Effective spin polarizations for a Ni/OT/Ni molecular wire 85

5.1 Transmission probability for a Pd/AT4/Pd molecular wire 93
5.2 Transmission probabilities for increasing thiol-Pd contact separation for the Pd/AT4/Pd molecular wire 95
5.3 Transmission probabilities for different AT4 binding sites on (111) Pd contacts 98
5.4 Transmission probabilities as different bias is applied across the Pd/AT4/Pd molecular junction 101
5.5 Energies of interface state resonances vs. bias for Pd/AT4/Pd 102
5.6 Current-voltage characteristic for the Pd/AT4/Pd molecular wire 106
5.7 Transmission probabilities for molecular wires with Rh contacts 108
5.8 Transmission probabilities as different bias is applied across the Pd/AT4/Rh molecular junction 109
5.9 Currents for the Pd/AT4/Rh molecular wire 110
5.10 Energies of interface state resonances vs. bias for Pd/AT4/Rh 111
5.11 Calculated current-voltage characteristics displaying negative differential resistance for molecular wires with (111)-oriented metal contacts 112
5.12 Currents displaying rectification for a Pd/AT4/Au molecular wire 114

6.1 Extended molecule for an Au/OT/Fe molecular wire 120
6.2 Transmission probabilities for the Au/OT/Fe molecular wire 122
6.3 Currents exhibiting spin rectification for the Au/OT/Fe molecular wire . . . 124
6.4 Spin current rectification for a Pd/OT/Fe molecular wire 126
6.5 Currents for an Au/OT/Ni molecular wire 127

Chapter 1

Introduction

A molecular wire is an organic molecule that forms a conducting bridge between electronic contacts. A single organic molecule is likely to be the smallest entity to conduct electricity and thus molecular wires present many interesting challenges to fundamental science as well as enormous potential for technological applications.

Over thirty years ago, Aviram and Ratner [1] proposed theoretically that molecular wires should have the ability to rectify electronic current. Molecular electronics was born. However the concept lay dormant as technology with the ability to measure and manipulate materials on the single molecule scale was lacking. In the 1990's the development of scanning probe microscopy (SPM) and improvements in modern lithographic, self assembly and molecular synthesis techniques spawned experimental realizations of molecular wires [2, 3, 4, 5, 6, 7, 8, 9, 10, 11, 12, 13] and interest in molecular electronics was renewed. From the viewpoint of fundamental science, molecular wires are inherently quantum mechanical systems and thus present novel test beds for studying interesting quantum phenomena. Furthermore, the realization of molecular devices pushes modern experimental techniques to extreme limits and will undoubtedly continue to yield progress for experimentation. Even more exciting is that implementation of electronics based on single molecules may achieve devices with dimensions orders of magnitude smaller than conventional solid state devices. Continued advancement of electronic technologies requires platforms that may augment or even replace conventional solid state electronics for which fundamental size limits are believed to exist. Thus great incentives currently exist to study molecular electronics.

The experiments of the 1990's attempted to measure the conductance of single molecules arranged in self-assembled monolayers (SAMs) using scanning tunneling microscope (STM) [2, 3, 5, 6, 8] or mechanically controlled break junction techniques [4]. Atomic force microscopy (AFM) [9, 10, 11], cross-bar assemblies [12] and evaporated top metal contacts [7, 13] have also been used to measure conduction through SAMs. Such self-assembly schemes provide little control over the atomic details of the molecular junction and experiments that aim to measure the conductance properties of single or few molecules have been plagued with a number of uncertainties. These include whether a molecule is actually present in the junction, whether the molecule bonds properly to both contacts, the number of molecules that are present at the bridge site and whether impurities or metal filaments are present within the molecular barrier. Equally important, the specific atomic details of the electrode-molecule interface such as the molecular binding site, have been shown to strongly influence the transport properties of molecular wires hindering the reproducibility of experiments. Thus the community has recognized that the characteristics of a molecular device are properties of not only the molecule but also of the electrodes [14, 15, 16, 17]. In response to these obstacles, diligent experimental techniques have emerged allowing for the determination (in particular experimental setups) that a single molecule (or at the very most a few molecules) comprises the conducting bridge and that the molecule is properly bonded to both electrodes [18, 19, 20] . In addition, secondary imaging techniques such as inelastic electron tunneling spectroscopy (IETS), that have the potential to reveal additional information about atomic structure, have been applied to molecular wires [21]. Such industrious experimentation has finally permitted the realization of molecular rectifiers based on the original Aviram-Ratner scheme [22, 23].

Theories of molecular conduction have also made advances. Such studies traditionally begin by considering separately the electronic components that make up a molecular wire: Electrons in an isolated molecule, confined in all three spatial dimensions, are bound to the molecule in discrete molecular orbitals which are filled up to the Highest Occupied Molecular Orbital (HOMO). In an isolated macroscopic metal electrode (an electron reservoir) electronic states are continuous and develop energy bands which are filled up to the electrode Fermi energy. When the molecule is coupled to macroscopic electrodes to form a molecular wire, its discrete molecular orbitals hybridize with the continuous electronic states of the reservoirs becoming part of the continuum. Thus the discrete energy levels of the molecule broaden into transmitting states that become part of the continuous energy spectrum of the molecular wire and electrons may scatter from one electrode to the other via the molecule. A bias voltage applied between the two electrodes induces a net electron flux resulting in current flowing through the molecule. A standard method for evaluating such a current is Landauer theory [24] which relates the electronic current flowing through the system to the quantum mechanical probability for a single electron to scatter elastically from one electrode to the other. Quantitative analysis within the Landauer formalism requires knowledge of the underlying electronic structure of the molecular wire system.

Most theoretical work in molecular electronics has been based on semi-empirical tight-binding models and/or *ab initio* Kohn-Sham density functional theory (DFT) of the electronic structure. DFT attempts to calculate molecular electronic properties from first principles without adjustable parameters or input from physical intuition but is limited in practice to systems with relatively small numbers of atoms, does not have a rigorous justification when applied to transport calculations, and relies heavily on uncontrolled approximations. Semi-empirical methods can handle much larger systems and can use input from both experiment and *ab initio* methods, but their use is not straight forward and requires developing an intuitive understanding of the physics and chemistry of the systems being studied.

A number of calculations based on each method have attempted to explain the measured conductance of 1,4 benzene-dithiolate (BDT) molecules between gold electrodes[1] [4]. However in each case the calculation has overestimated the conductance by orders of magnitude [25, 26, 27, 28, 29]. Thus arguably the most successful application of modern molecular electronics theory to date is that reported by Emberly and Kirczenow [30] to explain the measured conductance of BDT wires. They argued that because the experiment [4] was performed using electrodes coated with SAMs of molecules that were brought into contact using a mechanically controlled break junction, the most likely configuration was not a *single* molecule properly bonded to both contacts. Instead they rationalized it was more likely that two overlapping molecules bridged the electrodes, where each molecule bonded to only one contact. Employing a theoretical description of the electronic structure of the molecular wire system based not on DFT but on simpler semi-empirical techniques, Emberly and Kirczenow successfully calculated a conductance of the correct magnitude.

---

[1] BDT (a benzene ring with hydrogen atoms at ring positions 1 and 4 substituted for sulfurs) consists of few atoms and possesses de-localized electron states that are presumed conductive, thus is a popular molecule for modeling.

The success of this and related work on other molecular electronic systems [5, 12, 31] speaks to the effectiveness of such semi-empirical techniques in helping to understand and predict molecular electronic phenomena. An expanded methodology based on similar semi-empirical techniques is employed throughout this thesis.

Molecular electronics continues to be an exciting area of condensed matter research. The classic paradigm of molecular electronics is based on single or few thiolated molecules bridging *gold* electrodes; the identification of molecular devices has focussed almost entirely on characteristics of the molecules themselves. Molecular wires with different conduction properties have been proposed and constructed through the incorporation of spatially asymmetric molecules [32], molecules that may undergo a conformational change in response to an applied bias voltage [33, 34], and molecules that may oxidize or reduce as a result of bias voltage [7]. Indeed the current rectification predicted in the original Aviram-Ratner scheme [1], and its subsequent realizations [22, 23], were due to intrinsic properties of the donor/acceptor molecules considered for the bridge. However in light of the recognition that the characteristics of molecular devices are sensitive to the properties of not only the molecules but also the electrodes, interest in molecular electronic devices with more complex metal electrodes is growing.

Integration of complex metal electrodes with relatively simple organic molecules has already brought together molecular electronics and the established field of spintronics [35, 36, 37] yielding a new branch of nanoscience termed *molecular spintronics* [38, 39, 40, 41, 42, 43, 44]. It was predicted that the electronic transport across molecules bridging two ferromagnetic nickel electrodes would depend sensitively on electron spin resulting in appreciable magnetoresistance [38]. Indeed preliminary experimental reports have confirmed that a molecular bridge is capable of sustaining significant spin polarization leading to magnetoresistance [45, 46, 47] and novel molecular spintronic systems are just beginning to be explored while being amongst the smallest possible nanoscale spintronic devices.

The aim of this thesis is to develop a general understanding of the interesting electron transport properties of molecular wires with *transition metal* electrodes. It is demonstrated that the mechanisms responsible for transport at moderate bias in such wires are not due to 'pure' molecular states (such as the HOMO), as is expected for molecular wires with gold electrodes. Instead the current is dominated by transport mediated by electronic states at the metal-molecule interfaces that develop as a result of the strong chemical bonding between molecular sulfur orbitals and transition metal d-electron orbitals. Thus strong features in the transition metal electrode densities of states lead to enhancements in the transmission at corresponding energies. In short molecular wires, these *interface states* contribute appreciably to the conductance. Being located mainly within the transition metal contacts and having strong transition metal d-orbital character, the energies of the states track with the bias voltage applied between the contacts of the molecular wire. Thus a bias voltage may resonantly enhance or reduce the current; finite bias effects must be included explicitly for reliable predictions in contrast to molecular wires with gold electrodes where such effects are commonly neglected[2]. This understanding is systematically developed through the exploration of a number of new, physically important nanoelectronic systems.

Nanoelectronic devices with ferromagnetic *iron* electrodes are a core focus of this thesis. Spin-dependent transport through iron nanocontacts bridged with a pair of iron atoms is a natural starting point for studying molecular wires with magnetic transition metals since the two iron atoms may be regarded as a small molecule while at the same time being of the same atomic species as the contacts. This system is considered first [48] to elucidate the systematics and complexities of spin-dependent transport in nanoscale systems and to provide a basis for which to compare and understand the factors that affect electron transport in nanoscale systems with other transition metal electrodes. *Organic* molecular wires with iron electrodes [43], systems that have not previously been considered either theoretically or experimentally, are investigated next and novel spin-dependent transport mechanisms and device characteristics are predicted. Single molecules bridging ferromagnetic nickel electrodes are also investigated and a possible explanation of some experimentally observed phenomena [47] is proposed. Based on the general understanding of transport in molecular wires with transition metal electrodes developed through investigation of these systems, a new controllable negative differential resistance (NDR) mechanism owing to resonant transport mediated by interface states [49, 50] with potential applications for molecular electronic technology and a novel physical phenomenon termed *spin current rectification* [51] are also introduced in this thesis.

Molecular electronics theory is a difficult and emerging subject and reliable application of the theory to realistic systems remains challenging. Molecular wires are extremely complex, many-body systems with huge numbers of quantities required for models that aim to

---

[2] See for example Refs. [25, 26, 27, 30].

establish a connection with potential experiments, many of which can not be determined accurately with modern experimental or theoretical techniques. In addition to several that have been mentioned, some of the unknowns required for accurate modeling include: the change, if any, of the geometrical structure of the molecule upon binding to electrodes, the preferred binding site and bond lengths of the molecule to the electrodes, the crystallographic orientation of the electrode surface, the molecular-contact energy alignment, the charge transfered to the molecule upon binding to the contacts, the effect of applied bias voltage on the geometry of the molecular junction and how the applied bias affects the electronic states and charge of the wire. However, as transport experiments have yet to be performed on the majority of the transition metal-molecular wire systems considered in this thesis, the predictions presented here are intended to stimulate related experiments that may be achieved with a number of different of techniques. Thus, while atomic details of the metal-molecule interface are required at the outset of the transport calculation that is based on an atomic description of molecular wires, physically reasonable *estimates* for these parameters based on insights from experiment, calculation and physical intuition is sufficient for the present purpose. In this fashion, qualitative trends may be extracted from the resulting electron transport predictions. Trends that are robust to variations in the model parameters should be directly observable in a range of experimental systems for which control of the atomic scale geometries is beyond the present state-of-the-art. Thus the qualitative phenomena presented in this thesis should be accessible to present day experimental techniques.

This thesis is organized into seven chapters. Microscopic model calculations for predicting current-voltage characteristics of molecular wires with transition metal electrodes are developed in Chapter 2. The chapter begins with an introduction to Landauer theory relating current to the quantum mechanical probability for a single electron to be transmitted across a molecular wire. Simplification of the many-body Schrödinger equation through a number of physical approximations follows, along with a review of density functional theory (DFT), insights from which are used to appropriately modify the electronic structure methods used to model molecular wires. These electronic structure methods are based on a semi-empirical tight-binding formalism for modeling transition metals together with extended-Hückel theory used to model molecules and an introduction to each is presented next. With the molecular wire Hamiltonian defined, a method for calculating the transmission probability based on an elastic scattering formalism suitable for transition metal electrodes [48] is then developed. The effects of finite bias voltage and the electrostatic potential profile are introduced in the following section. The chapter is concluded with a presentation of Mulliken analysis which is used to gain understanding of the mechanisms responsible for transport in each of the mesoscopic systems that follow. The methodology is applied to study a number of physically important systems in the remaining chapters.

A systematic study of spin-dependent transport through ferromagnetic iron nanocontacts bridged by iron atoms [48] is presented in Chapter 3. First, the classical Julliére model for approximating magnetoresistance based on experimentally measured spin polarizations of individual contacts is introduced and its deficiencies are discussed. Next it is demonstrated that the semi-empirical parameters applied to model the iron contacts provide a satisfactory description of the surface properties of iron nano-clusters as well as bulk properties. The full quantum mechanical calculation introduced in Chapter 2 is performed next to calculate the current-voltage characteristics and magnetoresistance for iron nanocontacts bridged in a range of junction geometries. Several novel phenomena are predicted including negative magnetoresistance and spin-transport resonances due to dangling bond formation as the chain is stretched through its breaking point. An examination of the spin-dependent tunneling between ferromagnetic nanoscale iron contacts separated by vacuum concludes the chapter.

In Chapter 4, the spin-dependent transport calculation is extended to study single-molecule spintronic devices beginning with its application to single BDT or alkane-dithiolate molecules bridging ferromagnetic iron electrodes [43]. It is predicted that the magnetoresistance should become inverted with increasing bias and its relevance to experiment and to potential technological applications is discussed. The physical origin of the inverted magnetoresistance is attributed to interface states that develop due to the strong chemical bonding between the thiol-terminated ends of the molecules and the d-electron orbitals of the iron electrodes. Next spin-dependent transport is studied for single alkane-thiolate molecules bridging ferromagnetic nickel electrodes and a possible explanation of some experimentally observed phenomena [47] is proposed. The organic-nickel system lends itself to an analytic procedure developed in Appendix D for extracting *effective* bias-dependent spin polarizations of each electrode that reproduce the calculated magnetoresistance when used together with the Julliére formula. The calculated effective spin polarizations have little connection with the commonly accepted measured spin polarization values for isolated contacts demonstrating the important role played by the metal-molecule interface in molecular spintronic systems.

The nature of metal-molecule interface states is explored in greater detail in Chapter 5 for molecular junctions where single thiolated organic molecules bridge non-magnetic transition metal electrodes [49, 50]. It is demonstrated that electron transmission at moderate bias is mediated by interface states for thiolated molecular wires when the transition metal contacts have strong d-orbital components near the Fermi level. The dependences of the interface state resonances on the orientation of the metal interface, the adsorption site of the molecule, and the separation between the thiolated ends of the molecule and the metal contacts are examined. Resonant enhancements and reductions of the interface state transmission as the applied bias is varied are predicted, resulting in non-linear transport phenomena including negative differential resistance (NDR) and rectification in molecular junctions with palladium and platinum nanocontacts. NDR realized in this new way should be technologically interesting and may be controlled by tailoring interface state properties through appropriate choice of nanoelectrode transition metals and surface structures.

Finally in Chapter 6 the principles developed in the preceding chapters are applied to identify, not only a new molecular device, but a new physical phenomenon which has not previously been explored either experimentally or theoretically: *spin current rectification* by molecules [51]. Consistent with thermodynamic considerations, two forms of spin current rectification in molecular wires are predicted: A *weak* form in which the spin current reverses direction when the bias voltage applied to the junction is reversed and a *strong* form in which the direction of the spin current is unchanged upon reversal of the bias. Calculations of spin-dependent transport are presented for several molecular junctions bridging ferromagnetic (iron or nickel) and non-magnetic (gold or palladium) contacts and specific systems that should exhibit spin current rectification of each type depending on the materials used and the experimental conditions are identified. Molecular wires displaying both spin current and charge current rectification are expected to be possible, and may find practical application in nanoscale devices that combine logic and memory functions.

Chapter 7 concludes the thesis by summarizing the new, important results developed here and some of the challenges that remain for future studies.

Chapter 2

Electron Transport in Molecular Wires with Transition Metal Contacts

2.1 Introduction

A methodology for calculating the electronic current flowing through a two-terminal molecular wire in response to a bias voltage applied between the electrodes is developed in this chapter. The Landauer formalism which relates the electronic current to the probability of an electron incident upon a molecular junction to be transmitted through the molecule into the drain reservoir is introduced in Section 2.2. Through a number of physical approximations, the many-body Schrödinger equation for an infinite number of interacting electrons is simplified in Section 2.3. Once a tractable quantum mechanical problem has been formulated and a Hamiltonian describing molecular wires with transition metal electrodes has been introduced based on general considerations, Sections 2.4 and 2.5 introduce electronic structure methods from quantum chemistry that will be utilized extensively throughout this thesis. The methods are combined in the next sections with an electronic structure method suitable for transition metal electrodes and explicit Hamiltonian matrices describing molecular wires will be generated. With the scattering Hamiltonian explicitly defined, Section 2.8 introduces a method for numerically calculating the scattering wavefunction and thus the transmission probability for molecular wires with transition metal electrodes. The explicit inclusion of finite bias effects into the scattering theory is discussed in Section 2.9.

The chapter is concluded with an introduction to Mulliken Analysis which is employed throughout this thesis to elucidate the nature of molecular orbitals that are responsible for conduction through the molecular wires.

2.2 Landauer Theory for Calculating Electronic Current in Mesoscopic Systems

Two-terminal mesoscopic electronic systems (e.g., molecular wires) are characterized most simply as two metallic electrodes that act as source and drain reservoirs for electrons, connected via a junction of atoms or molecules. Coupled to macroscopic electrodes, the discrete molecular energy levels of the molecule broaden into transmitting states that become part of the continuous energy spectrum of the molecular wire and electrons may scatter from one electrode to the other via the molecule. As a bias voltage is applied across the electrodes, a current may flow through the junction. A standard method for evaluating such a current is Landauer theory [24]. (For a review of Landauer-Büttiker theory see Ref. [52].) This relates the electronic current flowing through the system to the quantum mechanical probability for a single electron to scatter elastically from one electrode to the other. For a two-terminal system, the current as a function of the applied bias voltage V may be calculated as

$$I(V) = \frac{e}{h} \int_{-\infty}^{\infty} dE \, T(E,V)[f(E,\mu_S) - f(E,\mu_D)] \tag{2.1}$$

where $f(E,\mu) = 1/(e^{[(E-\mu)/kT]} + 1)$ is the equilibrium Fermi distribution and $\mu_S = E_F + eV/2$ and $\mu_D = E_F - eV/2$ are the electrochemical potentials of the source (S) and drain (D) electrodes respectively in terms of the common Fermi energy, E_F; only zero temperature scattering is considered in this thesis[1] thus $f(E,\mu) = 1$ or 0, if $E < \mu$ or $E > \mu$, respectively. $T(E,V)$ is the quantum mechanical probability of an electron incident upon the molecular junction with energy E to be transmitted through the molecule into the drain reservoir. $T(E,V)$ is, in general, dependent on the applied bias voltage V as the electronic structure describing the molecular wire redistributes as the applied bias is varied. Thus the electron

---

[1] The typical energy scale for transport in the systems introduced in the following chapters is approximately $1eV$, hence raising the temperature of the systems to room temperture ($kT \sim 0.03eV$) is expected to have a relatively minor impact on the resulting qualitative predictions.

flux is determined by the net probability of an electron in an occupied state in the source to scatter through the molecule into an unoccupied state in the drain reservoir.

The remainder of this chapter develops a methodology for calculating $T(E,V)$ for elastic scattering in molecular wires with transition metal electrodes.

2.3 Quantum Chemistry and the Many-Body Schrödinger Equation

A molecular wire characterized by a molecule bridging macroscopic metal electrodes is a *many-body* quantum mechanical system with infinite degrees of freedom whose steady-state[2], many-body wavefunction is governed by the time-independent Schrödinger equation $H|\Psi\rangle = E|\Psi\rangle$ for a large number N of interacting particles. If atomic nuclei are treated as fixed with respect to the mobile electrons in the wire (the Born-Oppenheimer Approximation) the electronic Schrödinger equation may be written as

$$\sum_{i=1}^{N}(-\frac{\hbar^2}{2m}\nabla_i^2|\Psi(\mathbf{r})\rangle - \frac{1}{4\pi\varepsilon_0}\sum_I Z_I\frac{e^2}{|\mathbf{r}_i-\mathbf{R}_\mathbf{I}|}|\Psi(\mathbf{r})\rangle) + \frac{1}{2}\frac{1}{4\pi\varepsilon_0}\sum_i\sum_{j\neq i}\frac{e^2}{|\mathbf{r}_i-\mathbf{r}_j|}|\Psi(\mathbf{r})\rangle = E|\Psi(\mathbf{r})\rangle \tag{2.2}$$

where $|\Psi(\mathbf{r})\rangle$ is the N electron wavefunction, $\mathbf{r} = \{\mathbf{r_i}\}$ are the electronic positions, m is the electron mass, and Z_I are the ionic charges at positions $\mathbf{R_I}$ [53]. The first term in Equation (2.2) is the kinetic energy term, the second term represents the electrostatic potentials due to the Coulomb interactions of the electrons with the bare atomic nuclei and the last term is due to electron-electron interactions.

Equation (2.2) is impossible to solve exactly for all but the simplest systems and several approximations are required for practical calculation. In the Hartree Approximation (the simplest mean-field theory) the many-electron wavefunction is approximated by the product of single-electron states $|\Psi_i\rangle$:

$$|\Psi(\mathbf{r})\rangle = |\Psi_1(\mathbf{r}_1)\rangle|\Psi_2(\mathbf{r}_2)\rangle...|\Psi_N(\mathbf{r}_N)\rangle. \tag{2.3}$$

In reality Eqn. (2.3) must be replaced by a linear combination of anti-symmetrized products or Slater determinants because the Pauli exclusion principle requires the many-electron

---

[2] Time-dependent transport and inelastic processes are not considered in this thesis.

wavefunction $|\Psi\rangle$ to be antisymmetric (which Eqn. (2.3) is not). However, while calculation of total energies or ground state wavefunctions (as in Section 2.4) of a quantum system require knowledge of the full many-body wavefunction $|\Psi\rangle$, transport calculations within the Landauer formalism require only the single-electron wavefunctions $|\Psi_i\rangle$.

Within the Hartree Approximation (and the more sophisticated Kohn-Sham density functional theory described below), Equation (2.2) for N electrons is replaced with a set of N one-electron equations

$$(-\frac{\hbar^2}{2m}\nabla^2 + V_{eff}(\mathbf{r}))|\Psi_i(\mathbf{r_i})\rangle = E_i|\Psi_i(\mathbf{r_i})\rangle \tag{2.4}$$

where $V_{eff}(\mathbf{r})$ is an effective potential produced by all ions and electrons felt by electron i. The electron-electron interaction portion of $V_{eff}(\mathbf{r})$ is complex and, in general, is also a function of $|\Psi_i(\mathbf{r_i})\rangle$, thus the solution of Equation (2.4) is difficult without further approximation. In the field of molecular electronics the level of approximation employed for $V_{eff}(\mathbf{r})$ is often categorized into *model chemistries.* Two model chemistries will be introduced in detail in Sections 2.4 and 2.5.

The Tight-binding Approximation (TBA) is used throughout this thesis and expresses the scattering wavefunctions $|\Psi(\mathbf{r})\rangle$ that span all space in terms of a discrete set of electronic orbitals. I.e., $|\Psi\rangle$ is represented using a linear combination of atomic orbitals (LCAO): $|\Psi\rangle = \sum_j \Psi_j|j\rangle$, where $|j\rangle$ spans all atomic orbitals of all atoms in the system (which at this point spans infinite dimensions). Thus within TBA, molecular wires are described atomistically and electrons move through the system by hopping between atomic orbitals. The atomic orbitals $|j\rangle$ are general functions often chosen to be Slater-type orbitals (STOs) or gaussian-type orbitals, typically representing all valence electron orbitals in the system. Core electronic orbitals are often neglected as electrons in those orbitals are tightly bound to the atomic nuclei and thus are less mobile than valence electrons; their energies are lower and thus contribute mainly to states that are fully occupied and do not contribute to the current except at extremely high bias. Substituting the LCAO approximation for the scattering states $|\Psi\rangle$ and bracketing with atomic orbital $\langle i|$, the N single-electron differential Schrödinger equations are replaced by the matrix equation

$$\sum_j H_{i,j}\Psi_j = E\sum_j S_{i,j}\Psi_j \tag{2.5}$$

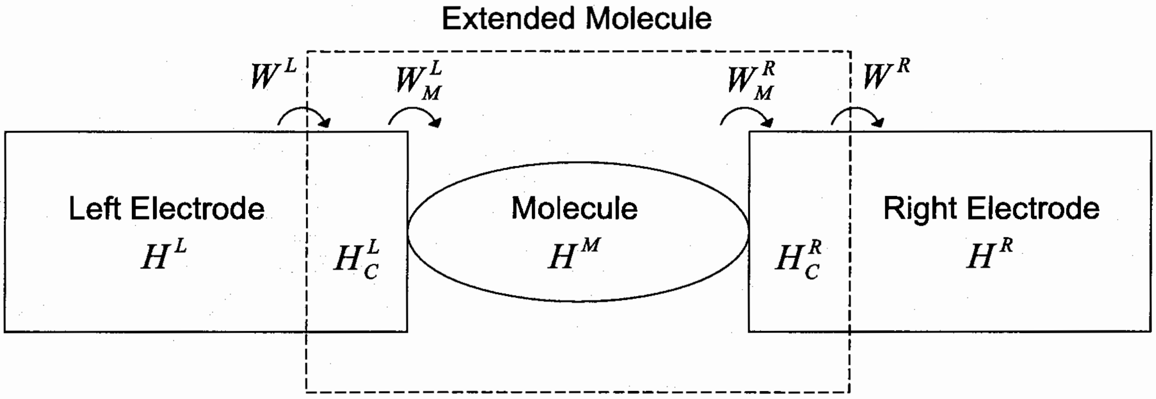

Figure 2.1: Schematic partitioning of a molecular wire into left and right semi-infinite electrodes and an 'extended molecule' consisting of the molecule and finite metal clusters from each electrode.

where $H_{i,j} = \langle i|H|j\rangle$ are the Hamiltonian matrix elements in the basis of atomic orbitals. The atomic orbitals $\{|j\rangle\}$ may be non-orthogonal thus the overlap matrix $S_{i,j} = \langle i|j\rangle$ appears in Eq. (2.5). Each eigenvector of Equation (2.5) corresponds to one of the N single-particle solutions to Equations (2.4). In TBA the Hamiltonian and overlap matrices need be evaluated only on *discrete* atomic orbitals and may be calculated either directly with *ab initio* techniques that employ a level of approximation for $V_{eff}(\mathbf{r})$ in Equation (2.4) or estimated with semi-empirical techniques. The transmission probability $T(E,V)$ required in Equation (2.1) is calculated by explicitly solving the tight-binding Schrödinger Equation (2.5) at every energy E for the single-electron scattering states, $|\Psi\rangle$.

It is universally recognized that the properties of molecular wires are strongly dependent on not only the details of the molecular bridge but also of the electrodes [14, 15, 16, 17]. Thus an accurate description of the metal-molecule interface is crucial for reliable predictions of electronic transport in molecular electronic devices. As a result, it is common practice to include a portion of each of the left and right electrodes (as illustrated in Figure 2.1) when calculating the electronic structure of the molecule so that the chemical nature of the interface between the molecule and electrode surfaces is treated on an atomistic level. Therefore, the semi-infinite electrode reservoirs of the molecular wire are connected via an *extended molecule* with Hamiltonian

$$H^{EM} = H^M + H^L_C + H^R_C + W^L_M + W^R_M \tag{2.6}$$

where H^M is the Hamiltonian describing the molecule, $H_C^{L,R}$ are the Hamiltonians for the finite left and right electrode clusters that are included in the extended molecule, and $W_M^{L,R}$ are the Hamiltonians that couple the electrode clusters and the molecule. The elastic scattering Hamiltonian for the entire molecular wire may thus be rewritten as

$$H = H^{EM} + H^L + H^R + W^L + W^R \tag{2.7}$$

where $H^{L,R}$ are the Hamiltonians for the semi-infinite left and right electrodes that act as reservoirs for electrons and $W^{L,R}$ are the coupling Hamiltonians between the semi-infinite source and drain electrodes and each of the finite clusters included in the extended molecule. The terms implicitly include the effects of the bias voltage (if any) that is applied between the electrodes (see Section 2.9).

The electrodes that are infinite electron reservoirs for the molecular wire extend to $\pm\infty$ and are assumed periodic along the length of the wire. Thus the set of atomic orbitals $\{|j\rangle\}$ in Equation (2.5) is more appropriately replaced with the set $\{|n,j\rangle\}$ where n labels the cell in the direction of electron propagation and j spans the atomic orbitals within a cell. In what follows, the extended molecule will be assumed to occupy cell $n = 0$, while the left electrode occupies cells $n = -\infty..-1$ and the right electrode occupies cells $n = 1..\infty$. Thus the Hamiltonian Eqn. (2.7) is expressed in the basis of cells and atomic orbitals: $H_{n,i,m,j} = \langle n,i|H|m,j\rangle$.

With the scattering problem formulated, the following sections introduce chemistries for explicit evaluation of model Hamiltonians that describe molecular wires: The first of these, density functional theory, is drawn upon for structural and electronic considerations that are incorporated to refine the extended-Hückel-based tight-binding formalism used throughout this thesis. An introduction to extended-Hückel theory that is used for explicit calculation of the electronic parameters that enter in the molecular Hamiltonian, H^M, and $W_M^{L,R}$ in Equation (2.7) follows next. A methodology for appropriately modifying the extended-Hückel method to accurately represent the electronic structure of transition metal contacts and to include additional physical insight will be developed in the section that follows. This hybrid approach combining density functional considerations with the augmented extended-Hückel formalism permits calculations to be performed for larger structures than can be treated using density functional theory alone. It also allows the incorporation of semi-empirical features into the calculations which can compensate for some known deficiencies of density functional theory as applied to molecular electronic transport calculations.

2.4 Density Functional Theory

Density functional theory (DFT) is an *ab initio* formalism that has gained significant popularity for molecular electronics research. At the heart of DFT lies the Hohenberg-Kohn theorem [54] that establishes the *existence* of a unique functional[3] that determines the many-body ground state energy and electron density of a quantum mechanical system. The theorem does not provide, however, the form of said functional and new model functionals and refinements to existing functionals continue to emerge in the literature. The many-body ground state energy E may thus be written as a functional of the ground state electron density: $E[\rho(\mathbf{r})]$. Minimizing $E[\rho(\mathbf{r})]$ with respect to $\rho(\mathbf{r})$ while keeping $N = \int \rho(\mathbf{r}) dr^3$ fixed (N is the number of electrons in the system) yields an estimate for the ground state energy.

Replacing the N interacting electron wavefunction $|\Psi(\mathbf{r})\rangle$ in Equation (2.2) with electron density, the total energy may be written rigorously as

$$E[\rho(\mathbf{r})] = T[\rho(\mathbf{r})] - e\int V(\mathbf{r})\rho(\mathbf{r})dr^3 + \frac{1}{2}\frac{e^2}{4\pi\varepsilon_0}\int \frac{\rho(\mathbf{r})\rho(\mathbf{r}')dr^3 dr'^3}{|\mathbf{r}-\mathbf{r}'|} + E_{XC}[\rho(\mathbf{r})] \quad (2.8)$$

where $T[\rho(\mathbf{r})] = -\frac{\hbar^2}{2m}\int \nabla^2\rho(\mathbf{r})dr^3$, $V(\mathbf{r}) = \frac{1}{4\pi\varepsilon_0}\sum_I Z_I e \frac{1}{|\mathbf{r}-\mathbf{R_I}|}$ and $E_{XC}[\rho(\mathbf{r})]$ is the exchange-correlation potential that includes all effects due to the Pauli exclusion principle and electron-electron interactions not included by the third term in the above energy expression.

The local density approximation (LDA) assumes that E_{XC} is a *local* functional depending only on $\rho(\mathbf{r})$ (i.e., the system is treated locally as a uniform electron gas and E_{XC} depends only on position as opposed to gradient corrected methods in which the exchange-correlation also depends on $\vec{\nabla}\rho(\mathbf{r})$). Thus the exchange-correlation may be expressed approximately as an integral involving only the electron density. A particular DFT method, or model chemistry, is defined by choosing a specific approximation for E_{XC}.

Kohn and Sham established [55] that LDA renders solving Equation (2.8) *mathematically* equivalent to solving N equations for single, non-interacting (quasi) particles, as in Equation (2.4). In the Kohn-Sham formulation, $V_{eff}(\mathbf{r})$ includes the exchange-correlation as well as the electrostatic potential due to the nuclei and electron-electron interaction terms

---

[3] A functional is a function of a function.

in Equation (2.8) that depend on $\rho(\mathbf{r})$ and thus is also a function of $\rho(\mathbf{r})$. Upon solving each of the N electron equations for the single-particle wavefunctions, $|\Psi_i(\mathbf{r})\rangle$ (the Kohn-Sham orbitals), the ground state electron density is obtained as

$$\rho(\mathbf{r}) = \sum_{i=1}^{N} |\Psi_i(\mathbf{r})|^2. \tag{2.9}$$

Thus the ground state energy and electron density may be obtained self-consistently by iteratively solving for $|\Psi_i(\mathbf{r})\rangle$ where a new $V_{eff}(\mathbf{r})$ is numerically integrated at each step from the explicit E_{XC} that is chosen and the resulting $\rho(\mathbf{r})$ in Equation (2.9). In practice, the Kohn-Sham orbitals are usually treated using LCAO or plane wave bases.

Unlike the physical single-particle wavefunctions of Equation (2.4), Kohn-Sham orbitals are mathematical entities constructed to perform total energy and density calculations and have no rigorous connection to physical reality. However, although physical justification is lacking, Hamiltonians (such as those in Equations (2.6) and (2.7)) may be constructed in the basis of Kohn-Sham orbitals and have become the foundation on which an assortment of quantum transport algorithms have been established [29, 56, 57, 58]. This is problematic since the results of molecular electronic transport calculations that are based on the Landauer formalism (Eqn. (2.1)) are sensitive to the single-particle eigenfunctions and eigenvalues of those Hamiltonians. However molecular electronics theory is still an evolving field and methods that are *both* rigorous and practical have yet to emerge.

In addition to the above considerations, general density functional algorithms have not been optimized to study hybrid organic-metallic structures with large magnetic moments such as the molecular wires with large numbers of ferromagnetic atoms studied throughout this thesis in the context of spin-dependent transport[4]. Thus DFT approaches can not reliably replace the semi-empirical techniques used throughout this work.

On the other hand, appropriate semi-empirical values are not available for all parameters and *ab initio* methods are also important in developing the tight-binding models employed throughout this thesis. DFT is often less computationally demanding than comparable true *ab initio* techniques and can provide reliable information that includes total ground state and ionization energies. Also geometry relaxations of quantum systems including molecules may be performed accurately within DFT by calculating ground state energies

---

[4] The author is aware of two exceptions currently under development [42, 44]

as atomic nuclei spatial degrees of freedom ($\{\mathbf{R_I}\}$) are varied on a potential energy surface. A global minimum on the potential energy surface corresponds to the most likely molecular geometry while local minima are predicted metastable equilibrium positions. Unlike the application of DFT to transport, such DFT-based geometry calculations have a fundamental justification since the Hohenberg-Kohn theorem applies to total energies of many-body systems.

2.5 Extended-Hückel Theory

Extended-Hückel theory is a semi-empirical, valence electron (electrons in core orbitals are assumed frozen and thus not treated explicitly) LCAO formalism that provides an approximate description of the electronic structures for a wide variety of molecules. It uses a non-orthogonal basis of atomic orbitals $\{|\phi_i\rangle\}$ and relates Hamiltonian matrix elements to experimental ionization energies for isolated atoms [59]. The functional form of the atomic orbitals are Slater-type orbitals (STO's) which are approximations to single-particle wavefunctions in many-electron atoms and given by

$$\phi_i(\mathbf{r}) = \langle \mathbf{r}|\phi_i\rangle = N_i R_n(\zeta, r) Y_{l,m}(\theta, \phi) \tag{2.10}$$

where N_i is a normalization constant and $Y_{l,m}$ is the spherical harmonic for the ith orbital with quantum numbers l and m. The radial component with principle quantum number n is given by

$$R_n(\zeta, r) = (2\zeta)^{n+\frac{1}{2}} \frac{1}{\sqrt{2n!}} r^{n-1} e^{-\zeta r} \tag{2.11}$$

where ζ is a phenomenological orbital decay parameter known as the Slater exponent. Linear combinations of STO's are used to account for nodal behavior of higher-order spherical harmonic solutions (such as in d-orbitals) to the one-electron Schrödinger equation.

The diagonal Hamiltonian matrix elements, $H_{i,i} = \langle\phi_i|H|\phi_i\rangle$ are identified with experimental ionization energies for the corresponding atomic orbital ϕ_i of isolated atoms; the hydrogen $1s$ orbital matrix element for example is given by $H_{1s,1s} = -13.6eV$. In the Wolfsberg-Helmholtz form [60] of the model the off-diagonal matrix elements are obtained from the following relation

$$H_{i,j} = \frac{K}{2}(H_{i,i} + H_{j,j}) S_{i,j} \tag{2.12}$$

where K is a phenomenological parameter, usually taken to be 1.75 in order to match experimental data. $S_{i,j}$ are the overlap matrix elements connecting orbitals ϕ_i and ϕ_j, and are usually calculated by numerical integration

$$S_{i,j} = \langle \phi_i | \phi_j \rangle = \int \phi_i(\mathbf{r}) \phi_j(\mathbf{r}) d\mathbf{r}^3. \tag{2.13}$$

Numerical values for atomic ionization energies as well as Slater exponents are taken from Ref. [61, 62].

Extended-Hückel theory may be used to construct Hamiltonians that enter Equation (2.5) and this approach has been used successfully to explain the experimental current-voltage characteristics of molecular wires connecting gold electrodes [5, 12, 30]. However it does not provide an accurate description of the electronic and magnetic structures of *transition metal* crystals. Thus additional semi-empirical tight-binding techniques are required to augment extended-Hückel theory for describing for molecular wires with transition metal electrodes.

2.6 Tight-binding Formalism for Molecular Wires with Transition Metal Contacts

The finite metal clusters that are included in the extended molecule (Equation (2.6)) to represent the nanoscale contact region of molecular wires are defined atomistically where every atom of each cluster is assumed to occupy sites of a perfect crystal lattice. The electronic structure of the metal clusters may thus be modeled by a tight-binding Hamiltonian, $\langle 0,i | H_C^{L,R} | 0,j \rangle$, in a non-orthogonal basis (with overlap matrix $\langle 0,i | 0,j \rangle$ between atomic orbitals i and j) of valence s, p and d atomic orbitals, where the tight-binding parameters[5] are based on fits to *ab initio* band structures[6] of metal crystals [64]. A minimal set of Hamiltonian and overlap matrix elements that extend to second nearest-neighbor hopping (all others are assumed zero) are provided in Ref. [64] from which all other matrix elements may be generated from general symmetry considerations for atoms that occupy crystal lattice positions. Thus a functional basis set form is not required for this model.

---

[5] Slater-Koster 3-center parameters are selected.

[6] *Ab initio* band structure calculations compare well with experimental angle-resolved photoemission spectra; see for example Ref. [63] and references therein.

For ferromagnetic electrodes such as iron or nickel (introduced in Chapters 3 and 4), two sets of semi-empirical tight-binding parameters are provided in Ref. [64]: One set for spin *up*, one for spin *down*. Thus the transmission probabilities $T(E,V)$ and the current in Equation (2.1) are calculated independently as the parameter sets are applied separately for each spin channel; the total current is the sum of the contributions from each spin channel.

The transition metal clusters for the extended molecules in the following chapters are relatively large (each consisting of more than 50 atoms), albeit small with respect to *physical* systems that form when two macroscopic electrodes are contacted to create a nanoscale junction. Thus modeling the electronic structure of the clusters with parameters fitted to bulk crystals captures more fully the character of real macroscopic contacts. Moreover, as explained in Section 3.3, the model provides a satisfactory description of not only bulk properties, but also qualitatively accounts for the effects of surfaces and nanoscale geometries. Thus the tight-binding model, that is based on fits to bulk band structures, should appropriately describe also the nanoscale contact region of a physical mesoscopic junction that develops as macroscopic transition metal electrodes come together to form a molecular wire.

The tight-binding model described above that accurately represents the electronic structure of transition metal contacts is employed to augment the tight-binding formalism based on an extended-Hückel description of molecules that enter in the extended molecular Hamiltonian, H^{EM} (Eqn. (2.6)), for molecular wires in the following way: the Hamiltonian, $H_C^{L,R}$, and overlap matrices for the finite transition metal clusters are calculated with the tight-binding formalism based on the parameters in Reference [64]. Once the geometry of the extended molecule region has been appropriately estimated within DFT[7], extended-Hückel calculations are performed for the molecular Hamiltonian, H^M, and overlap matrix as well as the coupling Hamiltonians, $W_M^{L,R}$, between the molecule and finite metal clusters. Thus the coupling Hamiltonians, $W_M^{L,R}$, are spin-independent matrices (even for ferromagnetic contacts) which is consistent with the published off-diagonal matrix elements connecting spin *up* orbitals that are not very different from the corresponding matrix elements connecting spin *down* orbitals [64]. This is physically reasonable given that the spatial part of a spin *up* orbital should be similar to that of the corresponding spin *down* orbital.

---

[7] Typically this involves a geometry relaxation of the molecule [65] with respect to the fixed geometry of a subset of metal atoms from the extended molecule.

Extended-Hückel matrix elements are based on atomic ionization energies while the electronic parameters from Ref. [64] describing the metal clusters are defined up to an arbitrary additive constant. It is necessary to choose the value of this constant with care in order to obtain realistic electronic structure predictions from the hybrid tight-binding model. The constant is adjusted to align the Fermi energy of the electrodes relative to the Highest Occupied Molecular Orbital (HOMO) of the molecule according to the difference between the experimental work function, Φ_{exp}, of the particular transition metal [66] and the HOMO energy of the isolated molecule calculated within DFT[8], E^{DFT}_{HOMO} [65]. Thus, the relative separation between the HOMO and the Fermi level of the metal electrodes is estimated as $\Delta E = -\Phi_{exp} - E^{DFT}_{HOMO}$. The Hamiltonian matrix elements for the transition metal clusters, $H^{L,R}_C$, are adjusted so that the Fermi energy of the contacts is located according to the estimate ΔE with respect to the the HOMO energy calculated within the extended-Hückel method employed to model the electronic structure of molecular wires. A procedure for applying such a shift in energy for molecular wires modeled with non-orthogonal bases is outlined in Appendix A.

The Fermi level alignment outlined above neglects effects due to charge transfer. Nevertheless, a similar method has been used successfully to align the Fermi energy of gold with the HOMO of benzene-dithiolate (BDT) [67], thereby reproducing the shape of the measured current-voltage characteristic. The sensitivity of the current-voltage results presented in this thesis to charging effects is investigated in the following chapters by incorporating variations in ΔE to simulate qualitatively possible effects of changes in the potential distribution associated with charging. It is established that although charging effects may influence quantitative results, the qualitative predictions presented in this thesis are expected to be robust to such charge transfer effects.

2.7 Modeling Transition Metal Electrodes

The semi-infinite electrodes of a molecular wire are assumed periodic structures in the direction of electron propagation and thus electrons exist within them in one-dimensional Bloch states. Since the electrodes have finite cross-section (as opposed to a single one-

---

[8] DFT HOMO energy levels may be related to molecular ionization energies, thus are unique Kohn-Sham orbitals with connections to physical reality.

dimensional chain), the electrons have also transverse momentum (which is quantized) and an electron with energy E may exist in several different Bloch states. Each Bloch state corresponds to a different scattering channel at energy E, and an electron may be incident with scattering state $|\Psi^{\alpha}\rangle$ and longitudinal wave vector k^{α} upon the molecular junction from one channel, α, of several. The wavefunction thus satisfies the single-electron scattering Schrödinger equation $H|\Psi^{\alpha}\rangle = E|\Psi^{\alpha}\rangle$ where H is Hamiltonian (2.7) for the coupled molecular wire system.

Unlike gold which is an s-metal, where the Fermi energy resides in an energy band that has predominately s-electron character, the Fermi energies for the transition metals studied in this thesis lie in an energy region where the band structures have significant contributions from s, p, and d-electron orbital states. Whereas it has been found sufficient with gold to model the semi-infinite source and drain electrodes with a simple s-orbital description [25, 38, 68] (and thus one orbital per atomic site), doing so for molecular wires with transition metal contacts was found to be inadequate in the course of the present research. Thus, the full valence orbital basis set (9 orbitals – 1 s, 3 p, and 5 d) is necessary for modeling, not only the finite metal clusters included in the extended molecule, but also the semi-infinite transition metal electrodes.

On the other hand, as the extended molecule includes a finite but large cluster from each electrode, the macroscopic electronic character of the electrodes is well represented in the extended molecule (as discussed in the previous section and in detail in Chapter 3). Hence, the main requirement for the semi-infinite electrodes, $H^{L,R}$, is minimizing transport artifacts due to the artificial interface formed by the coupling, $W^{L,R}$, and dimensional resonances due to the finite size of the metal clusters included in the extended molecule, while mimicking macroscopic electrodes by providing ample electron flux into and out of the extended molecule. Thus the *geometry* of the constituent metal atoms of the semi-infinite electrodes may be relaxed from that of a full bulk crystal.

In a method similar in spirit to the Bethe lattice approximation employed for similar nanoscale transport systems [69, 70], the finite cross-section body-centered cubic (BCC) or face-centered cubic (FCC) semi-infinite electrodes with 9 valence orbitals per atomic site (that form a non-orthogonal basis as in Reference [64]) are replaced with a set of one-dimensional semi-infinite chains coupled to every orbital of each atom in the two atomic layers of each metal nanocluster that are furthest from the molecule. Thus the total number of the ideal leads connected to a cluster depends on the sizes of the outer layers of the cluster. For example, for clusters such as those designed in the following chapters which include layers of 4×4 and 5×5 atoms for the last two layers of each finite cluster included in the extended molecule, and where each atom in the cluster is described by 9 valence orbitals, this model for the electrodes results in $(4 \times 4 + 5 \times 5) \times 9 = 369$ semi-infinite leads used to model each electrode. Systematic studies carried out in the course of the present work showed that these large number of ideal leads when arranged in the above way have an effect similar to phase-randomizing Büttiker probes [71] in minimizing the influence of dimensional resonances due to the finite size of the metal clusters included in the extended molecule while providing ample electron flux to the junction. Thus substituting sets of one-dimensional leads for transition metal electrodes with full crystal symmetry dramatically increases computation efficiency and permits analytic derivation for the transport calculation outlined in the following section, while maintaining an adequate representation of the molecular wire systems.

The leads are each constructed from a semi-infinite chain of s-type orthogonal atomic orbitals, one orbital per lead site, with spacing (periodicity) a between orbital sites. Thus the electrodes may be parameterized with the tight-binding basis set $\{|n, j\rangle\}$ where n is the unit cell of the ideal lead and j spans the 369 atomic orbitals, one per lead. Each of the one-dimensional leads is decoupled from the others so there is no hopping between different lead orbitals $|j\rangle$. Therefore each individual lead represents an individual channel and the parameterization for the electrodes $\{|n, j\rangle\}$ may be replaced with $\{|n, \alpha\rangle\}$. I.e, an electron may be incident with wave vector k^{α} upon the extended molecule from any channel α of the 369 possible channels of each electrode.

The on-site energy parameters for the leads are $\langle n, \alpha | H^{L,R} | n, \alpha \rangle = \varepsilon^{\alpha}$ where ε^{α} is matched to the site energy of the extended molecule atomic orbital to which the lead is coupled. Since the electronic structure of the extended molecule is an implicit function of bias voltage and electron spin, the site energies of the source and drain leads need not be equal. The hopping energy parameters are $\langle |n, \alpha | H^{L,R} | m, \beta \rangle = \tau \delta_{n,m\pm 1} \delta_{\alpha,\beta}$; only nearest-neighbor hopping between orbitals is included. Identical hopping parameters are assumed for all leads but the parameters may differ on the source and drain electrodes. A moderately large lead bandwidth, or hopping parameter τ, is assumed so that all transmitting modes are real: τ is assumed to be 8 (15) times larger than the $s-s$ nearest-neighbor hopping parameter for a bulk crystal of the particular material [64] in order to partially accommodate for the number of nearest-neighbor hopping elements in physical BCC (FCC) electrodes that are neglected in the one-dimensional lead model.

The coupling Hamiltonian matrix elements, $W^{L,R}_{n,j,n',j'} = \langle n,j|W^{L,R}|n',j\rangle$, between the extended molecule and one-dimensional leads are the only quantities outstanding for the specification of model Hamiltonian (2.7). Since each source (drain) one-dimensional lead α is coupled through its orbital at $n = -1$ ($n = 1$) to the extended molecule at site $n = 0$, only the matrix elements $W^{L}_{0,j,-1,\alpha}$ and $W^{R}_{0,j,1,\alpha}$ and their Hermitian conjugates are non-zero. A lead coupling equal to the spin-dependent nearest-neighbor $s-s$ hopping parameter in the bulk crystal [64] (which is the dominant hopping parameter) multiplied by four in order to partially account for the artificially lower coordination number[9] provided by the model is assumed for $W^{L}_{0,j,-1,\alpha}$ and $W^{R}_{0,j,1,\alpha}$ when j is an atomic orbital in the *last* layer of either metal cluster and α is the one-dimensional lead coupled to it. A non-orthogonal basis is assumed for the coupling Hamiltonians, and the multiplication of four is performed on both overlap and Hamiltonian matrix elements. The coupling to the second-to-last layer of the clusters is not enhanced and is assumed equal to the second nearest-neighbor $s-s$ hopping parameter in the bulk material, consistent with the coordination number for atoms in that layer. Calculated transmission results show no strong sensitivity to these multiplicative parameters. Thus the results presented in the following chapters do not change qualitatively if the parameters of the ideal leads are varied (within reasonable bounds) or an additional layer of metal atoms is included in the clusters.

With the scattering Hamiltonian of Equation (2.7) fully defined, explicit solutions to the Schrödinger equation may now be formulated and the transmission probability predicted. The following section developing the transport methodology assumes that the scattering problem is formulated using an orthonormal tight-binding basis set. Thus Equation (2.5) must first be orthogonalized (as H^{EM} and $W^{L,R}$ are formulated in non-orthogonal bases) at every energy using the transformation [72, 73] summarized in Appendix B.

---

[9] Each atomic orbital in the last two layers of the extended molecule clusters is coupled to only one, one-dimensional lead, whereas in true (100) BCC or FCC electrodes, each interior atom in the last layer has four nearest-neighbor atoms outside the boundary of the extended molecule.

2.8 Quantum Transport in Molecular Wires with Transition Metal Electrodes

The transmission probability required by Equation (2.1) for predicting current is obtained from the conditions imposed on the wavefunction solutions to Equation (2.5) for molecular wires: An electron incident with energy E upon the extended molecule from a particular channel α is partially transmitted through the molecule into drain lead β and partially reflected back into source lead β' as depicted in Figure 2.2. The scattering state solution to the Schrödinger equation with model Hamiltonian (2.7) for an electron incident from lead α may thus be expressed in terms of the reflection $r_{\beta,\alpha}$ and transmission $t_{\beta,\alpha}$ matrices and satisfies different conditions in the left lead (L), right lead (R) and the extended molecule (EM): The total scattering wavefunction is the sum $|\Psi^{\alpha}\rangle = |\Psi^{\alpha}_{L}\rangle + |\Psi^{\alpha}_{EM}\rangle + |\Psi^{\alpha}_{R}\rangle$, with the following conditions

$$|\Psi^{\alpha}_{L}\rangle = \sum_{n=-\infty}^{-1} \left(e^{ink^{\alpha}a}|n,\alpha\rangle + \sum_{\beta'\in L} r_{\beta',\alpha} e^{-ink^{\beta'}a}|n,\beta'\rangle\right) \tag{2.14a}$$

$$|\Psi^{\alpha}_{EM}\rangle = \sum_{i} c^{\alpha}_{i}|0,\phi_{i}\rangle \tag{2.14b}$$

$$|\Psi^{\alpha}_{R}\rangle = \sum_{n=1}^{\infty} \sum_{\beta\in R} t_{\beta,\alpha} e^{ink^{\beta}a}|n,\beta\rangle. \tag{2.14c}$$

Thus, in the left lead, the scattering state is a sum of the incident rightward propagating state and the reflected leftward propagating Bloch states in that lead (all states are propagating as the lead bandwidth is sufficiently large). In the right lead the scattering wavefunction is the sum over transmitted rightward propagating Bloch states. All Bloch states in channels α, β or β' in both leads have energy E. The electron wavefunction on the extended molecule is expressed here in terms of the molecular orbitals of the extended molecule, $|0,\phi_{i}\rangle$, i.e., the eigenstates of the Hamiltonian (2.6).

The conditions (2.14) and the orthogonality of the one-dimensional lead orbitals is used to obtain the transmission amplitude: $t_{\beta,\alpha} = \langle 1,\beta|\Psi^{\alpha}_{R}\rangle e^{-ik^{\beta}a}$. Similarly, the reflection amplitude is $r_{\beta,\alpha} = (\langle -1,\beta|\Psi^{\alpha}_{L}\rangle - e^{-ik^{\alpha}a}\delta_{\beta,\alpha})e^{-ik^{\beta}a}$.

A variety of methods exist for solving the quantum mechanical scattering problem (2.5) with Hamiltonian (2.7) to determine the scattering state solution and thus transmission prob-

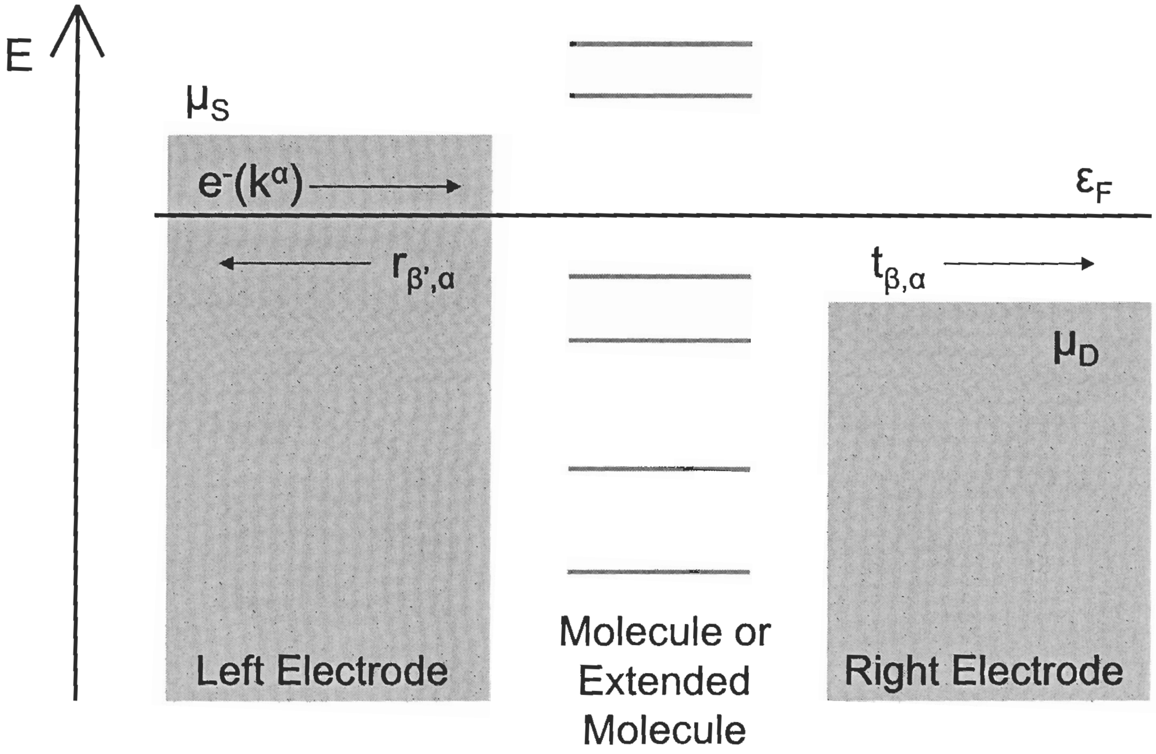

Figure 2.2: Energy level diagram for an electron scattering through a molecular wire. The electron is incident on the molecule from the left electrode and partially reflected back into the left electrode and partially transmitted into the right electrode.

ability. A standard method based on the Lippmann-Schwinger formalism and Green's function techniques [52] is used in this thesis and is outlined briefly next.

The Lippmann-Schwinger equation

$$|\Psi^{\alpha}\rangle = |\Phi_0^{\alpha}\rangle + G_0(E)W|\Psi^{\alpha}\rangle \tag{2.15}$$

is a reformulation of the Schrödinger equation in the language of free propagators [74] or Green's functions. $G_0(E) = G_0^L + G_0^R + G_0^{EM}$ is the Green's function for the decoupled system of left and right electrodes and the extended molecule. Each Green's function is defined individually as $G_0 = (E - H_0 + i\delta)^{-1}$ where H_0 is the Hamiltonian for the decoupled portions of the molecular wire system[10] and δ is an infinitesimally small parameter that

---

[10] It is crucial that the Hamiltonian matrices be orthogonalized using the transformation presented in Appendix B so that they may be physically decoupled from one another.

ensures the contour integral is evaluated in the appropriate portion of the complex plane; positive δ corresponds to the *retarded* Green's function, while negative δ corresponds to the *advanced* Green's function. The latter quantity is not required in the present formulation of quantum transport. $W = W^L + W^R$ is the coupling matrix evaluated in the previous section that describes the coupling between the electrodes and extended molecule. $|\Psi^\alpha\rangle$ is the total scattering state corresponding to the *un-normalized* incident electron state $|\Phi_0^\alpha\rangle$, from which the transmission and reflection coefficients may be extracted via Eqns. (2.14).

The incident electron state $|\Phi_0^\alpha\rangle$ is confined to the *decoupled* left electrode in semi-infinite one-dimensional lead α and thus propagates with energy $E = \varepsilon^\alpha + 2\tau cos(k^\alpha a)$. The one-dimensional model for the semi-infinite leads describing the electrodes presents the simple analytic form of a linear combination of forward and backward propagating one-dimensional Bloch states for the incident eigenstate

$$|\Phi_0^\alpha(k)\rangle = \sum_{n=-\infty}^{-1} (e^{ink^\alpha a} - e^{-ink^\alpha a})|n,\alpha\rangle. \tag{2.16}$$

Different transition metals and geometries will be considered for left and right electrodes in this thesis. However, due again to the simple formulation of the one-dimensional leads, the Green's functions of the left and right electrodes are identical in form and differ only in their energy parameters, ε^α, τ (which are implicit functions of applied bias V and electron spin). The Green's functions, $G_0^{L,R}$, of the electrodes may be expressed in the basis of atomic orbitals $\{|n,\alpha\rangle\}$ used to parameterize the one-dimensional leads

$$G_0^{L,R} = \sum_\alpha \sum_{n=1}^{\infty} \sum_{m=1}^{\infty} (G_0^{L,R})^\alpha_{m,n} |m,\alpha\rangle\langle n,\alpha|. \tag{2.17}$$

For electrodes modeled with one-dimensional leads, the analytical evaluation of $(G_0^{L,R})^{\alpha,\alpha}_{m,n} = (G_0^{L,R})^\alpha_{m,n} = \langle m,\alpha|G_0^{L,R}|n,\alpha\rangle$ is straightforward and is presented in Appendix C.

Similarly, the Green's function for the extended molecule, G_0^{EM}, may be expressed in the basis of molecular orbitals that describe the extended molecule

$$G_0^{EM} = \sum_i (G_0^{EM})^i |0,\phi_i\rangle\langle 0,\phi_i| \tag{2.18}$$

where the matrix elements in the basis of orthogonal molecular orbitals (that diagonalize the Hamiltonian (2.6)) are

$$(G_0^{EM})^{i,i}_{0,0} = (G_0^{EM})^i = \frac{1}{E - \varepsilon_i} \tag{2.19}$$

where ε_i is the energy eigenvalue associated with the molecular orbital ϕ_i of the extended molecule.

Having obtained expressions for all Green's functions, the Lippmann-Schwinger Equation (2.15) may be solved for the scattering wavefunction $|\Psi^{\alpha}\rangle$. The set of states $\{|n,j\rangle\}$ where n spans the constituent cells in the direction of electron propagation of the molecular wire $(-\infty..\infty)$ and j spans the distinct leads α in each electrode and the molecular orbitals ϕ_i of the extended molecule at $n=0$ is orthonormal (once the transformation in Appendix B has been performed). Thus bracketing Equation (2.15) with $\langle n,j|$ one obtains

$$\begin{aligned}\langle n,j|\Psi^{\alpha}\rangle - \sum_{n'=-\infty}^{\infty}\sum_{j'}\sum_{n''=-\infty}^{\infty}\sum_{j''}((G_0^L)_{n,n'}^{j,j'} + (G_0^{EM})_{n,n'}^{j,j'} + (G_0^R)_{n,n'}^{j,j'})\times \\ \times(W^L_{n',j',n'',j''} + W^R_{n',j',n'',j''})\langle n'',j''|\Psi^{\alpha}\rangle = \langle n,j|\Phi_0^{\alpha}\rangle. \qquad (2.20)\end{aligned}$$

The summations in Equation (2.20) simplify greatly as W is zero unless the unit cells (n',n'') are $-1<n<1$. Also, the individual Green's functions are non-zero only on the portions of the molecular wire for which they are defined and all vanish for $j \neq j'$.

Nevertheless, Equation (2.20) describes an infinite set of linear equations with unknowns that run over all atomic orbital sites of the molecular wire. However, since only the quantities $\langle 1,\beta|\Psi_R^{\alpha}\rangle$, $\langle -1,\beta|\Psi_L^{\alpha}\rangle$ and c_i^{α} are required for the evaluation of $t_{\beta,\alpha}$ and $r_{\beta,\alpha}$, only a linearly independent subset of (2.20) need be considered. Thus, $\langle n,j|$ need only span $\langle 1,\beta|$, $\langle -1,\beta|$ and $\langle 0,\phi_i|$ which together with Eqs. (2.14) yield the following set of linear equations

$$e^{-ik^{\alpha}a}\delta_{\beta,\alpha} + r_{\beta,\alpha}e^{ik^{\beta}a} - \sum_i (G_0^L)^{\alpha}_{-1,-1,}W^L_{-1,\alpha,0,i}c_i^{\alpha} = (e^{-ik^{\alpha}a} - e^{ik^{\alpha}a})\delta_{\beta,\alpha} \qquad (2.21a)$$

$$c_i^{\alpha} - \sum_{\beta\in L}(G_0^{EM})^i W^L_{0,i,-1,\beta}[e^{-ik^{\alpha}a}\delta_{\beta,\alpha} + r_{\beta,\alpha}e^{ik^{\beta}a}] - \sum_{\beta\in R}(G_0^{EM})^i W^R_{0,i,1,\beta}t_{\beta,\alpha}e^{ik^{\beta}a} = 0 \qquad (2.21b)$$

$$t_{\beta,\alpha}e^{ik^{\beta}a} - \sum_i (G_0^R)^{\alpha}_{1,1}W^R_{1,\alpha,0,i}c_i^{\alpha} = 0. \qquad (2.21c)$$

Thus Equation (2.20) is reduced to a finite set of simultaneous linearly independent equations that can be solved for the unknowns $r_{\beta,\alpha}$, $t_{\beta,\alpha}$ and c_i^{α} for an electron incident in each channel α with energy E with standard numerical linear equation solving techniques.

The total transmission probability for electrons to enter the right electrode from the left electrode is given by

$$T(E,V) = \sum_{\alpha \in L} \sum_{\beta \in R} \frac{|v_\beta|}{|v_\alpha|} |t_{\beta,\alpha}|^2 \tag{2.22}$$

where v_α is the velocity of the electron in the rightward propagating state in left lead α, and v_β is the velocity of the rightward propagating state in right lead β at energy E. Similarly, the total reflection probability is

$$R(E,V) = \sum_{\alpha \in L} \sum_{\beta \in L} \frac{|v_\beta|}{|v_\alpha|} |r_{\beta,\alpha}|^2 \tag{2.23}$$

where v_β is the velocity of the electron in the leftward propagating state in left lead β. Unitarity requires that $T(E,V) + R(E,V) = N$ where N is the number of incident electron channels (i.e., the number of 1D source leads or 369).

Generalizing for non-degenerate electron spin (molecular wires with ferromagnetic electrodes), the transmission probability may be expressed as

$$T(E,V) = \sum_{\alpha \in L} \sum_{\beta \in R} \sum_{s,s'} \frac{|v_{\beta,s'}|}{|v_{\alpha,s}|} |t_{\beta,s';\alpha,s}|^2 \tag{2.24}$$

where $t_{\beta,s';\alpha,s}$ is the transmission amplitude from a state of ideal lead α of the source electrode with spin s to a state of ideal lead β of the drain electrode with spin s' and $v_{\alpha,s}$ and $v_{\beta,s'}$ are the corresponding electron velocities. If spin flips during transmission of electrons through the junction are neglected as in the present work and the summations over spin in Equation (2.24) for T are restricted to a particular spin orientation then Equation (2.1) yields the current for that spin orientation, i.e., $I_\uparrow$ or $I_\downarrow$. For degenerate spin $I_\uparrow = I_\downarrow$ and the current calculated via Equation (2.1) is multiplied by 2.

2.9 Finite Bias and the Electrostatic Potential

The Hamiltonian matrix elements of Equation (2.7) and consequently the matrix elements in Equations (2.21) including the transmission and reflection coefficients are implicit functions of applied bias voltage V. Thus the transmission probability (2.22) that enters the Landauer expression (2.1) for the electronic current I flowing in a system depends on the applied bias voltage V as well as electron energy E. A bias voltage applied between the two terminals of a molecular wire introduces an imbalance between the chemical potentials of the source μ_S and drain μ_D electrodes and a net current is induced to flow in the direction of positive applied bias according to Equation (2.1). Thus for net electron flux incident from the source electrode, the drain electrode must be at higher electrostatic potential ϕ than the source; a potential difference exists between the source and drain electrodes that establishes an electric field in the vicinity of the molecule. The spatial details of that electric field are described by an electrostatic[11] *potentialprofile*. Since most of the interesting transport phenomena predicted in this thesis occur outside of the linear voltage response regime, the effects of *finite* bias must be included explicitly for realistic modeling.

The electrostatic potential profile of a molecular wire arising from an applied bias voltage is difficult to calculate from first principles since it is a non-equilibrium many-body property and may be sensitive to charging and screening effects. However, in Ref. [58], it has been shown by comparison with the results of *ab initio* calculations (that include the electronic correlation energies of molecular wires and their electric field dependence in a mean field approximation) that the effects of screening and capacitive charging of the electrodes on transport in simple molecular wires can be modeled accurately by employing appropriate phenomenological potential profiles between the metal contacts. This approach is adopted in this text: In each of the mesoscopic transport systems considered, the entire bias is assumed to drop over the narrowest constriction (the molecule or a pair of metal tip atoms) of the junction. This is consistent with the efficient screening of the electric field by electrons in metals; the electric field extends only a very short distance across the metal-molecule interface. The details of the phenomenological potential profile in the vicinity of the molecule will be explored for each of the specific systems presented in the following chapters.

All metal atoms (and ideal leads) to the source side of the molecule are therefore assumed to be at a potential $\phi = -\frac{V}{2}$, while metal atoms and leads to the drain side are at $+\frac{V}{2}$ for bias voltage V applied to the drain. In each case the electrostatic potential modifies the diagonal matrix elements of the tight-binding Hamiltonian (2.7) of the molecular wire system which become $H_{i,i} = H^0_{i,i} - e\phi_i$ where $H^0_{i,j}$ is the tight-binding Hamiltonian matrix at

---

[11] Consideration of electrostatic potential profiles is appropriate here since steady-state conditions are assumed throughout this thesis.

zero bias and ϕ_i is the electrostatic potential ϕ at the site occupied by atomic orbital i. As the tight-binding basis is non-orthogonal, the electrostatic potential also modifies non-diagonal Hamiltonian matrix elements. This effect is included approximately in the form

$$H_{i,j} = H^0_{i,j} - eS_{i,j}(\phi_i + \phi_j)/2. \tag{2.25}$$

Equation (2.25) may be understood from the summary presented in Appendix A.

2.10 Mulliken Analysis

Throughout this thesis it will be useful to examine particular Hamiltonian eigenstates $|\Psi_k\rangle$ in terms of the wavefunction weight that resides on certain atoms or orbitals. However since the atomic orbital bases employed throughout this work are non-orthogonal[12], the norm of the eigenstate $\langle\Psi_k|\Psi_k\rangle$ contains overlap terms that are not rigorously separable. Thus the resolution is somewhat arbitrary.

The methodology employed in this thesis for eigenstate resolution is based on the analysis by Mulliken and is performed as follows: Consider the normalized eigenstate $|\Psi_k\rangle = \sum_i c_{k,i}|i\rangle$ of the Hamiltonian, where $|i\rangle$ is an atomic orbital. Express the norm of the eigenstate in terms of the contributions of all atomic orbitals of the system as

$$\langle\Psi_k|\Psi_k\rangle = \sum_{i,j} c^*_{k,i}c_{k,j}S_{i,j} \tag{2.26}$$

where $S_{i,j} = \langle i|j\rangle$. To resolve the eigenstate $|\Psi_k\rangle$ into its atomic or orbital components the Mulliken weight

$$c^*_{k,i}c_{k,i} + \sum_{j\neq i}(c^*_{k,i}c_{k,j}S_{i,j} + c^*_{k,j}c_{k,i}S_{j,i})/2 \tag{2.27}$$

is assigned to each atomic orbital i. Hence the contributions of overlapping atomic orbitals are arbitrarily assigned with equal weight to the two orbitals involved.

---

[12] The orthogonalization procedure of Appendix B is energy-dependent and thus is not suitable for this purpose.

Chapter 3

Spin-dependent Transport in Atomic Fe Nanocontacts

3.1 Introduction

Spin-dependent transport (SDT) phenomena occur when a bias voltage is applied across a junction between materials one or both of which are magnetic [35, 36, 37]. They include partial or complete spin polarized injection of electric current and changes in the electrical resistance when the magnetization direction of one of the magnetic components of the system is reversed through the application of a magnetic field. The latter effect is usually referred to as "tunneling magnetoresistance" (TMR) or "giant magnetoresistance" (GMR) and has important technological applications including read head sensors for magnetic storage devices (hard drives) and magnetic random access memory (MRAM). SDT has been observed at interfaces between ferromagnetic metals and superconductors [75], between ferromagnetic and normal metals [76], between ferromagnetic metals separated by thin insulating films [77], and more recently between magnetic semiconductors and nonmagnetic semiconductors [78, 79].

Iron, nickel and cobalt are ferromagnetic because the exchange interaction due to the Pauli exclusion principle reduces the Coulomb repulsion energy of electrons with *parallel* spin. Thus ferromagnetic metals are characterized by spin-split energy bands with majority electron bands at lower energy than minority bands and unequal populations of spin *up* and spin *down* electrons that produce a spontaneous net magnetization. Two ferromagnetic source and drain electrodes that are connected via a conducting junction can form two separate magnetic domains whose magnetizations (i.e., net unpaired electron spins) may be manipulated independently through the application of magnetic field[1]. For anti-parallel magnetizations of the source and drain, *majority (minority)* electrons in the source are transported (in the absence of spin-flip processes) across the junction under bias voltage into *minority (majority)* bands in the drain. The majority spin in *each* contact is referred to as "spin *up*" and the minority spin as "spin *down*". Thus if an electron is transmitted between contacts with anti-parallel magnetizations without changing its spin orientation, the transition is referred to as a spin *up* → spin *down* or spin *down* → spin *up* transition. The energy band mismatch typically produces larger scattering and thus electrical resistance for anti-parallel than parallel magnetizations resulting in magnetoresistance.

The magnetoresistance (MR) is defined as

$$MR = \frac{I_P - I_{AP}}{I_{AP}} \tag{3.1}$$

where I_P (I_{AP}) is the electric current flowing between the ferromagnetic nanocontacts when their magnetizations are parallel (anti-parallel).

The energy band spin-splitting of a ferromagnetic electrode may also produce a spin *up* current $I_\uparrow$ that is different from the spin *down* current $I_\downarrow$ flowing across the junction and partial or complete spin polarized injection of current into another magnetic or non-magnetic contact is possible. Thus another SDT quantity of relevance is the spin injection factor and is defined as

$$\eta = \frac{I_\uparrow - I_\downarrow}{I_\uparrow + I_\downarrow}. \tag{3.2}$$

At the present time spin-dependent transport through *nanoscale* junctions is attracting increasing attention. SDT through chains of atoms or single atoms[2] connecting pairs of nickel and cobalt nanocontacts has been investigated theoretically [70, 80, 81, 82, 83]. Such systems have been realized experimentally using break-junction [84, 85, 86, 87, 88] and

---

[1] Independent rotation of electrode magnetization vectors is typically accomplished experimentally through the fabrication of spatially asymmetric contacts so that each consists of a magnetic domain of a different size.

[2] In addition interest in SDT through junctions bridged by organic molecules is growing and is the subject of Chapter 4.

electrochemical [89] techniques and transport measurements on them have been carried out [84, 85, 86, 87, 88, 89]. SDT measurements have also recently been carried out on iron atomic contacts [88, 90].

Spin-dependent transport through Fe atoms connecting Fe nanocontact electrodes (forming a quantum point contact or QPC) will be explored theoretically [48] in this chapter. Fe QPCs are physically rich enough to elucidate the systematics and complexities of SDT in nanoscale systems, yet not quite as intricate as the ferromagnetic metal-organic systems that are the subject of the following chapter. The comprehensive study of transport in Fe QPCs also provides a basis for which to compare and understand the factors that affect electron transport in nanoscale systems with other transition metal electrodes. Considerations of primary importance will be revealed to be: explicit inclusion of finite bias effects, for which qualitative differences from models that neglect bias effects are predicted, and the influence on transport characteristics by the densities of states of the electrodes.

The chapter begins with an introduction to Julliére's classical theory for spin-dependent tunneling. The Julliére model relates the MR that is attainable for particular systems to experimentally measured spin polarizations for the individual contact materials. However, in the sections that follow, it will be shown that the Julliére formula in its simplest form does *not* contain useful information relating to spin-dependent transport between QPCs. The tight-binding model for the electronic and magnetic structures of the ferromagnetic contacts that is obtained from fitting the known band structure of magnetic bulk Fe [64] (as introduced in Chapter 2) is discussed in detail in Section 3.3 and its applicability to structures possessing surfaces and nanoscale contact geometries is investigated: It will be demonstrated that the model incorporates in an approximate way *both* the bulk and surface magnetic properties of Fe which together influence SDT through a junction of bulk Fe electrodes that come together at a nanocontact, as in experimental realizations of Fe QPCs. In the following sections, the methodology developed in Chapter 2 will be applied to study SDT in different arrangements of Fe atoms connecting the ferromagnetic contacts: Section 3.4 begins by considering a structure in which the positions of the atoms of the Fe nanocontacts and of the atomic bridge connecting them coincide with sites of an Fe crystal. The application of finite bias across the junction of the Fe contacts is considered explicitly and unusual SDT phenomena including *negative* magnetoresistance are predicted. In the next section, more general geometries will be considered in which the separation between the nanoclusters is allowed to vary, as occurs in break-junction experiments. To this end, the tight-binding model of the electronic structure of the Fe clusters will be supplemented by introducing a position-dependent parameterization for the electronic coupling between clusters, in the spirit of extended-Hückel theory. The separation between the tips of the clusters is then varied from a bulk nearest-neighbor distance, in which case ballistic SDT is predicted, to a distance at which the atomic bridge has been broken where vacuum-tunneling-like SDT occurs. The cross-over regime will be examined and interesting phenomena are predicted, including pronounced spin-dependent transport resonances mediated by dangling bonds that form on the tip atoms. Finally, the spin-dependent current and magnetoresistance are examined explicitly for the case of tunneling between ferromagnetic nanoscale tips separated by vacuum.

3.2 Julliére Model for Spin-dependent Transport

The Julliére model for spin-dependent tunneling between two ferromagnetic electrodes relates the magnetoresistance that may be attained for the device to the spin polarization P of each electrode [77]. The spin polarization of each electrode[3] is often defined in terms of spin *up* and spin *down* densities of states (DOS) (typically at the Fermi energy) that contribute to transport, $n_\uparrow$ and $n_\downarrow$ respectively so that

$$P = \frac{n_\uparrow - n_\downarrow}{n_\uparrow + n_\downarrow}. \tag{3.3}$$

The classical model assumes that the transmission probability (and thus the current) is proportional to the product of spin-dependent densities of states of the electrodes on either side of the tunnel junction (e.g., $I_\uparrow \propto n_{1\uparrow} n_{2\uparrow}$). Hence, the Julliére formula for magnetoresistance may be expressed explicitly as

$$MR = \frac{2P_1P_2}{1 - P_1P_2} \tag{3.4}$$

for spin polarizations P_1 and P_2 of the two electrodes.

Numerical values for the spin polarization P of each electrode are often obtained from experiments that measure spin injection from ferromagnetic materials into superconducting

---

[3] The spin polarization of the electrode is related to, but should not be confused with, the spin injection factor defined in Equation (3.2).

electrodes [75]; values for the spin polarization obtained in this way are $P = .31$ for Ni and $P = .45$ for Fe [91]. For Fe, the measured value is in reasonable agreement with the estimate obtained from considering the Fe DOS (Equation (3.3)) (see Figure 3.1(d)), while for Ni the DOS estimate predicts the incorrect sign (as $n_\downarrow > n_\uparrow$ for Ni DOS at the Fermi energy) (see Ref. [64]). Nevertheless, reasonable estimates for magnetoresistances in some magnetic tunnel junctions (MTJs) with a range of electrode materials have been obtained from the Julliére formula together with these experimental spin polarizations [92]. This apparent discrepancy may be resolved by recognizing that wavefunctions for valence d-electronic states of the ferromagnetic electrodes, having lower energy than those for s-electrons, decay very quickly in the insulating barrier of the MTJ and thus contribute less efficiently to the conductance [92, 93, 94, 95, 96, 97, 98][4]. Therefore d-electrons that are responsible for the strongest features in the densities of states for magnetic electrodes do not play an active role in transmission in such insulator-mediated systems. Thus the measured spin polarizations [91] often provide a reasonable estimate for the ratios of spin *up* to *down* electrons that *contribute* to transport in conventional MTJs.

However, in QPC systems, the magnetic electrodes are in physical contact and so d-electrons contribute effectively to transport. Thus, the *full* DOS for the electrodes may be expected to accurately describe electrons that contribute to transport in nanoscale systems; together with the Julliére formula, the DOS may be expected to accurately predict the MR.

However the magnetoresistance of conventional MTJs is a property of not only the electrode, but also strongly sensitive to the electrode-insulator interface [95, 96, 98, 100, 101, 102, 103, 104, 105, 106, 107]: The magnetoresistance of thin film MTJs has been experimentally shown to be sensitive to the choice of insulating barrier [103, 104]. States that form at the ferromagnet-insulator interface have been predicted to dominate transport (in the minority spin channel) for thin insulating film Fe/MgO/Fe MTJs [96, 101]. Also, insertion of ultra-thin metal interface layers, including Au or Cr for example, between the ferromagnetic electrode and insulating barrier has been reported to modify the interface density of states (and thus the transport and MR) for similar MTJ systems [105, 106].

---

[4] This decay is further enhanced by the conservation of wavevector parallel to the interface (conventional MTJs such as those formed with thin metal-oxide insulating films are assumed periodic structures in the direction perpendicular to electron propagation) [92, 96, 99, 100, 101]. In QPC systems, however, such as those studied in this chapter, there is no lateral periodicity and transverse wavevector conservation is broken.

For ferromagnetic systems bridged with molecules or atoms, interface effects are expected to be *at least* as important; in the following chapters the conduction is predicted to be dominated completely by interface effects at moderate bias voltages. Thus the Jullière formula in its simplest form can not be accurate if the spin polarizations that enter Equation (3.4) are obtained from considerations of the electrodes *alone* (either from experimental values or DOS considerations). However, the Jullière model may be reconciled with the results of more sophisticated quantum spin transport calculations if the calculations of the spin polarizations are generalized to reflect the *interfacial* transmission at each contact [101]. Such a generalization requires a full quantum mechanical calculation, and resolution of the total transmission into contributions due to the different interfaces is difficult for systems under an applied bias voltage (which is a primary result of this chapter). A molecular system for which the generalized definition of spin polarizations under bias is tractable will be discussed at the end of Chapter 4. In the meantime, however, as the spin polarizations that trivially enter Equation (3.4) do not properly account for the effects of the atomic interface, the classical Jullière model will be shown inadequate for predicting SDT through Fe QPCs.

3.3 Tight-binding Model and Applicability to Nanoscale Geometries

The microscopic transport calculation introduced in Chapter 2 requires knowledge of the underlying electronic structure of the Fe QPC system; experimental systems of the type investigated in Refs. [88, 90] are very difficult to characterize on the atomic scale and may involve atomic reconstructions of the electrodes near the nanoscale junction. On the other hand, micron-scale Fe whiskers with (100) surface orientations have been fabricated and characterized [108], and many studies have been reported also on conventional MTJs with Fe (100) electrodes [95, 96, 101, 108]. The present system of interest consists of two bulk ferromagnetic metal electrodes that act as a source and drain for electrons, joined by a nanoscale QPC junction of atoms of the same magnetic metal. This structure is modeled as a connected pair of nanoscale contacts of (100) body-centered cubic iron, each contact consisting of a 55 atom cluster built from $5 \times 5, 4 \times 4, 3 \times 3, 2 \times 2$ layers of atoms, terminated with a single tip atom that is assumed positioned over the hollow site formed by the 2 × 2 layer. Thus the QPC bridging the nanocontacts is modeled as a dimer consisting of the two tip Fe atoms and all atoms are arranged so that they fall on sites of a bulk Fe crystal lattice.

The Hamiltonian describing the extended-molecule (Eqn. (2.6)) for an Fe QPC system may be replaced with

$$H^{EM} = H_C^L + H_C^R + W, \tag{3.5}$$

i.e., there is no organic molecule and H^M may be omitted. The electronic structure of the Fe clusters is described by a tight-binding Hamiltonian using a non-orthogonal basis of s, p and d-atomic orbitals, a total of 9 orbitals per atom for each spin orientation. The values of the Hamiltonian $H_C^{L,R}$ and overlap matrix elements are taken from Ref. [64] as described in Section 2.6. These tight-binding parameters are based on fits to *ab initio* band structures calculated for Fe crystals [64]; parameters from Ref. [64] have previously been employed successfully to study conventional MTJ systems involving Fe and other magnetic metals together with insulating or vacuum tunnel barriers or non-magnetic metal spacers [94, 95, 97, 102, 109] and magnetic [81] and non-magnetic [110] atomic nanoscale systems. Moreover, tight-binding parameters taken from Ref. [64] have been used to model platinum nanocontacts and the resulting transport properties have been shown to agree with a density functional theory description [111].

For parallel magnetizations on two contacts that simultaneously occupy sites of a perfect BCC crystal lattice, the off-diagonal matrix elements, W, connecting orbitals having the *same* spin orientation in opposite clusters may also be obtained from Reference [64]. As in in Ref. [64], all Hamiltonian and overlap matrix elements connecting orbitals having opposite spin orientations are taken to be zero, i.e., spin flips during electron transmission through the junction are not considered. The transport calculation of Chapter 2 is generalized for non-degenerate spin by applying independently spin *up* and *down* tight-binding parameters, i.e., s and s' are restricted in Eqn. (2.24) to particular spins and Eqn. (2.1) yields the current for that spin orientation. The total current is $I = I_\uparrow + I_\downarrow$. The tight-binding parameter set is modified and/or extended appropriately (as discussed below and in Section 3.5.2, respectively) when a magnetic domain wall is present or the positions of the atoms of the junction do not all coincide with sites of a perfect BCC Fe crystal lattice.

Each cluster (including the tip atom) and the semi-infinite leads connected to it for the transport calculation are assumed to form a single magnetic domain. Thus, if the magnetizations of the two nanocontacts are anti-parallel, an atomically thin, hard domain wall is present at the midpoint of the Fe dimer connecting the two clusters, in accordance with the calculation of Ref. [112] and with previous work modeling SDT in Ni atomic contacts [70]; the magnetization vector rotates 180^o at the hard domain wall. The tight-binding parameters developed in Ref. [64] do not include the off-diagonal Hamiltonian or overlap matrix elements between atomic orbitals located on opposite sides of a magnetic domain wall. However the published off-diagonal matrix elements connecting spin *up* orbitals are not very different from the corresponding matrix elements connecting spin *down* orbitals in the same domain [64]. This is physically reasonable given that the spatial part of a spin *up* orbital should be similar to that of the corresponding spin *down* orbital. Thus in the present work, when geometrically applicable, the off-diagonal matrix elements, W, connecting orbitals that are on *opposite* sides of an atomically thin domain wall (having the appropriate spin orientation) are approximated by the average of the spin *up* and spin *down* matrix elements connecting the corresponding orbitals in a single domain.

To better understand the significance of the results of the SDT calculations presented in the following sections it will be useful to compare them to particular features of the spin-resolved surface and bulk densities of states of the Fe electrodes that are parameterized with the tight-binding model presented above and to further resolve the density of states into its s, p and d components; 100,000 random k points were used to generate a representation of the density of states for spin *up* and *down* electrons in bulk Fe. The partial and total bulk densities of states resolved with the Mulliken analysis presented in Chapter 2 are shown in Fig. 3.1(a-d).

In order to assess the applicability of the semi-empirical tight-binding model (that is based on fits to bulk band structures) to nanostructures that include surfaces, the local magnetic moment per atom in the (100) surface atomic layer and in the interior of large Fe clusters (with nearly 400 atoms) was calculated. A similar Mulliken analysis to that described in Chapter 2 was used to resolve the electron probability distributions for individual eigenstates of the tight-binding Hamiltonian used in the present work into surface and interior contributions. The lower coordination number and lack of symmetry at the surface was found here to result in enhanced magnetic moments at the surface, approximately $2.5\mu_B$ per atom at the surface versus $2.2\mu_B$ in the bulk for this model, a result qualitatively similar to that of *ab initio* surface calculations for (100) Fe ($2.25\mu_B$ in the bulk and $2.98\mu_B$ at the

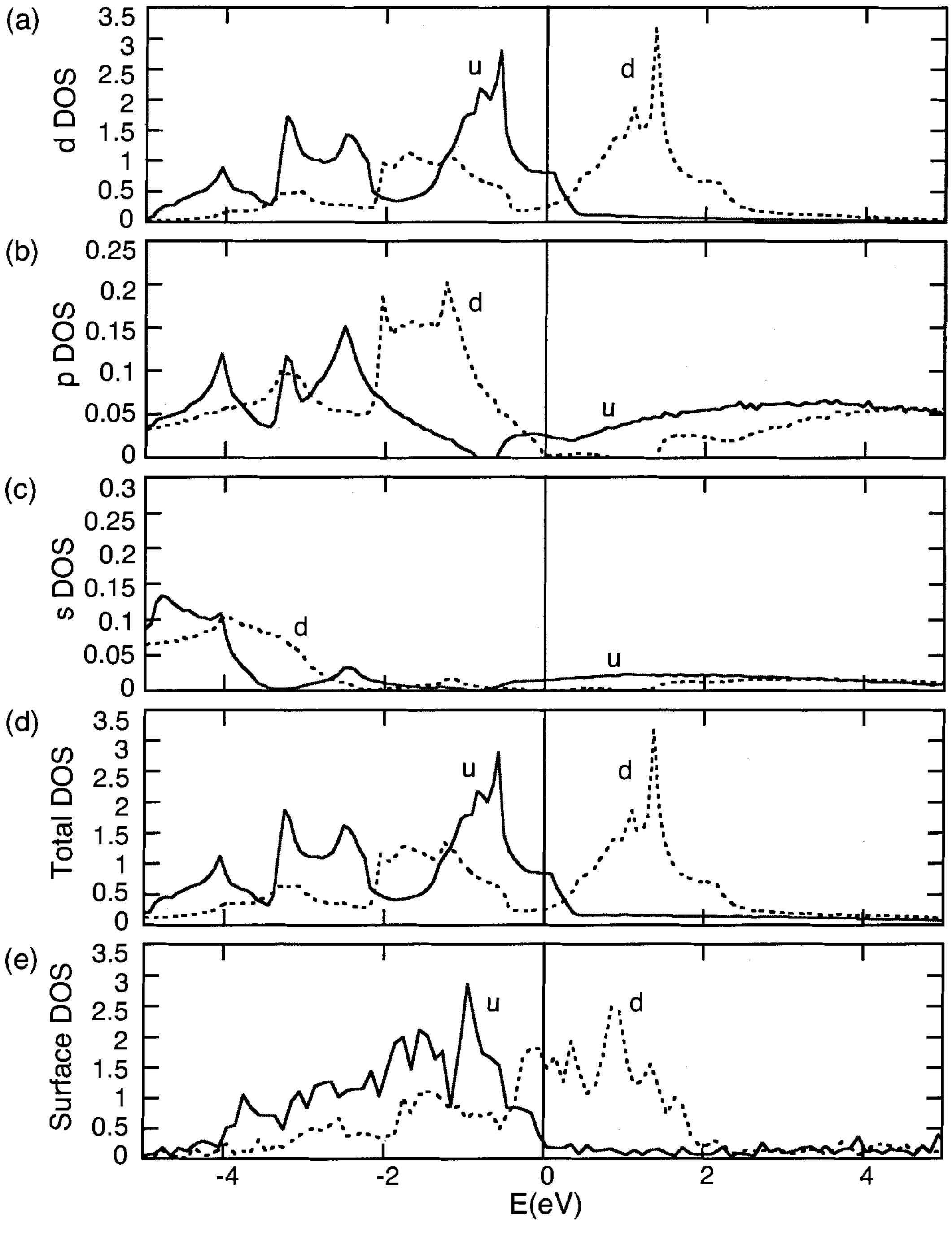

Figure 3.1: Calculated partial (a-c) and total bulk (d) and (100) surface (e) densities of states vs. energy (eV) at zero bias for spin *up* (solid curve u) and spin *down* (dotted curve d). The Fermi energy is located at $0eV$.

surface) [113]. Mulliken analyses arbitrarily assign half of the probability contribution that is due to overlaps between two atoms in Equation (2.26) to each of the two atoms involved and therefore tend to underestimate differences between the electronic populations of adjacent atoms, often significantly. Thus the level of agreement between the present model and the *ab initio* surface calculations [113] is regarded as satisfactory. The contributions from the (100) surface layer of a representative Fe cluster to the spin *up* and spin *down* densities of states obtained in this way are shown in Figure 3.1(e) and compare well with those reported in Ref. [113].

As further indication that the semi-empirical model is appropriate for describing also the nanocontact region (the two tip atoms comprising the Fe QPC) in addition to the rest of the contacts approximating bulk electrodes, the model was employed to predict magnetic moments of *actual* Fe nanoclusters of increasing size. The results of this calculation are compared to those of *ab initio* calculations on identical nanoclusters [114] in Figure 3.2(a-d). Solid lines correspond to the present study, dashed lines to the first principles calculations of Šipr *et al* [114]. It is evident that the predicted moments of the semi-empirical model compare well to those of the *ab initio* study for both the surface and interior atoms of the clusters, particularly when the cluster size resembles that of the nanoclusters used for the transport calculation (51 and 59 atom clusters compared to the 55 atom clusters employed for transport in the following sections). The good agreement for the outermost atoms of the clusters is considered indication that the model adequately reproduces the magnetic properties of even atoms of low coordination number, such as the two tip atoms of the clusters in the transport calculations. Additionally, as the nanocluster size is increased (to the 51 and 59 atom sized clusters), the magnetic moments of all of the interior atoms quickly approach that of the bulk. Therefore these results also provide further evidence that the Fe clusters employed in the transport calculations are large enough to model macroscopic magnetic Fe electrodes (with single atom tips) if the above semi-empirical tight-binding model is used to treat the electronic and magnetic structures of these systems.

The above tight-binding model will be applied to study SDT through Fe QPCs with a number of contact geometries in the following sections.

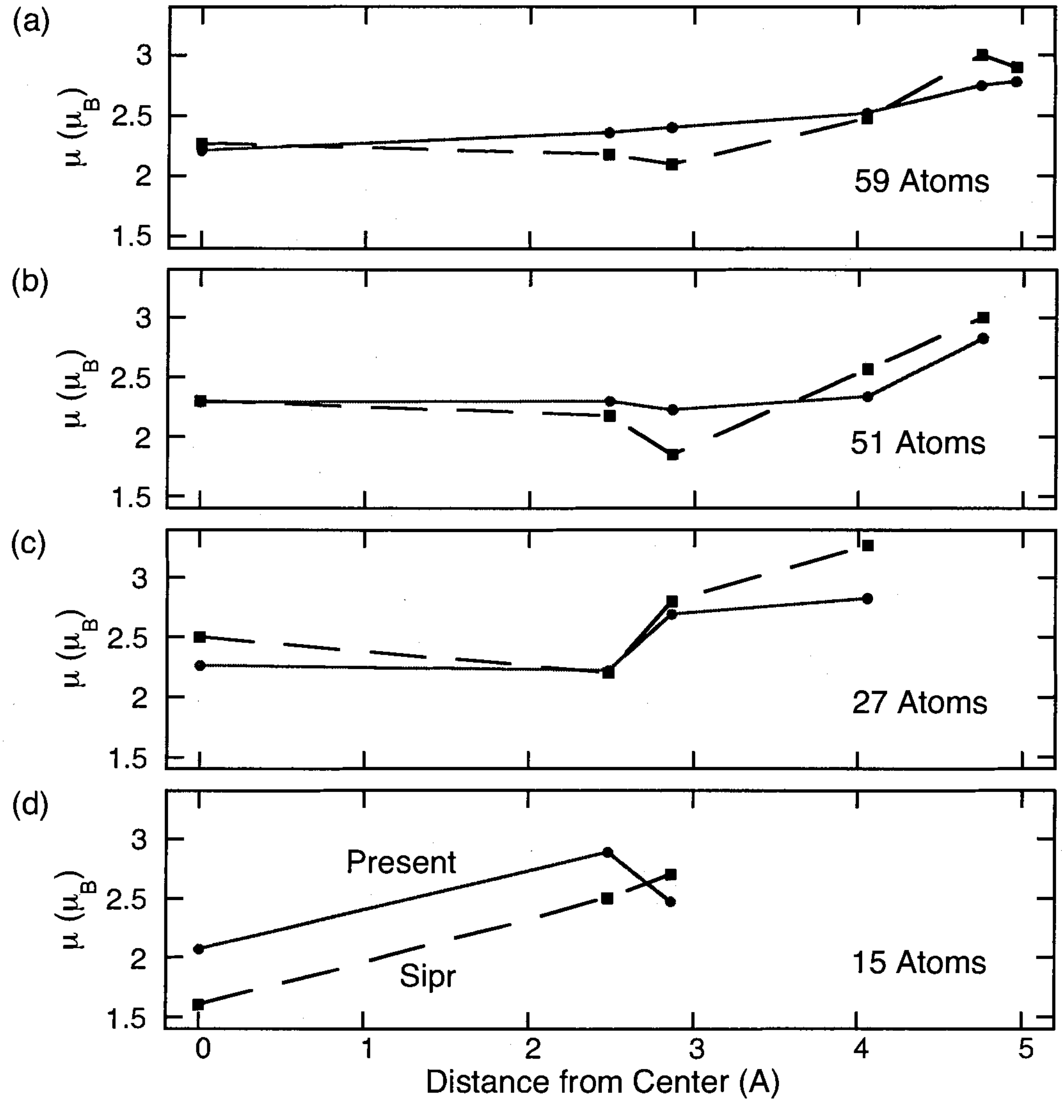

Figure 3.2: Magnetic moments per atom vs. atom distance from the central atom of Fe nanoclusters. All atoms are at bulk lattice positions. Cluster size is increased as coordination shells are added. (a) 59 atom Fe cluster. (b) 51 atom cluster. (c) 27 atoms. (d) 15 atoms.

3.4 Fe Nanocontacts Bridged by Fe Atoms in a BCC Nearest-Neighbor Geometry

The QPC geometry displayed in Figure 3.3 is considered first. The two 55 Fe atom clusters are placed so that the atom terminating the tip of each cluster is at a bulk nearest-neighbor

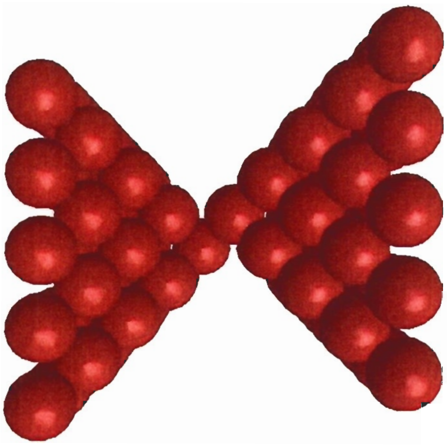

Figure 3.3: Extended molecule for an Fe QPC in a BCC geometry. Each cluster consists of 55 Fe atoms. All atoms coincide with sites of a (100) BCC Fe crystal lattice.

position relative to the tip atom of the other cluster. Thus all atoms occupy positions that match sites of a body-centered cubic Fe bulk lattice so that a tight-binding Hamiltonian and overlap matrix for the entire structure can be constructed using the parameter set of Ref. [64] as described above. Sets of ideal one-dimensional leads (as described in Section 2.7) are used to model source and drain reservoirs for the transport calculation.

The $up \rightarrow up$ (u) and $down \rightarrow down$ (d) transmission probabilities calculated via Equation (2.24) for parallel magnetization of the two contacts at zero bias are shown in Figure 3.4(a) for this geometry. The Fermi energy is at $0eV$. The $up \rightarrow down$ transmission for anti-parallel magnetization is shown in Figure 3.4(b) (detailed balance dictates that at zero bias $T_{up \rightarrow down} = T_{down \rightarrow up}$). The transmission characteristics depend somewhat on the specific details of the chosen geometry, such as cluster size and shape. However, quite similar results are obtained when a 6×6 atom layer is added to each of the clusters. Current and magnetoresistance results (in the following figure) are also robust to geometrical changes, such as addition of a 6×6 layer, or deletion of the 5×5 layer that terminates the nanocluster, indicating that the clusters and ideal leads in the present model adequately represent real (macroscopic) Fe leads.

For this geometry, the calculated spin $up \rightarrow up$ transmission, perhaps surprisingly for a transition metal, exhibits a fairly flat plateau close to unity near and above the Fermi energy.

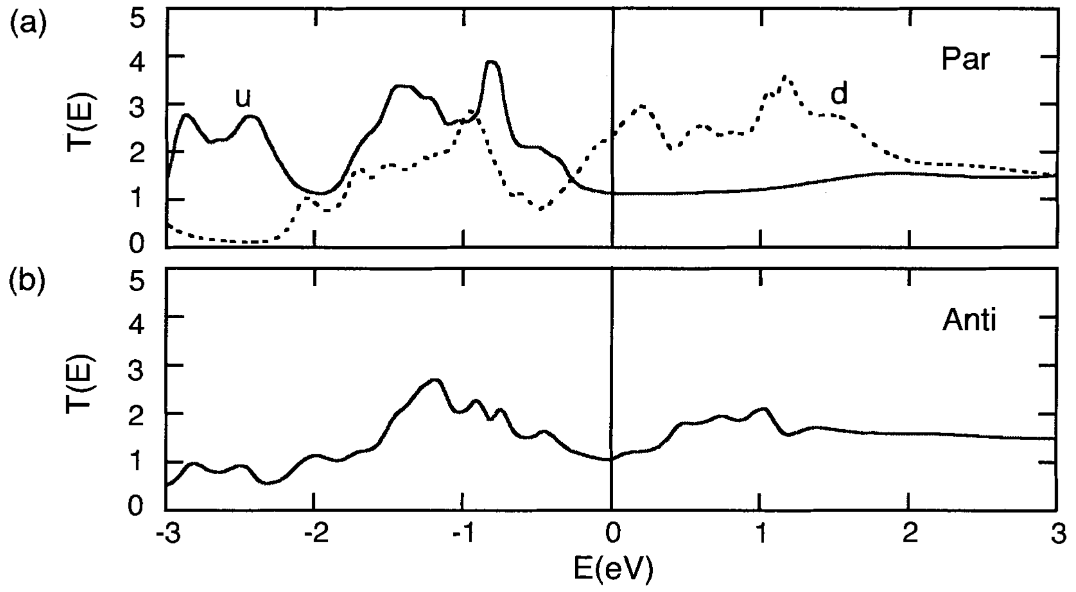

Figure 3.4: Transmission probabilities as a function of energy (eV) at zero bias for the BCC contact geometry in Figure 3.3. (a) Spin *up* → *up* (u) and *down* → *down* (d) transmission probabilities for parallel magnetization of the two contacts (b) Spin *up* → *down* transmission for anti-parallel magnetization. The Fermi energy is located at $0eV$.

As for atomic chains constructed from some non-magnetic metals [110], this roughly unity transmission for spin *up* electrons is not due to a single open conducting channel, but to the superposition of partially conducting channels. By systematically switching off the tip atom-to-tip atom coupling for different atomic orbital symmetries, it is deduced that the *up* → *up* transmission near the Fermi energy is due primarily to s and p-electrons, even though as is seen in Figure 3.1 the spin *up* density of states due to d-electrons is comparable to those due to s and p-electrons above the Fermi energy. Below the Fermi energy, the bulk and surface densities of states for *up* electrons are larger (primarily d-like), and the predicted transmission is also higher.

In contrast to the spin *up* case, the spin *down* → *down* transmission near the Fermi energy, not only shows a strong contribution from p-type electrons but a very strong d-electron component; s-electrons do not seem important in this case. This also can be contrasted to the spin *down* densities of states very near the Fermi energy where that due to p-electrons is small and comparable to that for s-electrons. Yet the presence of many common features that can be observed in the calculated transmission and the surface and bulk densities of states supports the conclusion that the spin transport properties of this magnetic system are influenced by the densities of states. This is reasonable as the DOS reflects the number of open conducting channels for a representative atom at particular energies. The transmission in Figure 3.4 is dominated by transport mediated by open conducting channels on the two tip atoms which are, at least partially, reflected in the bulk and surface DOS; the d-orbital tight-binding on-site energy parameters which are close to E_F for spin *down* electrons and approximately $0.8eV$ below E_F for spin *up* electrons [64] (and mediate transmission on the tip atoms near those energies) are well represented by peaks in the surface DOS and the transmission in Figure 3.4. However, the transmission characteristics can not be determined from solely a knowledge of the densities of states (i.e., from a semi-classical picture); characteristics such as the near quantum conductance above the Fermi energy in the spin *up* channel and the magnitudes of the transmission features can not be deduced from the densities of states alone. Those characteristics can be determined only from a full quantum transport calculation such as that presented here.

The transmission probability, $T(E,V)$, that enters the Landauer expression (2.1) for the electric current I flowing through the QPC depends on the applied bias voltage V as well as the electron energy. The bias dependence of T depends on the electrostatic potential profile through the nanocontact as described in Section 2.9. A heuristic approach to modeling the electrostatic potential profile is adopted in this thesis: Results obtained for a variety of simple models are compared next. The bias, V, is applied symmetrically so that the window of conduction (the limits of integration in Eqn. (2.1)) spans $\pm\frac{eV}{2}$ on either side of E_F.

Figure 3.5(a) shows the current[5] calculated by approximating $T(E,V)$ with $T(E,0)$, an approximation commonly used to study transport in the linear response regime (low values of applied bias) and recently adopted to study finite bias transport in molecular wires with gold electrodes (see for example Refs. [25, 26, 27, 30]). In Figure 3.5(a) the calculated current is higher for parallel magnetization than for anti-parallel magnetization and steadily increases with applied bias, characteristic of ballistic transmission. The calculated MR, as defined by Eq. (3.1) is positive and larger at low bias, decaying to a lower value of about 15% at high bias. It remains positive for all values of bias voltage.

---

[5] $I(-V) = -I(V)$ as the system is mirror symmetric in the direction of electron propagation. Thus current results for negative bias voltages are not displayed in Figure 3.5.

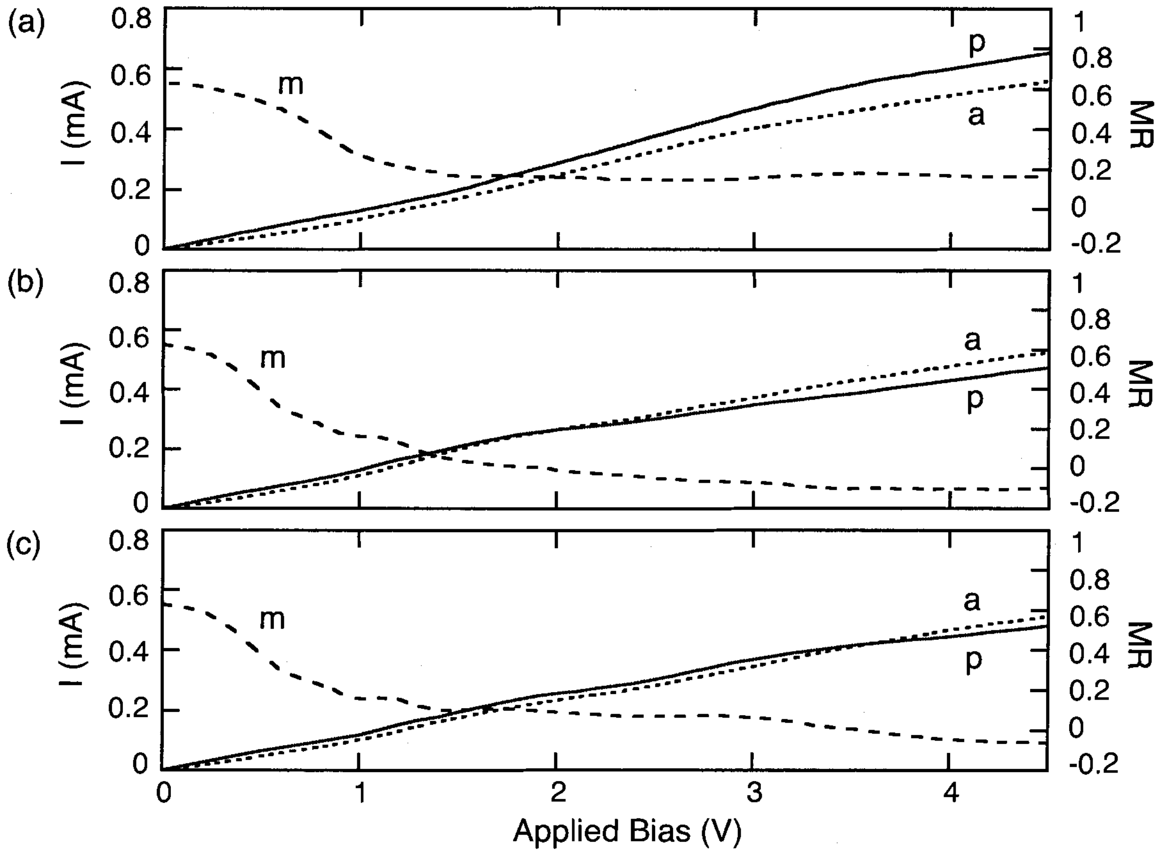

Figure 3.5: The current as a function of bias voltage for the BCC contact geometry in Figure 3.3 for parallel (p) and anti-parallel (a) magnetizations calculated with: (a) $T(E,0)$ approximating $T(E,V)$, (b) The linear voltage drop model, and (c) The abrupt voltage drop model. The MR (m) is also shown. $I(-V) = -I(V)$ due to the system's mirror symmetry.

Figure 3.5(b) and (c) show the results obtained using explicitly bias-dependent transmission probabilities $T(E,V)$ that were calculated for two different models of the potential profile of the nanocontact. In each case the entire voltage drop was assumed to occur across the narrowest constriction in the system, i.e, over the dimer. Thus all atoms (and ideal leads) to the source side of the dimer are assumed to be at a potential $\phi = -\frac{V}{2}$, while atoms and leads to the drain side are at $+\frac{V}{2}$. For the results shown in Figure 3.5(b) the potential is assumed to vary linearly through the region occupied by the dimer [29, 58, 69, 115]. In Figure 3.5(c), for comparison, the potential is assumed to change abruptly from $\phi = \pm\frac{V}{2}$ in the atomic layers adjacent to the dimer to $\phi = 0$ on the two atoms that constitute the dimer itself, a profile analogous to that proposed initially in theoretical work on ballistic semiconductor nanostructures [116] and more recently adopted for modeling certain molecular wires [117, 118]. In each case the electrostatic potential modifies the tight-binding Hamiltonian matrix elements as summarized in Section 2.9.

The applied electrostatic potential breaks the symmetry between the left and right clusters in Figure 3.3. Symmetry breaking often results in weaker transmission probabilities in quantum transport, and this has qualitative implications for the present system: The symmetry breaking as energy levels on the source and drain are shifted apart manifests itself in a somewhat lower transmission and current for parallel magnetization of the contacts (especially at higher bias) in Figure 3.5(b) and (c) than in Figure 3.5(a) where the effect of the applied bias on the transmission is neglected. However the net current for anti-parallel magnetization is much less sensitive to bias-related symmetry effects: As summarized in Figure 3.6, for anti-parallel magnetization of the contacts the applied bias brings the strongly transmitting spin *up* states of the source contact (which according to the maximum in the transmission plot in Figure 3.4(a) are *below* E_F at zero bias) into resonance with similar spin *down* states of the drain contact, and the resulting *up* → *down* transmission increases with increasing bias. However, no such resonant effect occurs for *down* → *up* transmission which decreases with increasing bias. Thus the effect of the applied bias on the *total* transmission for anti-parallel magnetization is relatively small. Because it selectively depresses the current for parallel magnetization of the contacts, the bias-induced symmetry breaking results in a cross-over with increasing bias from positive to negative values of the MR in Figure 3.5(b) and (c), an effect not found in the less realistic model of Figure 3.5(a) where the effect of the bias on the electron transmission probability is neglected. Thus the explicit inclusion of finite bias effects is essential for accurate predictions of the transport characteristics of nanoscale systems with transition metal electrodes that have non-monotonic DOS near the Fermi energy[6].

The bias voltage at which negative MR is predicted to appear ($\sim 2V$ in Figure 3.5(b) and $\sim 3.5V$ in Figure 3.5(c)) depends on the details of the potential profile across the junction where the two electrodes touch: In the linear voltage drop model the bias applied across the

---

[6] For comparison see the relatively monotonic transmission near the Fermi energy predicted for a short gold chain in Ref. [68].

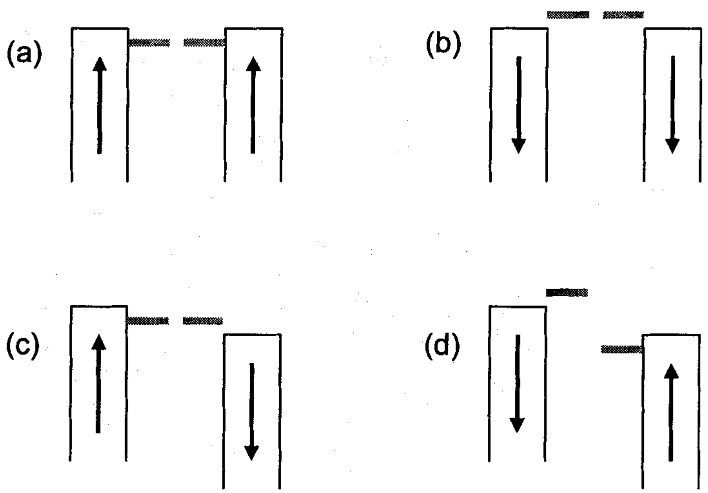

Figure 3.6: Resonant energy level alignment for an Fe QPC under bias. The horizontal line on the left (right) depicts energy states of the source (drain) contact with appropriate spin orientation that contribute most effectively to the transmission according to the largest features in the transmission in Figure 3.4(a). (a) For parallel magnetizations, at zero bias transmitting states on the source and drain are degenerate and located below E_F for spin *up* $\rightarrow$ *up* transmission. The energy levels move apart under bias weakening the transmission in that energy range. (b) Conductive states are higher in energy for the spin *down* orientation. (c) For anti-parallel magnetizations, an applied bias brings the transmitting spin *up* states of the source contact into resonance with spin *down* states of the drain contact enhancing the *up* $\rightarrow$ *down* transmission. (d) The *down* $\rightarrow$ *up* transmission is reduced as energy levels shift further apart under bias.

junction *simultaneously* shifts the energies of similar atomic orbitals on the two tip atoms (as depicted in Figure 3.6), bringing them closer together or further apart, depending on their relative spin orientations and whether the magnetizations of the contacts are parallel or anti-parallel. Thus orbitals of the tip atoms are brought closer to or further from resonance with each other. On the other hand, since in the abrupt voltage drop model the applied bias affects the energies of all of the atomic orbitals of the contacts *except* those of the tip atoms, the corresponding resonant effect of the applied bias in this model is weaker; energies of orbitals within a cluster are shifted with respect to *unshifted* energy levels on the tip atoms. Therefore, the onset of negative MR requires a higher applied bias in the abrupt voltage drop model.

While the *exact* potential profile for a QPC is not known, according to density functional calculations [29, 58] the linear voltage drop model may be a more accurate approximation for all-metal systems than the abrupt voltage drop model. However, the predicted results are qualitatively similar for *both* models of the potential profile (both of which are qualitatively different from the linear response model), demonstrating the robustness of the present method; it is reasonable to expect the results of a fully self-consistent calculation of the potential profile to fall between these two model profiles. Also it is unclear whether a QPC can withstand bias voltages as large as those plotted in Figure 3.5 before the onset of electron migration and other inelastic effects. Nevertheless, the system should enter the regime where bias effects are appreciable well before the onset of such effects and this work is intended to stimulate experiments directed at observing the novel phenomena that are predicted to emerge.

3.5 Spin-Dependent Transport for More General Junction Geometries

3.5.1 Structural Considerations: Bulk and Relaxed Geometries

In the following sections the two (100) Fe BCC $5 \times 5, 4 \times 4, 3 \times 3, 2 \times 2$ and single tip atom clusters are aligned with a *common* (x) axis in the direction of electron propagation and the separation between clusters is varied as occurs in break-junction experiments. In the first of these geometries the two tip atoms are again separated by a bulk nearest-neighbor distance, 2.482Å. This is referred to as the "linear geometry" and is illustrated in Figure 3.7. DFT geometry relaxations [65] on simple model systems involving the pair of 2×2 planes and the two Fe atoms forming the dimer, that have been performed in the course of this work, indicate that the two tip atoms in this geometry are close to their stable positions. Similar relaxations showed that when the clusters are pulled apart, some stretching occurs between the tip atoms and their respective 2×2 layers, but most of the stretching occurs between the two tip atoms. When the tips are far apart representing vacuum tunneling, geometry relaxations show that, with respect to the rest of the cluster, the Fe tip atom sits very near its bulk position. Therefore, it is assumed that as the junction is stretched, all of the stretching

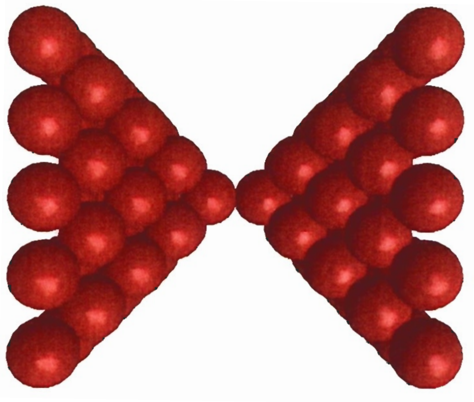

Figure 3.7: Extended molecule for an Fe QPC in a linear contact geometry. Each cluster consists of 55 Fe atoms arranged on bulk BCC Fe crystal lattice positions.

occurs between the two tip atoms, and so the atoms of each tip separately are located on their bulk Fe lattice positions.

3.5.2 Generalizing the Tight-Binding Model

For these more general junction geometries, the Hamiltonian matrix elements $H_C^{L,R}$ of Equation 3.5 between atomic orbitals within each of the two Fe clusters will again be based, as discussed above, on Fe ferromagnetic tight-binding parameters derived from *ab initio* bulk band structure calculations [64]. However a different approach is needed to obtain the non-diagonal Hamiltonian matrix elements, W, that describe tip-to-tip coupling since the atoms involved no longer all fall on sites of a single BCC Fe lattice: The non-diagonal Hamiltonian matrix elements that describe tip-to-tip coupling are estimated using the extended-Hückel method outlined in Section 2.5. However, the values of the matrix elements given in Ref. [64] are not close to the ionization energies of the corresponding atomic orbitals employed by extended-Hückel theory but are defined up to an arbitrary additive constant. It is necessary to choose the value of this constant with care in order to obtain realistic results from Equation (2.12). Its value is chosen so that when the two tips are positioned in the BCC geometry studied in Section 3.4, the model (including the tip-to-tip coupling matrix elements, W, obtained using Equation (2.12)) reproduces the $up \rightarrow up$ transmission near the Fermi energy (Figure 3.4(a)) obtained using only the bulk parameters from Ref. [64]. The value of the shift that is applied to the bulk electronic parameters is $C = -13.53eV$. Since the atomic orbital basis is non-orthogonal, the energy shift is applied with the methodology outlined in Appendix A. The same tip-to-tip coupling parameters are used for all spin configurations. This is consistent with the fact that bulk *up-up* coupling parameters are very similar to *down-down* coupling parameters [64]. The transmission away from the Fermi energy for the spin *up* configuration with this parameterization is in good qualitative agreement with that found utilizing the bulk parameters for the tip-tip coupling. The spin *down* and anti-parallel configurations also yield transmission in qualitative agreement near and away from the Fermi energy.

Thus the overlaps $S_{i,j}$ in Equation 2.13 between Slater-type orbitals provide the *distance and orientation-dependence* of the tip-to-tip Hamiltonian matrix elements, W, required for the more general junction geometries (as in extended-Hückel theory). However, the Hamiltonian matrix elements are normalized so as to yield transport results consistent with those obtained from a Hamiltonian matrix derived from *ab initio* calculations.

3.5.3 SDT in Fe Nanocontacts Bridged by Fe Atoms in a Linear Geometry

Results for spin transport for an Fe QPC in the linear geometry (Figure 3.7) with tip atoms separated by a bulk nearest-neighbor distance (2.482Å) are shown in Figure 3.8. The spin $up \rightarrow up$ transmission for parallel magnetizations shown in Figure 3.8(a) shows a similar plateau above E_F to that for the BCC geometry (Figure 3.4(a)). This similarity is due to the dominance of the non-directional s-orbitals in both cases. Below the Fermi energy, the transmissions exhibit significant differences, due to the importance of the very directional d-orbitals in that energy range. For the two different geometries, spin $down \rightarrow down$ (Figure 3.8(a)) and $up \rightarrow down$ (Figure 3.8(b)) transmissions are similar in a broad sense, such as overall magnitude, but display many differences on a finer scale due to the importance of d-orbitals in those transmissions.

As shown in Figure 3.8(c) the current as calculated from the voltage-dependent transmission in the linear voltage drop model is slightly weaker for the linear geometry than for the BCC geometry. The weaker current can be attributed to the lack of second nearest-neighbor coupling between the two contacts in the linear geometry. A larger MR is pre-

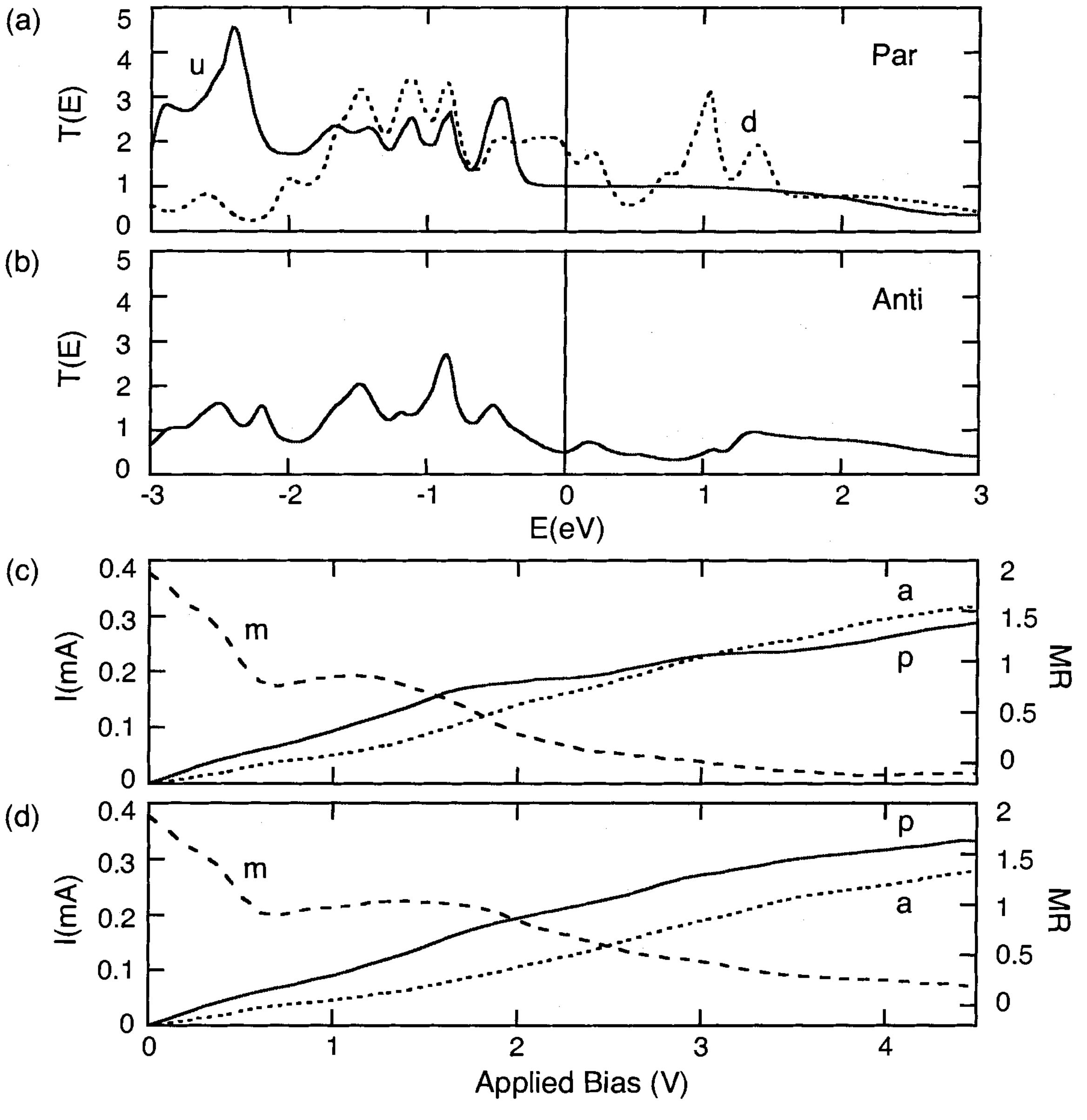

Figure 3.8: Spin-dependent transport for an Fe QPC in the linear geometry shown in Figure 3.7. (a) The transmission probabilities at zero bias for spin *up* → *up* (u) and *down* → *down* (d) configurations for parallel magnetizations. The Fermi energy is located at $0eV$. (b) Spin *up* → *down* transmission for anti-parallel magnetization. Currents for parallel (p) and anti-parallel (a) magnetizations and MR (m) calculated with the linear voltage drop model and the abrupt voltage drop model are shown in (c) and (d), respectively.

dicted than for the BCC geometry and a negative MR is again predicted, but this time it manifests near an applied bias of $3V$. As was discussed for the BCC geometry, in the linear voltage drop model the applied bias *simultaneously* moves the atomic orbitals of the tip atoms closer or further apart in energy. Thus the linear voltage drop model provides a relatively strong mechanism for those energy levels to move closer to or further from resonance with each other. However, in the present case of the linear geometry, there is no second neighbor coupling between a tip atom and atoms of the opposite contact and so the resonant effect is weaker than in the previous case of the BCC geometry. The potential profile with abrupt voltage drops is also less conducive to negative MR here (as in the BCC geometry) thus a negative MR does not occur within the voltage range in Figure 3.8(d). Again, all of these results are also reasonably robust to the addition of a 6×6 atom layer to each of the clusters.

It should be noted that the classical Julliére estimate (Eqn. (3.4)) employing commonly accepted measured spin polarizations (P=.45) [91] yields a MR of 51% for Fe MTJs, in reasonable agreement with the predicted MR for an Fe QPC in the BCC geometry at low bias in Figure 3.5. However, the Julliére model does not account for the strong bias dependence of the MR, nor the inversion of MR with increasing bias. More importantly, the differences in the magnitude of the magnetoresistance for Fe QPCs arranged in the BCC and linear geometries serves to illustrate the major inadequacy of the Julliére model for spin-dependent transport in nanoscale systems: While it is clear that both bulk and surface densities of states influence transmission probabilities, the Julliére estimate based *entirely* on properties of isolated electrodes does not include directional effects that are responsible for the differences between Figures 3.5(b,c) and Figures 3.8(c,d) that emerge in the full quantum mechanical calculation. Such differences may be regarded as the analogue of interface effects in the present class of nanoscale systems. The inadequacy of the Julliére formula is further illustrated in the following section where the separation between tip atoms will be allowed to vary, for which the simplest Julliére model predicts *no* change in MR.

3.5.4 Dependence of Spin Transport on the Separation Between Tip Atoms and Dangling Bond Formation

Figure 3.9(a,b) shows the calculated dependence of the magnetoresistance and spin injection factor (as defined by Eqns. (3.1) and (3.2), respectively) on the separation between the two tip atoms as the junction is stretched for two values (0.5 and 1.0V) of the bias voltage, for the linear voltage drop model.

As the separation between tip atoms is increased, the MR (Figure 3.9(a)) initially decreases rapidly then increases to a local maximum at tip separations near 3.5 and 4Å then resumes its decrease turning weakly negative and, for 0.5V bias, increases again at large separations. The spin injection factor for parallel magnetization of the contacts (Figure 3.9(b)) is negative at small separations, i.e., the spin *down* (minority spin) current predominates, and rises initially with increasing separation almost to zero near 3Å. It then passes through a minimum near 3.5 and 4Å (where the MR shows a maximum) before resuming its rise and becoming positive at large separations. The local maxima in the MR and minima in the spin injection factor near 3.5 and 4Å are due to a pronounced resonance in the dominant *down* → *down* transmission that appears near the Fermi energy for parallel magnetization of the contacts at such separations. This transmission resonance persists when a 6×6 Fe layer is added to each nanocontact, thus it does not appear to be a dimensional resonance due to the finite size of the Fe clusters[7].

By examining the contributions of the individual electronic eigenstates of the Hamiltonian of the coupled Fe clusters to the *down* → *down* transmission (through the Green's function G_0 in the Lippmann-Schwinger Equation (2.15)) the particular eigenstate that is responsible for this transmission resonance was identified: Mulliken analysis revealed that for tip separations corresponding to the appearance of the *down* → *down* transmission resonance, a significant portion of this eigenstate resides on the tip atom of the drain contact[8] and has $d(x^2-y^2)$ orbital symmetry there; the $d(x^2-y^2)$ orbital has a lobe oriented along the x-axis towards the tip atom on the other cluster. Since the $d(x^2-y^2)$ orbital is involved

---

[7] Similar trends to those displayed in Figure 3.9 were predicted also for different choices of tip-tip matrix elements, W.

[8] A similar eigenstate with enhanced weight on the tip atom of the source contact is also found but under most conditions its energy is outside of the range between the source and drain electrochemical potentials so that it does not contribute significantly to the current.

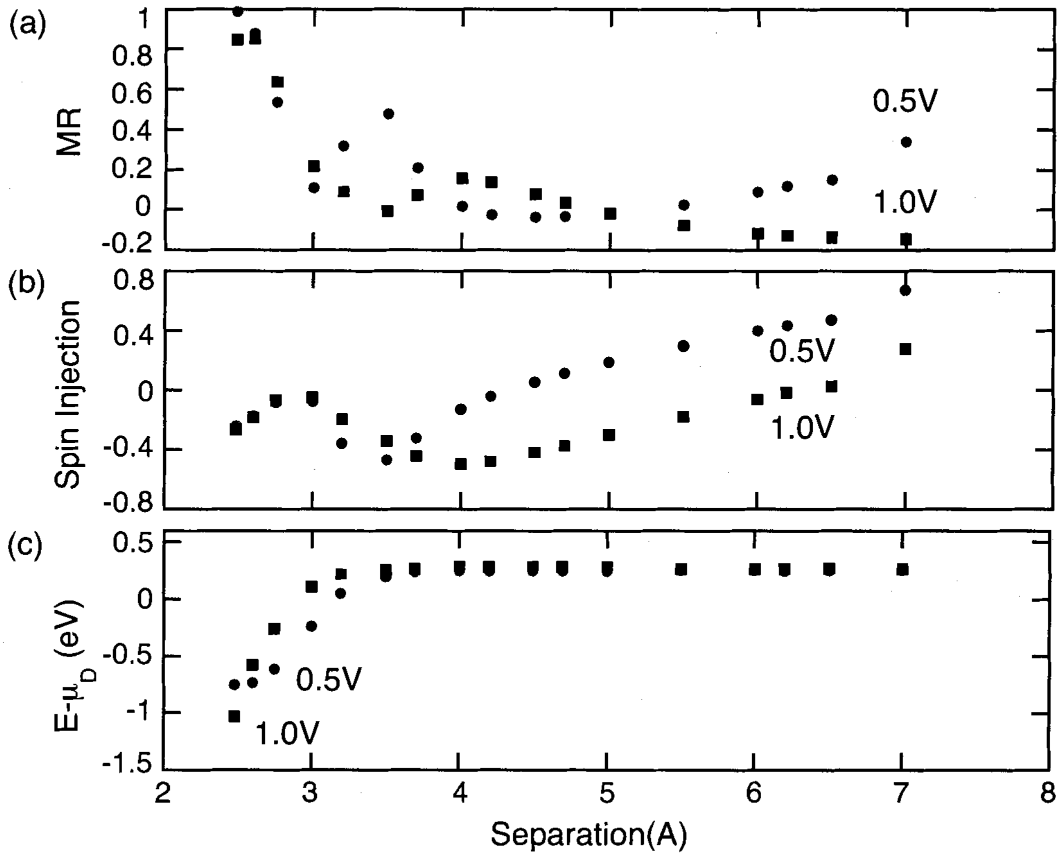

Figure 3.9: Spin-dependent transport in the linear tip geometry vs. separation of the tip atoms. (a) MR as a function of tip separation for applied biases of 0.5*V* (circles) and 1.0*V* (squares). (b) The spin injection of the current for the same separations in (a). (c) The energy eigenvalue associated with the spin *down* dangling bond state relative to the chemical potential of the drain electrode (0*eV*) as a function of tip separation.

in tip-to-tip bonding and the amplitude of the eigenstate of interest on the tip atom increases as the tip separation is increased, the appearance of this eigenstate state is attributed to bond-breaking between the tip atoms and associated formation of a dangling bond.

The energy E of the dangling bond eigenstate relative to the electrochemical potential of the drain is plotted in Figure 3.9(c) as a function of tip separation for the two values of applied bias considered in Fig. 3.9(a,b). The dangling bond state is the dominant feature in the Mulliken spectrum of the tip atom within a broad window about the Fermi energy and this criterion is used to identify the state for the different values of the tip separation and applied bias. At zero temperature, only states within the limits of integration corresponding to the applied bias contribute to the predicted current (see Eq. (2.1)). These limits are determined by the electrochemical potentials of the source ($0.5eV$ and $1.0eV$ in Figure 3.9(c) for the two values of applied bias) and the drain ($0eV$). As shown in the figure, as the tip separation is increased, the energy of the dangling bond state shifts into the window of integration, above the electrochemical potential of the drain and therefore begins to contribute to the current. (Note that this happens at separations close to those where the MR in Fig. 3.9(a) first begins to rise signaling the onset of the transport resonance). Simultaneously, the Mulliken weight of the state located on the drain tip increases (as the separation is increased) to a value of about 10%, a sizeable portion of the total probability distribution of the eigenstate given that a total of 110 atoms make up the Fe clusters in the present model. Therefore, as the separation is increased from its smallest distance of 2.482Å, the initial decrease in MR is attributed to the stretching of the bond between the two tip atoms. The following increase to the local maximum in MR is attributed to the formation of a dangling bond as the tips are further pulled apart, leading to the resonant feature in the *down* ⟶ *down* transmission. Once the dangling bond has been formed, its energy and Mulliken weight are roughly constant, and the MR resumes its decrease with increasing separation.

As was discussed in the previous sections, *s*, *p* and *d*-electrons all play a significant role in transport in this system for small tip separations. However their contributions decay differently as the tip separation is increased and the tunneling regime is entered. Since the valence *d*-electrons have a lower site energy than the other electrons ($E_d < E_s, E_p$) [64], they decay more rapidly resulting in a less significant contribution from *d*-electrons to transport as the tip separation is increased.

For an applied bias of $0.5V$ and near a tip separation of about 4.5Å, the contribution to tunneling from *d*-electrons is roughly equal to that of *s*-electrons. Here $T_{up \rightarrow up}$ (mostly due to *s*-electrons) and $T_{down \rightarrow down}$ (mostly due to *d*-electrons) are roughly equal and the spin injection factor (Fig. 3.9(b)) is roughly zero, defining a cross-over regime. This can be viewed as the cross-over from ballistic transmission to tunneling-like transport. At the cross-over, transmission from spin *up* (mostly *s* and *p*) to spin *down* (mostly *d*) for anti-parallel magnetization of the contacts is roughly the same as that for the parallel spin configurations, and the resulting MR (Fig. 3.9(a), $0.5V$) is very small, or even slightly negative. Since this small negative magnetoresistance appears at a relatively small applied bias, it should be accessible experimentally in these systems.

At larger separations, beyond the cross-over regime, the current is dominated by the transport of s and p-electrons and $T_{up \to up}$ makes the largest contribution. Therefore the spin injection factor (Fig. 3.9(b)) is positive, and growing. Since transmission involving *down* (mostly d) electrons is rapidly decreasing, $T_{down \to down}$ and $T_{up \to down}$ are small (due to band mismatch the anti-parallel transmission in general is smaller than the decreasing *down* $\to$ *down* transmission) and, as can be seen in Fig.3.9(a) in the $0.5V$ case, the MR also begins to slowly grow. At higher biases (for example at $1.0V$ bias in Fig.3.9(a) and (b)) more energy levels are sampled, increasing the importance of the d-states to transport and the cross-over doesn't occur until larger separations. Therefore, this model predicts that when d-states are important, the current will be dominated by minority electrons, and when d-states are negligible, current due to majority electrons will dominate. This is quite analogous to the predictions made by Mathon on periodic systems involving cobalt and tunneling gaps of varying widths, where the fast decrease in d-electron transport accounts for a rapid reversal in sign of the spin injection [92, 97].

The strong dependence of the MR and spin injection (which provides an indication of the spin polarization P) on both separation and bias serves as further illustration of the inadequacy of the classical Julliére theory for predicting SDT properties with commonly accepted (measured) spin polarization values in which both considerations are neglected.

3.5.5 Vacuum Tunneling Between Fe Nanocontacts

When the separation between tip atoms is very large (vacuum tunneling), the d-electron states have decayed across the gap between the contacts and do not significantly contribute to the transmission. In this situation all Hamiltonian matrix elements coupling the tip atoms, except those involving s and p_x-orbitals, are negligible. Figure 3.10(a,b) shows the calculated transmissions for Fe nanocontacts in the linear geometry with a tip atom separation of 7Å at zero bias. Similar weak transmission resonances to those labeled u and d in Figure 3.10(a) will be significant for the prediction of *spin current rectification* in Chapter 6.

Figure 3.10(c) shows the $I-V$ characteristics calculated using the linear voltage drop model for $T(E,V)$. The current increases with bias ($\sim$ linearly at low bias), resembling

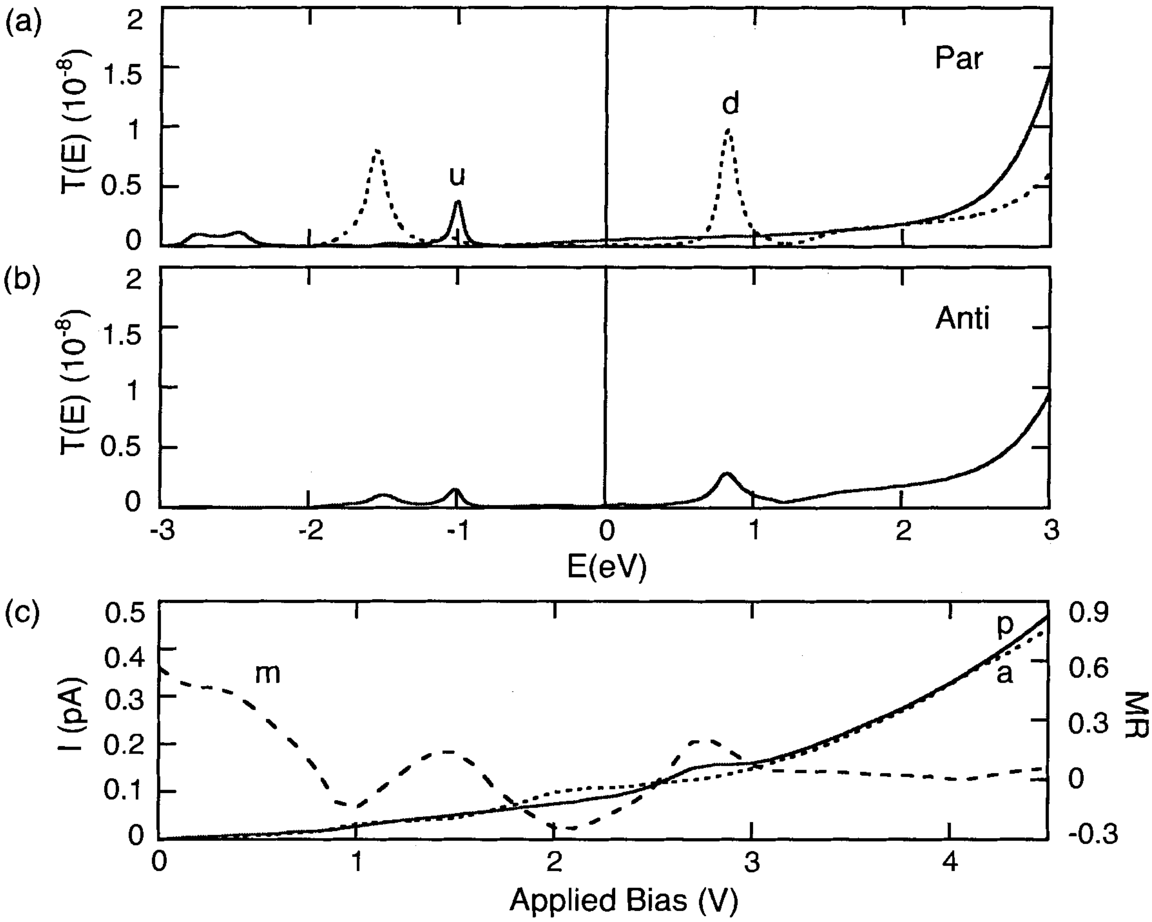

Figure 3.10: Spin-dependent transport for Fe nanocontacts with 7Å tip separation representative of the vacuum tunneling regime. Transmission probabilities for parallel and anti-parallel magnetizations are shown in (a) and (b), respectively. The Fermi energy is located at $0eV$. (c) Current for parallel (p) and anti-parallel (a) magnetizations and MR (m) calculated with the linear voltage drop model.

the accepted behavior of tunneling through vacuum. At the application of about $2V$, the *up* → *down* transmission becomes the strongest scattering channel due to a similar resonant enhancement to that depicted in Figure 3.6 between the transmitting states labeled *u* and *d* in Figure 3.10(a), so the anti-parallel current becomes stronger than the parallel current. This results in a relatively strong, negative MR, although the *down* → *down* transmission regains its dominance and positive MR returns at higher bias. Thus the shifting of different transmission maxima again results in non-monotonic behavior of the MR and negative MR for some values of the applied bias. However, there is no sustained MR reversal such as is predicted when d-electron states contribute directly to transport.

3.6 Conclusions

In this chapter, the application of the microscopic quantum theory of transport developed in Chapter 2 to iron nanoscale junctions bridged by Fe quantum point contacts has elucidated many of the systematics and complexities of spin-dependent transport in nanoscale systems. Ferromagnetic tight-binding parameters (that were shown to provide a satisfactory description of surface and nanoscale geometries as well as bulk properties) were applied to study ballistic transport between a pair of Fe contacts connected by two Fe atoms in a nearest-neighbor geometry. It was predicted that the magnetoresistance of this system should switch sign from positive to negative with increasing bias voltage, when the effects of finite bias are included explicitly, illustrating the importance of such considerations for electron transport in nanoscale systems with transition metal contacts.

The tight-binding model was extended to study spin-dependent transport for more general tip geometries and predictions of the magnetoresistance and spin injection as a function of separation between Fe QPCs were presented from nearest-neighbor distances to the vacuum tunneling regime. Characteristic trends emerging in those transport predictions as the separation is varied were associated with decay rates of different orbitals and with the breaking of bonds and associated dangling bond formation resulting in spin-dependent transmission resonances.

Spin-dependent transport properties of the QPC junction are influenced by bulk and surface densities of states for the ferromagnetic electrodes, but a systematic, physical interpretation of the predicted phenomena required a more complete physical picture than is provided by density of states considerations alone. Thus the classical Julliére formula for estimating the magnetoresistance from experimental spin polarizations (or DOS considerations) of the electrodes was found inadequate as it neglects the influence of interface effects that are crucial to transport in nanoscale systems. A Julliére model expressed in terms of *effective* spin polarizations that take into consideration the effect of interfaces will be reconciled with the quantum transport calculation at the end of Chapter 4.

Chapter 4

Molecular Spintronics: Spin-dependent Transport in Molecular Wires

4.1 Introduction

Molecular wires with ferromagnetic electrodes have been predicted to produce significant magnetoresistance effects [38, 39, 40, 41, 42, 43, 44] due to the significant energy splittings between spin up and spin down states in the magnetic metal contacts and the weak spin-orbit interaction (negligible spin flipping) in organic molecules. Experimental reports on $100nm$ organic molecular films with magnetic electrodes [45, 46] have confirmed that a molecular bridge is capable of sustaining significant spin polarization leading to magnetoresistance, proving that individual or groups of organic molecules may potentially be used for building ultra-small spintronic devices. Thus novel *molecular spintronic* systems are just beginning to be explored while being amongst the smallest possible nanoscale spintronic devices.

More recently, an experiment was reported in which electrons transmitted through octanethiolate (OT) molecular self-assembled monolayers (SAMs) between nickel contacts [47] retained their spin polarization, yielding an observed magnetoresistance of roughly 12%. While appreciable, the observed magnetoresistance was markedly lower than the 21% predicted by the Julliére formula (Eqn. (3.2)) together with the commonly accepted spin polarizations for Ni electrodes ($P = .31$) [91]. Bias-dependent and negative magnetoresistance were also reported leading the authors [47] to speculate that these phenomena may be due to the presence of impurities within the molecular film. However, similar effects were predicted in the previous chapter of this thesis also for *ideal* iron quantum point contacts. The corresponding phenomena for spin-dependent transport in ideal molecular wires will now be investigated theoretically.

Molecular wires with iron electrodes, systems that until now have received little experimental or theoretical attention, will be considered first, permitting the methodology and physical insight developed for Fe nanocontacts in Chapter 3 to be applied to the present class of molecular spintronic systems. Two very different Fe-molecular junctions will be explored theoretically: A conducting (conjugated) benzene-dithiolate (BDT) molecule and an insulating octane-dithiolate (ODT) molecule bridging ferromagnetic Fe nanocontacts [43]. The atomic structure of the Fe-molecular junctions is considered in detail in Section 4.2.1 so that appropriate atomistic models of the extended molecules may be constructed. Refinements to the hybrid tight-binding model introduced in Section 2.6 for molecular wires with transition metal electrodes are then developed in Section 4.2.2 so that the model appropriately describes also the electronic structure of conjugated BDT molecules. The transport formalism developed in Chapter 2 is then employed to predict strong bias dependence of the magnetoresistance, and also the magnetoresistance to become negative with increasing applied bias for the Fe-BDT molecular wire in Section 4.3.1. Thus these calculations predict bias-dependent and negative magnetoresistance to be *intrinsic* properties of at least some molecular junctions (i.e., *not* dependent on the presence of impurities). Quite similar phenomena will be predicted also for insulating Fe-ODT molecular wires in Section 4.3.2. The physical origin of these phenomena will be identified as resonant transmission mediated by states that develop at the Fe metal-molecule interface due to the strong chemical bonding between molecular sulfur orbitals and Fe d-electron orbitals.

Once the nature of these phenomena has been elucidated in molecular spintronic devices with Fe contacts, spin-dependent transport will be investigated theoretically for molecular wires with nickel electrodes in Section 4.4. The calculation will reveal that *ideal* Ni-OT molecular tunnel junctions should display bias-dependent and negative MR similar to that observed experimentally in Ref. [47]. A MR maximum of roughly 12% (markedly lower than the Julliére estimate) is predicted, suggesting that the maximal magnetoresistance for the device may have in fact been obtained experimentally [47] (i.e., the magnetoresistance may *not* have been limited by impurities).

An analytic methodology for extracting *effective* spin polarizations of each contact under bias voltage from the transport calculation will then be developed and applied for the Ni-OT system in Section 4.5. When used together with the Julliére formula (Eqn. (3.2)), the effective spin polarizations (that are strongly dependent on the metal-molecule interface and on the applied bias) reproduce the predicted bias-dependent magnetoresistance. This result suggests that with the new definition of effective spin polarizations introduced here, the simple Julliére formula may be reconciled with the results of more sophisticated quantum spin transport calculations.

4.2 Modelling the Geometry and Electronic Structure of BDT Molecular Wires

An organic molecule of current experimental interest for molecular electronics is 1,4 benzene-dithiol. As depicted in Figure 4.1, the molecule consists of a benzene ring with the hydrogen atoms at ring positions 1 and 4 substituted by sulfurs. A hydrogen atom covalently bonds to each of the sulfur atoms and the molecule is charge neutral. The carbon p-orbitals that are not involved in the σ-bond framework of the planar benzene ring form molecular π-orbitals that are de-localized on the ring. Thus the electronic states on the ring of benzene-dithiol (that are close in energy to metal contact Fermi energies) are de-localized and thought to be conducive to electron transport; benzene-dithiol is expected to behave as a conductor, unlike simpler alkane-thiol molecules which are insulators. Both types of molecules possess relatively few atoms and simple regular geometries, and thus are optimal for modeling.

4.2.1 Structural Considerations: Atomic Details of the Metal-Molecule Interface

1,4 benzene-dithiol (and other thiolated molecules) may chemisorb between metal contacts to form a molecular wire via the following chemical pathway: In close proximity with a metal, benzene-dithiol loses the hydrogen ion bonded to each of the sulfurs and becomes 1,4 benzene-dithiolate (denoted BDT in this thesis). The BDT molecule has charge $-2e$ as the sulfurs acquire the electrons from the shed hydrogen ions that each react with the nearby

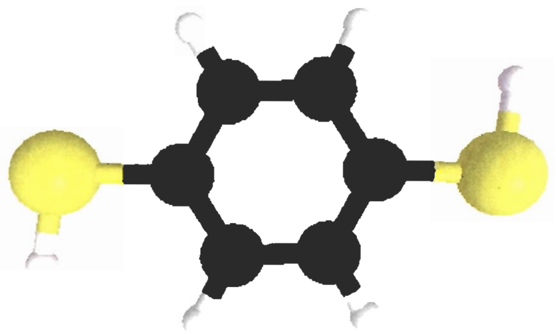

Figure 4.1: Ball-and-stick model for a geometry optimized [65], charge neutral 1,4 benzene-dithiol molecule. Large yellow balls indicate sulfur atoms; medium black, carbon atoms; small white, hydrogen atoms.

metal contacts by capturing a readily-removed valence electron. BDT then covalently bonds via chemisorption of the sulfurs (often referred to as 'anchoring groups' or 'alligator clips') to the contacts [119]. Thus BDT may self-assemble with appropriately positioned metal electrodes to form a molecular wire.

Molecular wire systems have been realized with an array of experimental techniques including STM [2, 3, 5, 6, 8, 19], mechanically controlled break junction [4, 18], cross-bar [12] and evaporated top metal contact assemblies [7, 13]. However, these experimental systems are very difficult to characterize on the atomic scale: Even for such systems based on gold electrodes (which have received tremendous experimental and theoretical attention) the atomic geometries of the metal-molecule interfaces remain unclear and may vary for different experimental set-ups. As an emerging area of molecular electronics, even *less* is known about the metal-molecule interface for molecular wires with transition metal contacts. However, as transport experiments have yet to be performed on the majority of the transition metal-molecular wire systems considered in this thesis, the predictions presented here are intended to stimulate related experiments that may be achieved with an assortment of techniques. Thus, while atomic details of the metal-molecule interface are required at the outset of the transport calculation that is based on an atomic description of molecular wires, physically reasonable *estimates* for these parameters are sufficient for the present purpose. In this fashion, qualitative trends may be extracted from the resulting electron transport predictions. Trends that are robust to variations in the model parameters should be directly observable in a range of experimental systems for which control of the atomic scale geometries is beyond the present state-of-the-art[1]. Moreover, while a single molecule is considered for the conducting bridge throughout this thesis, the mechanisms responsible for transport in molecular wires with transition metal contacts that are identified in this thesis should be applicable even to systems that may involve overlapping molecules [4, 30] or SAMs [7, 12, 13]. A systematic study of the effects of the atomic structure of the metal-molecule interface on electronic transport will be presented in Chapter 5.

Fe (100) oriented clusters of the type considered in Chapter 3 are assumed for the Fe-molecular wires studied here; reconstructions of the (100) Fe surface that may occur upon thiol adsorption are not considered. Alkane-thiols have been shown to adsorb on Fe (100) surfaces [121], however data for the preferred atomic adsorption site (particularly for BDT) on Fe is not presently available. Thus the molecular sulfur atoms are assumed to bond over Fe surface hollow sites, similar to the positioning of the Fe tip atoms in the previous chapter. For comparison, 'top-site' adsorption (the molecule bonds directly over a single tip atom that protrudes from the electrode surface) is also investigated. Such a contact geometry may be more realistic for experiments that contact a single molecule by retracting an STM tip [19]; due to the strength of the metal-S bond, a metal atom may be pulled to the bottom of the tip during the retraction. Additional adsorption sites will be investigated in Chapter 5 for (111) transition metal surfaces.

Upon adsorption on the (100) Fe electrode surfaces, the geometries of the molecules are assumed not to change. This assumption is supported by the only nominal atomic rearrangement of singly ionized 1,4 benzene-monothiol-monothiolate (denoted BDT') predicted by DFT geometry relaxations [65] carried out in the course of the present research for adsorption on a four atom Au (100) surface (denoted Au4) and on a two atom Fe (110) surface (denoted Fe2). The BDT S-C bond is assumed perpendicular to the Fe surface. Negligible tilt angles were obtained for geometry relaxations of BDT' on Au4 and Fe2 [65].

The final parameter required for an atomic specification of the Fe-molecular wire is the Fe-S bond length. Measured perpendicularly from the sulfur atom to the plane of the surface of Fe atoms, the Fe-S distance is estimated here to be 2.0Å with DFT geometry relaxations [65] of BDT' adsorbed on Fe2 and also of simple SH molecules on Fe4. Similar distances were also obtained for geometry relaxations of BDT' on Au4 [65], in agreement

---

[1] A *statistical* approach to theoretically treating such geometrical variations was reported in Ref. [120].

with previous theoretical results for thiols on Au (100) surfaces [122].

4.2.2 Electronic Considerations: Modification of Extended-Hückel

The electronic structure of the Fe-BDT molecular wire is modeled with the hybrid tight-binding methodology developed in Section 2.6 that is based on a combination of an appropriately modified extended-Hückel theory and tight-binding parameters obtained from fitting known band structures. Extended-Hückel has been used successfully to explain the experimental current-voltage characteristics of molecular nanowires connecting non-magnetic metal electrodes [5, 12, 30]. It includes electronic states for valence orbitals for each of the atoms of benzene-dithiol: The H atoms are each modeled with a single $1s$ orbital, C with a $2s$ and three $2p$ (p_x, p_y, p_z) orbitals, and S with a $3s$ and three $3p$ orbitals. Atomic orbitals couple together (through Eqn. (2.12)) to produce single-electron molecular orbitals.

In the ground state, the single-electron molecular orbitals of benzene-dithiol fill with two electrons per state (one per spin) up to the Highest Occupied Molecular Orbital (HOMO). The next highest orbital is the Lowest Unoccupied Molecular Orbital (LUMO). In a BDT-molecular wire, the electrode Fermi level is thought to lie between the HOMO and LUMO (of benzene-dithiolate). Thus transmission at moderate bias is expected to be mediated by those orbitals. Thus two electronic properties of primary importance for modeling are the separation between the Fermi level and molecular HOMO (ΔE introduced in Section 2.6 and discussed below) and the HOMO-LUMO gap.

For benzene-dithiol, extended-Hückel theory yields a HOMO-LUMO gap of approximately $2.2eV$, significantly smaller than that estimated from experimental absorption spectra of benzene-dithiol in solution [123]. Based on *time-dependent* density functional theory (TDDFT)[2] [65] a theoretical estimate for the HOMO-LUMO gap of $4.5eV$ was obtained for benzene-dithiol, in line with experimental values [123]; as the HOMO of benzene-dithiol is completely filled, the energy difference between the ground state and first excited state corresponds to an electron transition between the HOMO and LUMO. In the spirit of extended-Hückel theory this calculated excitation energy is interpreted as the energy difference between two effective single-particle electronic states, i.e., as a measure of the

---

[2] Analogous to total energy ground state electronic properties within DFT, TDDFT provides reliable information for *excited* molecular states.

HOMO-LUMO gap.

This deficiency of the extended-Hückel method is corrected here by replacing the phenomenological parameter K in Equation (2.12), with

$$K_{i,j} = \begin{cases} 2.29 & i,j \in \{C_{2p}\} \\ 1.75 & otherwise \end{cases} \tag{4.1}$$

where $K_{i,j}$ are fitting parameters so that the modified extended-Hückel model obtained in this way yields the correct HOMO-LUMO gap. I.e., when both atomic orbitals in Eqn. (2.12) are carbon p-orbitals, the phenomenological parameter K is increased. Similar orbital-dependence for K has been included successfully to improve extended-Hückel theory so that it predicts the correct bandgap of silicon [31]. The energy eigenvalues and eigenstates of the benzene-dithiol molecule in Figure 4.1 calculated within this modified extended-Hückel theory are displayed in Figure 4.2. Mulliken analysis was used to determine the sulfur and carbon content of each eigenstate. The estimated location of the iron electrode Fermi energy (as predicted with the methodology developed in Section 2.6) is shown for reference. Having mainly carbon π-orbital content, the primary effect of Eqn. (4.1) is a rigid shift upwards in energy of the LUMO and LUMO+1[3] (as both TDDFT and experiment indicate is appropriate).

The spin-dependent tight-binding model introduced in Section 2.6 and examined in Section 3.3 is applied to describe the electronic structure of the (100) Fe contacts. As discussed in the previous chapters, the model incorporates *both* the bulk and surface magnetic properties of Fe which together influence the spin-dependent transport through a nanoscale junction of bulk Fe leads bridged with molecules. Spin flip processes are not considered, consistent with weak spin-orbit interaction in organic molecules and the high degree of spin polarization retained in spin-dependent transport experiments on molecular junctions [45, 46, 47]. The molecular electronic parameters, H^M, and Hamiltonian matrix elements, $W_M^{L,R}$, coupling the Fe electrodes and the molecule are described with the modified extended-Hückel formalism developed above. Thus a spin-independent parameterization is used to model the Fe-molecule coupling consistent with the fact that off-diagonal spin

---

[3] The parameterization has also a marginal effect on the composition of the HOMO and HOMO-1, reducing their carbon content by approximately 10% (compared with un-modified extended-Hückel theory) and correspondingly increasing the sulfur content. Nevertheless, the HOMO remains de-localized: It is nearly perfectly transmitting on resonance as demonstrated in the following section.

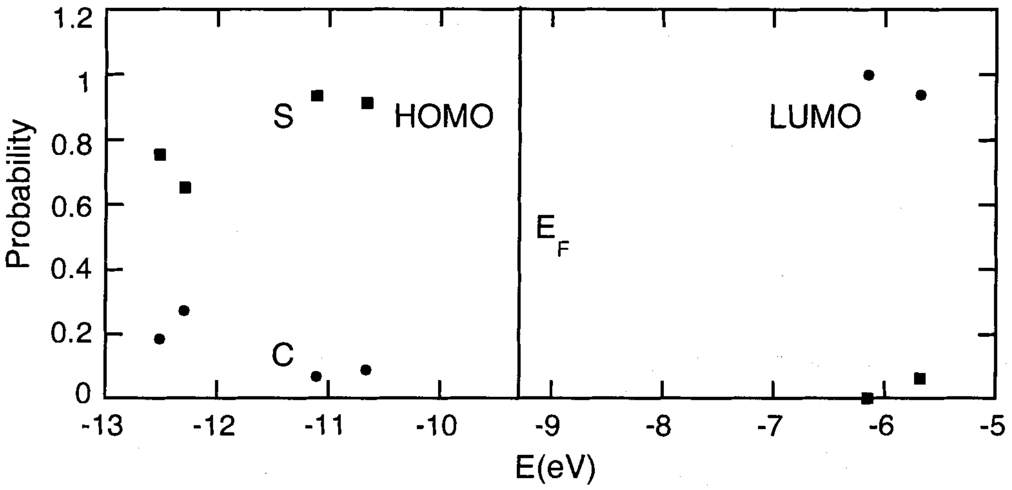

Figure 4.2: Energy eigenvalue spectrum of isolated 1,4 benzene-dithiol resolved into Mulliken probabilities for sulfur (squares) and carbon (circles). The hydrogen content is not shown. The Fe Fermi energy location, $E_F = -9.3eV$, as estimated in the following section, is shown for reference by the vertical line. A similar spectrum is predicted for the ionized BDT molecule.

up parameters in Ref. [64] are not very different from spin *down* parameters. Based on the methodology developed in Section 2.6, the separation between the Fe electrode Fermi energy and the HOMO of BDT is estimated to be $\Delta E = 1.36eV$.

Finite bias voltage effects are included explicitly through the heuristic methodology outlined in Section 2.9. The majority of the applied bias is assumed to drop over the metal-molecule interface [29, 58, 118]; one-third of the applied bias is assumed to drop at each interface and the remaining one-third linearly over the length the molecule. This model profile mimics the effects of charging and screening in an averaged sense[4]. Nearly identical current-voltage characteristics emerge if the details of the model potential profile are varied. Thus, as will be investigated in greater detail in Chapter 5, these details are not crucial to the predictions presented here.

---

[4] It has been shown by comparison with the results of *ab initio* calculations [58] (that include the electronic correlation energies of molecular wires and their electric field dependence in a mean field approximation) that the effects of screening and capacitive charging of the electrodes on transport in simple molecular wires can be modeled accurately by employing appropriate phenomenological potential profiles between the metal contacts.

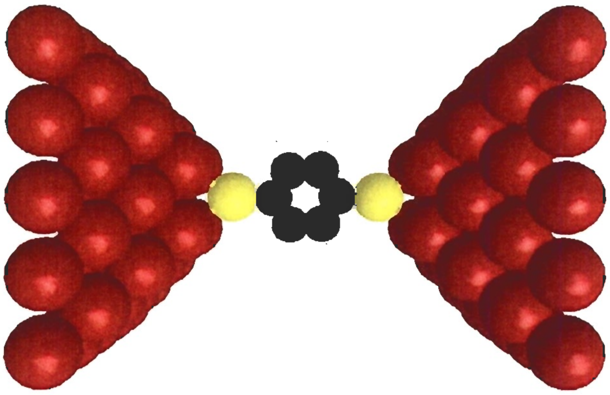

Figure 4.3: Extended molecule for a Fe-BDT molecular wire. Each metal cluster consists of 54 Fe atoms that coincide with sites of a (100) BCC Fe crystal lattice.

4.3 Spin-dependent Transport in Molecular Wires with Fe Contacts

4.3.1 Conducting Fe-Molecular Wires: BDT

The Fe-BDT extended molecule incorporating the estimates obtained in the preceding section for the geometrical parameters, is shown in Figure 4.3. Each ferromagnetic Fe cluster is built from 54 Fe atoms arranged in the bulk geometry of (100) Fe, which in Chapter 3 was shown to be large enough to represent real macroscopic leads that come together to contact a molecule, as in experimental realizations of molecular wires. Arrays of one-dimensional source and drain leads are coupled to this structure (as described in Section 2.7) to perform the transport calculation. The atomic structure of the molecular wire is assumed rigid under the application of bias voltage.

Figures 4.4(a,b) show the calculated transmission probabilities at zero bias for the Fe-BDT molecular junction in Fig. 4.3. The spin *up* $\longrightarrow$ *up* (u) and *down* $\longrightarrow$ *down* (d) transmissions (Figure 4.4(a)) are for parallel magnetization of the two contacts; *up* $\longrightarrow$ *down* transmission (Figure 4.4(b)) is for anti-parallel magnetization. Quite similar results for the transmissions and currents are obtained if the 5×5 outer Fe layer is deleted from each of the clusters indicating that the model clusters and ideal leads adequately represent real

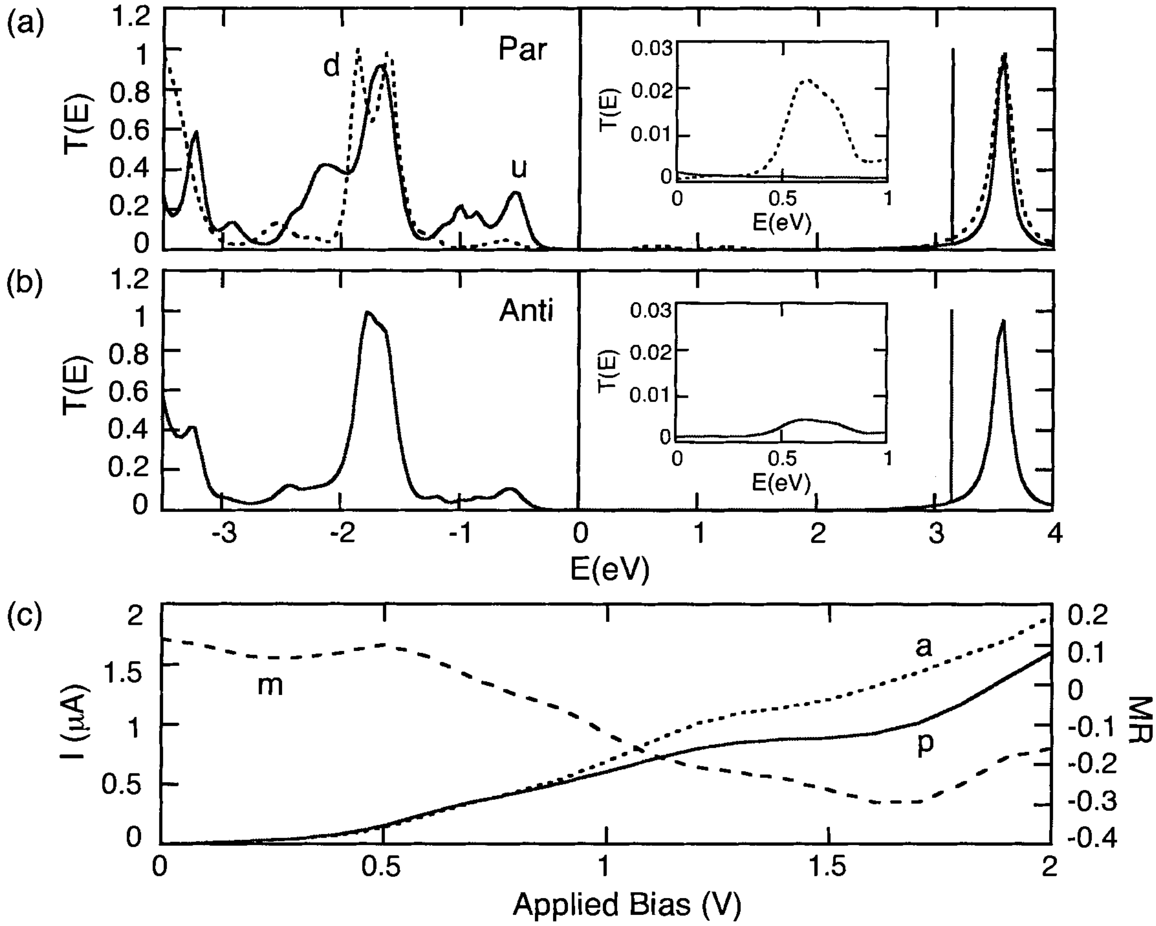

Figure 4.4: Spin-dependent transport for the Fe-BDT molecular wire in Fig. 4.3. (a) Transmission probabilities vs. energy at zero bias for the spin *up* → *up* (u) and *down* → *down* (d) configurations for parallel magnetizations. Fermi energy $= 0eV$. (b) Spin *up* → *down* transmission for anti-parallel magnetization. Expanded views of the transmission probabilities are shown in the insets. (c) Current vs. voltage for parallel (p) and anti-parallel (a) magnetizations. MR (m) is also shown.

(macroscopic) Fe leads. Having significant sulfur content (as shown in Figure 4.2), the molecular HOMO and HOMO-1 hybridize strongly with continuous metal states of the electrode, forming transmitting states giving rise to the strong transmission $1.4 - 2eV$ below the Fermi energy, $E_F = 0eV$. The peaks $3 - 4eV$ above the Fermi energy are due to the molecular LUMO and LUMO+1. The sharp resonance at $3.1eV$ results from extremely weak hybridization between the Fe leads and the isolated molecule's LUMO which has very little sulfur content (as depicted in Figure 4.2). Both the HOMO and LUMO of BDT are π-like orbitals similar to that of benzene, thus offer de-localization of electronic states resulting in roughly unity transmission near those levels.

More important, however, as they dominate the current at moderate bias (the HOMO and LUMO resonances do not enter the window of integration in Eqn. (2.1) up to $2V$ and so do not contribute resonantly to the current in Fig. 4.4(c)), are resonant states arising from strong hybridization between the molecular sulfur and the Fe d-electron orbitals. In Figs. 4.4(a,b) these states give rise to the broad transmission features, which predominate for spin up-electrons, between the Fermi energy and the HOMO resonances mentioned above. The hybridized states also produce weaker transmission resonances above the Fermi energy (that can be seen in the insets) for spin $down$ electron transmissions.

A representative molecular orbital for a hybridized state with energy approximately $0.5eV$ below E_F (in the range of the broad transmission resonance in Figure 4.4(a)) for parallel magnetizations and spin up configuration is displayed in Figure 4.5(a). The hybridized states are localized predominantly on the Fe electrodes and the adjacent sulfur atoms (i.e., on the metal-molecule interface unlike the HOMO and LUMO resonances that are perfectly conducting due to de-localization on the benzene ring) thus are termed *interface states*. Interface states allow electrons to transmit efficiently between the metal and molecule and so give rise to moderately strong transmission dominating the current in the experimentally accessible moderate bias regime. At zero applied bias for parallel magnetization of the contacts, the spin up Fe d-orbitals with energy below E_F hybridize very strongly with sulfur states on *both* sides of the molecule and transmitting orbitals form on each electrode as shown in Fig. 4.5(a). This results in the dominant u transmission near (below) the Fermi energy in Fig. 4.4(a).

The spin $down$ d-orbitals, occurring higher in energy and further from the molecular HOMO, hybridize more weakly[5] with molecular sulfur states producing weaker transmission resonances in Figure 4.4. For anti-parallel magnetizations (i.e., $up(down) \rightarrow down(up)$ transmission), only the source (drain) contact hybridizes strongly with molecular sulfur states at energies below E_F resulting in weaker $up \rightarrow down$ (ud) transmission

---

[5] The strength of the hybrid resonances in relation to their energy location relative to the HOMO resonances from which they hybridize will be investigated in detail in Chapter 5.

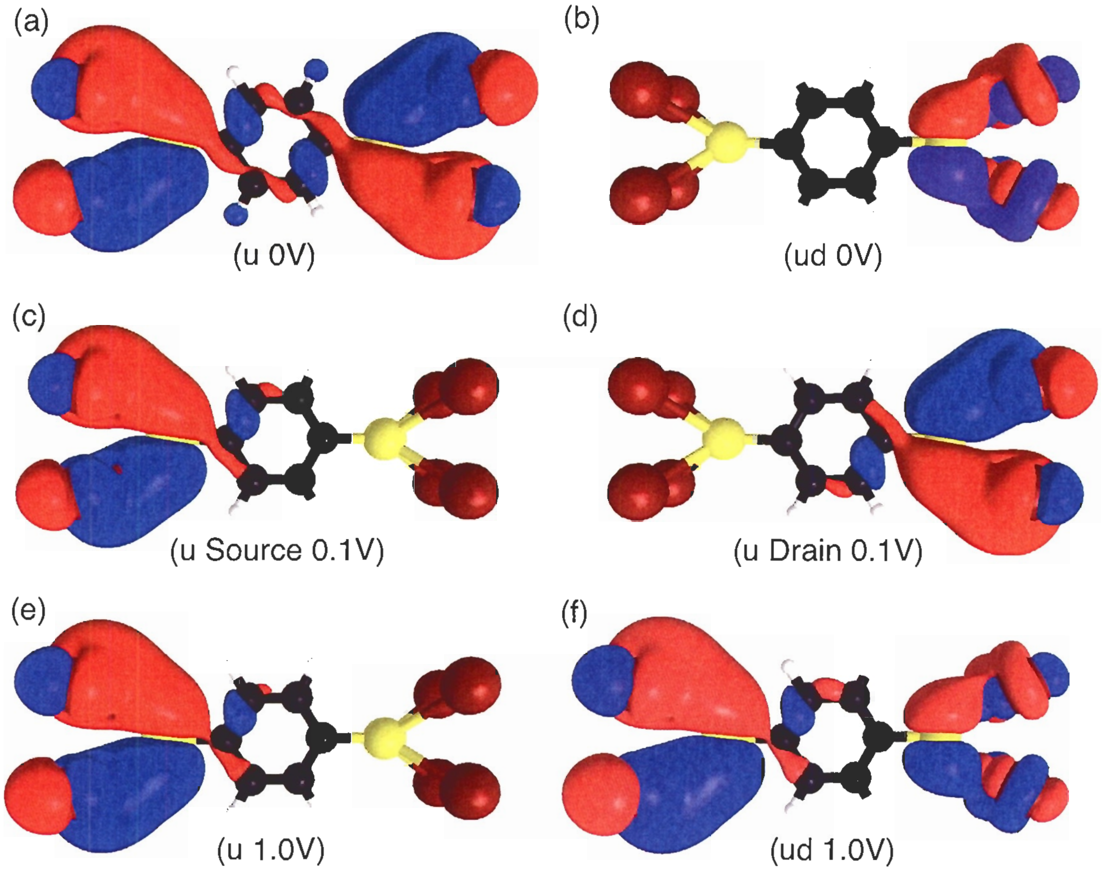

Figure 4.5: Representative hybridized energy eigenstates (red/blue indicates phase) of the entire extended molecule near the Fermi energy are depicted on ball-and-stick models of the BDT molecule and the 2×2 Fe planes on either side. (a) At $0V$ the u source (left) and drain (right) Fe electrode d-states hybridize with sulfur orbitals on *both* sides of the molecule forming transmitting states. In the *up* → *down* (ud) configuration, the source strongly hybridizes (as in (a)) with sulfur states, while the drain hybridizes at higher energies forming the weakly transmitting state displayed in (b). At $0.1V$, u states in (a) split into a state mainly on the source (c) that shifts upwards in energy and a state mainly on the drain (d) that shifts downwards. (e) At $1.0V$ u hybridized states on the source and drain have shifted well apart. (f) Source *up* hybridized states are shifted into resonance with drain *down* states in the ud orientation creating states that transmit strongly through the molecule.

there in Figure 4.4(b) than the u transmission in Fig. 4.4(a). Similarly, only the drain (source) contact hybridizes at energies above E_F, resulting in the even weaker transmission resonance in the inset of Figure 4.4(b). An interface state with energy near the weak resonance in Fig. 4.4(b), is displayed in Figure 4.5(b) for the spin ud orientation.

An applied bias breaks the symmetry between the source and drain electrodes in the parallel magnetization configuration. Thus the symmetric zero bias molecular orbitals (as in Fig. 4.5(a)) are supplanted by states associated mainly with either the source or drain electrode as shown in in Figure 4.5(c,d) for u transmission. The orbital in Figure 4.5(c) is shifted upwards in energy and is associated with the source electrode, while that in Figure 4.5(d) is shifted downwards and is associated with the drain. These orbitals can be traced to the zero bias orbital in Figure 4.5(a) and their energy splitting corresponds to the applied bias. Since the energies of these states are not perfectly aligned, simultaneous resonant transmission through both ends of the molecule is impossible. However, since the states remain close in energy at moderate bias, they *both* contribute *coherently* to near-resonant transmission via the extended molecule's Green's function (Eqn. (2.19)) in the Lippmann-Schwinger scattering formalism: There is appreciable coherent mixing between their off-resonant transmission tails resulting in relatively strong u transmission. The corresponding molecular orbital for ud transmission (at similar energies) resembles that shown for the source electrode in the u configuration in Figure 4.5(c), however a state with similar energy corresponding to the u drain state is absent. The reverse is true for du transmission and since these two transmission processes are mutually incoherent, there is no mixing of their off-resonant tails and the current in the case of anti-parallel magnetizations is weaker.

Fig. 4.4(c) shows the corresponding finite-bias current-voltage characteristics. As the interface states are not located *exactly* at the Fermi energy, they contribute to the current at very low bias through their off-resonant tails. The current under bias grows as more interface state resonances contribute to the transmission through the expanding conduction window determined by Eqn. (2.1). Since the u transmission dominates, the parallel magnetization current is larger, resulting in a positive magnetoresistance (calculated via Eqn. (3.1)) of about 10%. At larger applied bias, the applied electrostatic potential breaks the symmetry between the contacts further and the u transmission decreases as the hybridized Fe d-states associated with the source and drain move apart. However, at high bias in the case of anti-parallel magnetizations, interface states associated with *down* d-electron orbitals on the drain (as in Fig. 4.5(b)) are shifted into resonance with *up* d-electron states on the source: Hybridized transmitting states connecting *both* sides of the molecule with the electrodes form in the case of *up* $\longrightarrow$ *down* transmission as shown in Fig. 4.5(f), enhancing the transmission. No such resonant effect occurs for du transmission which decreases with increasing bias and so the *overall* effect of the applied bias on the *net* transmission for anti-parallel magnetization is small. No resonant enhancement occurs at increased bias for parallel magnetizations where hybridized states are shifted apart (Fig. 4.5(e)) and transmission is reduced. Therefore, because it selectively depresses transmission for parallel magnetization of the contacts, the bias-induced symmetry breaking results in a cross-over with increasing bias from positive to negative values of the MR in Fig. 4.4(c), analogous to the negative MR that was predicted for Fe QPCs in Chapter 3 that accompanied the resonant enhancement under bias in the spin *up* $\longrightarrow$ *down* channel depicted in Figure 3.5.

The spin-splitting of the interface states and their energy location at zero bias is comparable to that of the strong transmission resonances in Figure 3.4 for Fe QPCs which were shown to be influenced by the bulk and surface densities of states of the Fe electrodes; the energy location of interface states in the present class of molecular systems is influenced strongly by the energy location of d-electron orbitals and thus also influenced by features in the Fe bulk and surface (especially the surface) densities of states (Figure 3.1). The highly spin-split interface states give rise to the strongly spin-dependent transport characteristics.

The wave functions of the interface states responsible for transport at moderate bias are located primarily on the Fe electrodes. Therefore their energy levels are pinned to the electrodes and shift rigidly with applied bias explaining why the predicted moderate bias results are insensitive to the assumed potential profile. A more detailed investigation of interface states and their associated transmission resonances will be presented in Chapter 5.

Since the HOMO resonances in Figures 4.4(a,b) do not come close to the window of conduction (as determined by Eqn. (2.1)) for the results presented here (up to $2V$ in Fig. 4.4(c)), the HOMO is not expected to charge appreciably as the bias is increased in this range. Thus the simple assumed potential profile that accounts qualitatively for the effects of capacitive charging of the electrodes is expected to be reasonable. This is supported by the robustness of the predictions here to variations in the model potential profile. The interface states that dominate the current in the moderate bias regime are located mainly within the metal contacts and are well separated in energy from the Fermi levels of their respective leads. They are strongly coupled to their respective electrodes, whereas the calculated electron transmission probabilities via them from electrode to electrode are low (i.e., interface states on the source and drain electrodes are not strongly coupled to each other). Thus these states are always close to being in equilibrium with their respective electrodes and are therefore not expected to charge (i.e., change their electron occupations) appreciably in response to the application of bias. Furthermore the molecular LUMO levels are located at energies that are too high for them to become charged for the moderate bias voltages examined here. Therefore, because charging of the molecule in response to applied bias is not expected to be important, a single-particle electronic mean field theory, and in particular the hybrid electronic structure method and phenomenological potential profile employed throughout this thesis, is expected to be applicable to transport in these systems.

The preceding estimate for ΔE (the energy difference between the molecular HOMO level and the Fermi level of the metal at zero bias) neglects the effects of charge transfer between the electrodes and molecule; as sulfur is more electronegative than Fe, the Fe-S bond is expected to be polar covalent. Thus an electric field may establish in the vicinity of the metal-molecule contact, inducing a shift in energy levels relative to the above approximation. Variations in ΔE were modeled to simulate qualitatively possible changes in the potential distribution associated with charge transfer. Decreasing ΔE produced stronger hybridized resonances than those described above, as the HOMO and Fe d-electron orbitals become closer together in energy, while increasing it produced weaker resonances. The energy location of the interface states relative to E_F is robust to such variations, supporting the strong influence on the transmission by the Fe DOS. Thus although charging effects may influence quantitative results, the qualitative predictions presented here are robust to such charge transfer effects. Variations in the Fe-S bond length of $\pm 10\%$ had similar implications for quantitative results while qualitative predictions were robust to such variations.

For BDT bridging Fe nanocontacts, the cross-over to negative magnetoresistance occurs at relatively low bias, near $0.7V$, well within the range of current experimental techniques and therefore the predicted negative magnetoresistance should be accessible to experiment. With magnitude reaching more than 30%, the negative magnetoresistance may be more easily observed in this system than positive values. Since spintronic devices can in principle exploit magnetoresistance of either sign, molecular-Fe systems (with negative MR larger in magnitude than both positive values and the experimentally measured 12% for

Ni-molecular wires) may be attractive candidates for technological applications in devices based on molecular spintronics, but operated in the negative magnetoresistance regime.

Clearly this mechanism of negative MR is expected to be unique to systems that can both sustain a significant potential drop and allow for resonant transmission of d-electrons through the junction, i.e., nanosystems. Negative magnetoresistance emerging as a result of applied bias has already been observed experimentally in systems where ferromagnetic electrodes are separated by thin-film (metal-oxide) tunnel junctions only a few nanometers in width where the junction couples strongly to the electrode d-states [103, 104, 107]; states that form at the metal-insulator interface in those systems are analogous to the metal-molecule interface states predicted in this work. Since d-electrons (and interface state transmission) are not expected to contribute significantly to transport in conventional thin-film magnetic tunnel junctions more than a few nanometers thick [95, 96, 98, 100, 101], negative magnetoresistance when observed in those devices is often attributed to impurities [124]. However, the present theoretical prediction of *intrinsic* negative magnetoresistance in ideal systems demonstrates that bias-dependent and negative magnetoresistance are not necessarily signatures of impurities in molecular nanosystems.

For comparison, transport in an Fe/BDT/Fe molecular junction with a different geometry was also studied (not shown): Single Fe tip atoms were added to each of the clusters and the molecular sulfur atoms were bonded directly over them at the same heights considered previously (the S-C bond is assumed perpendicular to the surface). This geometry results in stronger and sharper resonances associated with the interface states and therefore the mechanism responsible for negative MR is even more prominent. Here the cross-over to negative magnetoresistance was found to occur at a lower bias voltage of $0.25V$.

4.3.2 Insulating Fe-Molecular Wires: Octane-dithiolate

Ferromagnetic Fe contacts bridged with a very different type of molecule (an insulator) will now be considered. The extended molecule for 8 carbon alkane-dithiolate, or octane-dithiolate (ODT), bridging Fe contacts is shown in Figure 4.6.

As for BDT, the S-C bond for ODT is assumed perpendicular to the Fe surface. This is consistent with the negligible S-C tilt obtained for DFT geometry relaxations of octane-thiolate (OT) on Au4 [65]. The resulting tilt angle of the molecule's carbon backbone

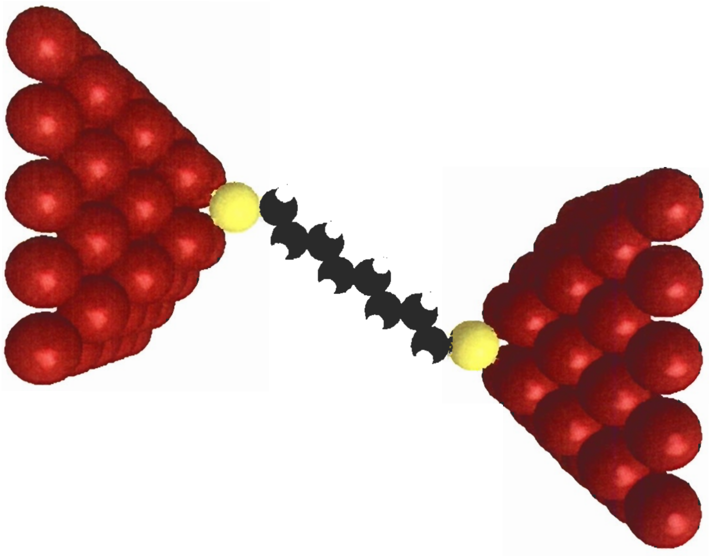

Figure 4.6: Extended molecule for a Fe-octane-dithiolate molecular wire.

is approximately 36^o consistent with previous theoretical ($\sim 30^o$) [122] and experimental ($30 - 34^o$) [125] studies of alkane-thiolate SAMs on Au (111) surfaces. Hollow site adsorption and an Fe plane-S distance of 2.0Å is assumed.

The HOMO-LUMO gap predicted with *un-modified* extended-Hückel theory is approximately $8eV$ for ODT, which is in close agreement with the accepted value for alkane-thiols[6]. Thus no modification of the phenomenological parameter K in Eqn. (2.12) is required for alkane-thiol molecules, i.e., $K = 1.75$. The technique developed in Section 2.6 produces $\Delta E = 1.76eV$. Taking into consideration the difference between work functions of Fe and Au ($0.4eV$ difference [66]), this estimate is in close agreement to the estimate obtained from experimental results for alkane-thiols between gold contacts [13].

The zero bias transmission probabilities for the Fe-ODT molecular wire are shown in Figure 4.7 for parallel (a) and anti-parallel (b) magnetization of the contacts. As ODT is an insulator, the strongest transmission features near the Fermi energy are weak resonant features associated with the (nearly degenerate) HOMO, roughly $1.8eV$ below the Fermi energy; because alkane carbon bonds are saturated (with hydrogen atoms), de-localized π-orbitals are not present and the HOMO is weakly transmitting, in contrast to BDT. Hence,

---

[6] See endnote 32 of Ref. [13].

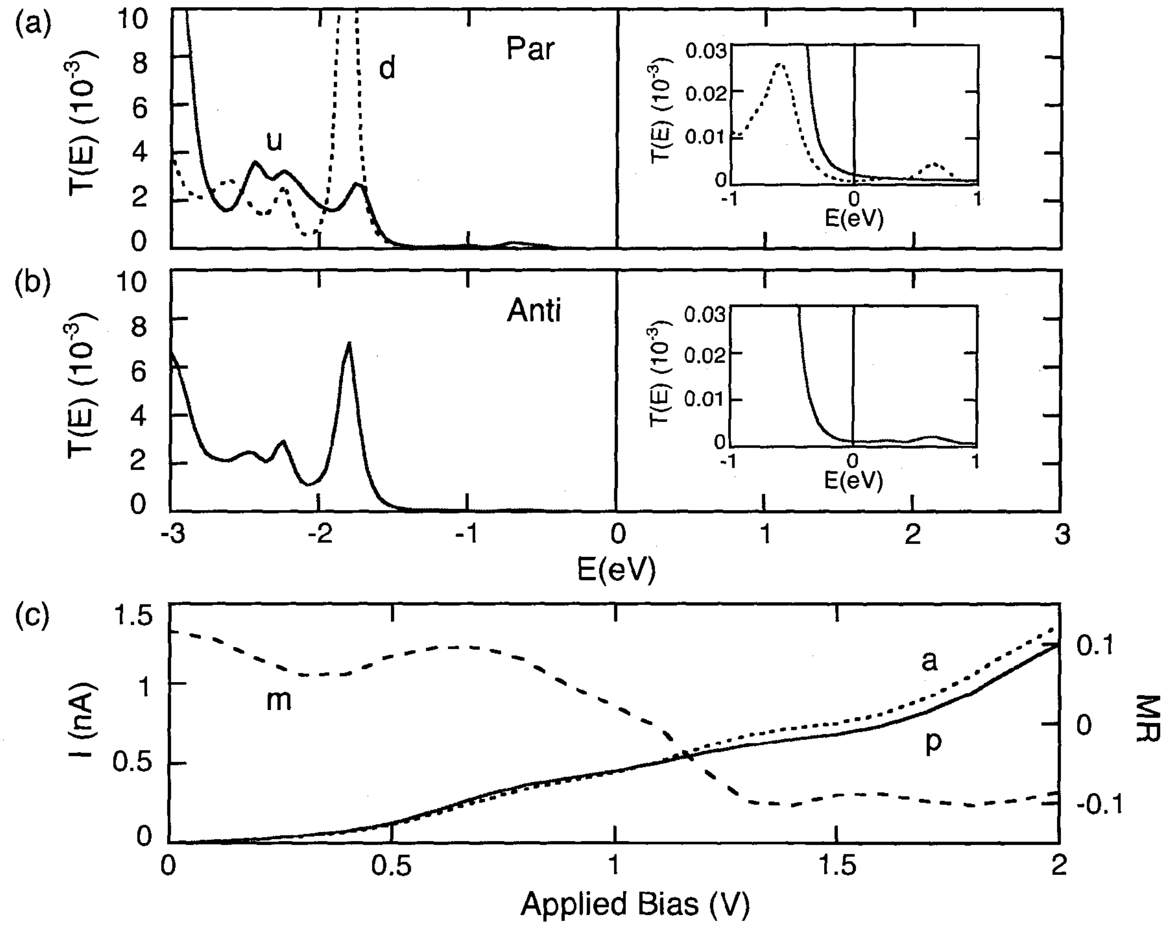

Figure 4.7: Spin-dependent transport for the Fe-ODT molecular wire in Fig. 4.6. (a) Transmission probabilities vs. energy at zero bias for the spin u and d configurations for parallel magnetizations. Fermi energy $= 0eV$. (b) Spin ud transmission for anti-parallel magnetization. (c) Current vs. voltage for parallel (p) and anti-parallel (a) magnetizations. MR (j) is also shown.

the HOMO is localized mainly at and near the sulfur atoms and decays rapidly along the molecule's carbon backbone. Transmission through the LUMO occurs at higher energies than those plotted (due to the large HOMO-LUMO gap of ODT). Other weakly transmitting states appear closer to the Fermi energy (about $0.5eV$ below) due to hybridization of molecular sulfur and Fe d-orbitals. These states are similar to those predicted in the case of BDT: the $up \rightarrow up$ transmission is largest as Fe up d-electron states are closest in energy to the ODT HOMO. Similar to BDT, weak *down* interface resonances predicted above E_F are shown in the insets. The fact that the interface states are located similarly to those for conducting Fe-BDT molecular wires reflects the importance of the Fe d-states and their energy location as represented by surface and bulk DOS (as summarized in Chapter 3).

The calculated current-voltage characteristics are shown in Figure 4.7(c). At moderate bias, symmetry between the source and drain electrodes in the parallel magnetization configuration leads to positive magnetoresistance. At higher applied bias, by the same mechanism described for BDT, the magnetoresistance becomes negative, but here the cross-over doesn't occur until nearly $1.2V$. The similar trends in magnetoresistance for insulating and conducting molecular wires are indicative of the robustness of the mechanism and its dependence on the electronic states at the Fe-S interfaces.

Because its mechanism relies on the simultaneous suppression of transmission for parallel magnetizations on the contacts and enhancement of the transmission in the anti-parallel ud transmission channel, this intrinsic negative magnetoresistance requires strongly spin-split energy bands providing a large magnetic moment. No such negative magnetoresistance has been reported for calculations on symmetric molecules bridging ferromagnetic *nickel* junctions [38, 40, 41, 42] and calculations on similar systems performed in the course of the present research[7] suggest that this different behavior may be related to the smaller spin-splitting in Ni: At sufficient bias to induce resonant transmission in the ud channel (the required bias is relatively small for Ni) much symmetry and overlap remain in the u transmission channel where energy levels are not adequately shifted apart. In addition, maximal features in the DOS for Ni electrodes occur on the *same* side of the Fermi energy for both spin configurations [64] and thus any enhanced transmission in the spin ud channel may contribute only off-resonantly to the current. Therefore the mechanism should be less effective in nanosystems based on nickel. However a related mechanism for negative magnetoresistance based on the appearance of *asymmetric* interface states in Ni contacts bridged with spatially asymmetric molecules (as were considered in the experiment [47]) will now be presented.

---

[7] For example, see the calculated transmission for Ni-ODT in the following section (Fig. 4.10(a)).

4.4 Spin-dependent Transport in Asymmetric Molecular Wires with Ni Contacts

The predictions of the previous sections for molecular wires with ferromagnetic Fe contacts indicate that bias-dependent and negative MR may be intrinsic properties of at least some molecular junctions, i.e., they are not necessarily signatures of impurities in such systems. The corresponding phenomena will now be investigated for ferromagnetic nickel contacts bridged by a single 8 carbon alkane-thiolate, or octane-thiolate (OT), molecule (nickel contacts separated by a SAM of OT molecules were investigated experimentally [47]).

Experimental studies have indicated that methyl-thiolates adsorb on Ni (100) surfaces in four-fold hollow site positions [126, 127] and that the molecular S-C bond is normal to surface [127]. Similar surface geometries are therefore assumed for the Ni-OT molecular wire. Each Ni cluster of the extended molecule is built from $5\times5, 4\times4, 3\times3, 2\times2$ (100)-oriented layers (54 atoms total) of atoms in the bulk geometry of FCC Ni. The perpendicular four Ni atom plane-S separation is estimated to be 1.773Å; the separation between the molecular carbon atom (on the non-thiolated molecular end) and the Ni electrode is estimated as 4.1Å [65]. While the magnitudes of the currents depend exponentially on the Ni-C separation, the magnetoresistance is qualitatively insensitive to this separation for a range of values. The qualitative predictions are also not overly sensitive to the Ni-S distance. The Ni/OT/Ni extended molecule is displayed in Figure 4.8.

The hybrid semi-empirical tight-binding model of Section 2.6 is used to model the electronic structure of the Ni-molecular wire[8]; a similar tight-binding model has been used previously to investigate transport through Ni-BDT molecular wires [38]. In contrast to the relatively small separations predicted between the sulfur atoms and metal contacts for dithiolated molecules in the previous sections, a substantial spatial gap is predicted at the interface between the metal contact and the non-thiolated molecular end of OT. In the numerical results presented here, for simplicity, it is assumed that half[9] of the applied bias

---

[8] The Fermi energy alignment is estimated to be $\Delta E = 1.26eV$.

[9] Approximating the molecular wire system as a parallel-plate capacitor with plates separated by a heterogeneous junction formed from two materials with different dielectric constants (a molecular film with a dielectric constant of $2.5-3$ and air) yields a potential profile where approximately $1-1.5$ times as much bias drops over the molecule as over the vacuum gap.

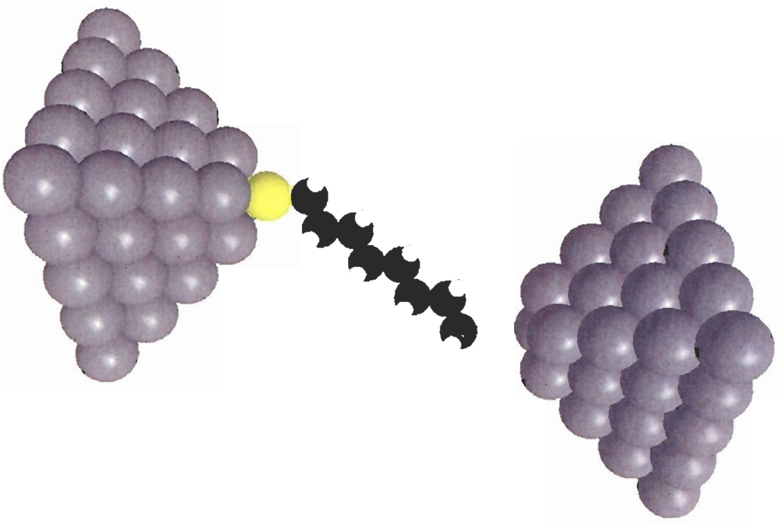

Figure 4.8: Extended molecule for a Ni-octane-thiolate molecular wire. Each Ni cluster consists of 54 Ni atoms arranged in the bulk geometry of (100) FCC Ni.

voltage drops at this interface and half drops across the molecule. The predicted magnetoresistance shows no strong sensitivity on the details of the potential profile as they are varied from one in which the bias drops linearly between the two contacts and one in which it drops entirely over the large spatial gap.

The calculated spin-dependent electron transport results are presented in Figure 4.9 for the Ni/OT/Ni molecular wire[10]. As displayed in Figure 4.9(d), the magnetoresistance for Ni/OT/Ni is predicted to be strongly bias-dependent and to become negative for both signs of the applied bias. The negative MR is again related to enhanced transmission in the spin ud channel (as seen in Figure 4.9(b)) that for this system occurs at *zero* bias; negative MR results primarily from the spatial asymmetry of the molecular bridge, not from the relative shifts of spin *up* and *down* contact states due to the application of applied bias (as was found for Fe-molecular wires). Thus negative MR for Ni/OT/Ni is predicted to result from a combination of interactions at the *different* metal-molecule interfaces:

The transmission features in Figures 4.9(a,b) may be understood as manifestations of

---

[10] The convention of current flow is that positive bias induces a net electron flux from the thiolated side of the molecular wire, i.e., with the right contact at a positive electrostatic potential relative to the left. $I(-V) \neq -I(V)$ as the system is not mirror symmetric in the direction of electron propagation.

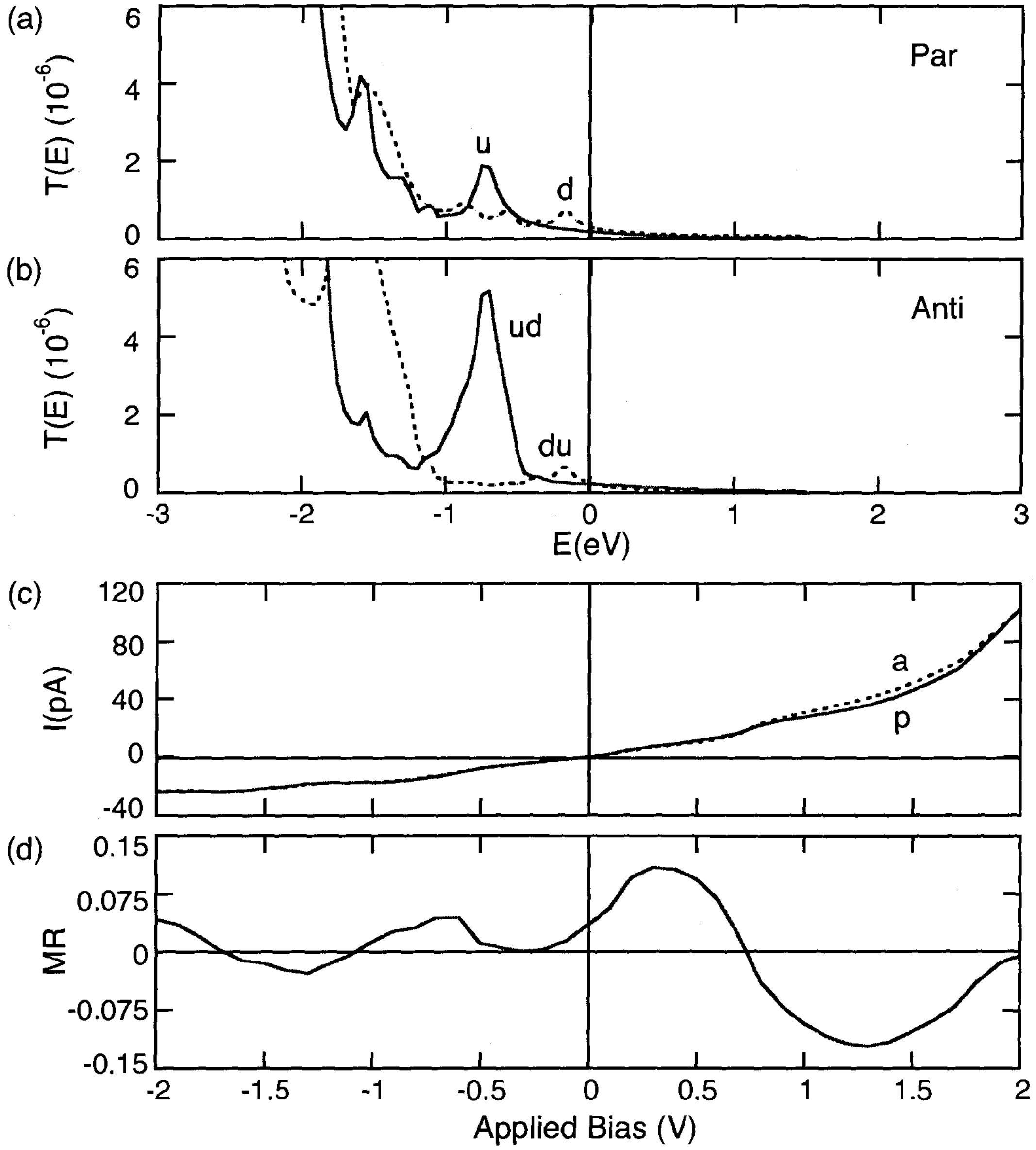

Figure 4.9: Spin-dependent transport for the spatially asymmetric Ni/OT/Ni molecular wire in Figure 4.8. (a) Transmission probabilities vs. energy at zero bias for the spin u and d configurations for parallel magnetizations. Fermi energy $= 0eV$. (b) Spin ud and du transmission probabilities for anti-parallel magnetization. (c) Calculated current vs. applied bias voltage for parallel (p) and anti-parallel (a) magnetizations. (d) Magnetoresistance vs. bias voltage.

consecutive transmission of electrons through the two different metal-molecule interfaces of the Ni/OT/Ni junction. However, since a molecular wire can not be constructed with a *single* metal-molecule interface, in order to develop an intuitive understanding of the predicted effects, the transmission through two closely related *symmetric* molecular junctions will be considered next (the physical justification for this analysis is provided in Appendix D): Figure 4.10(a) shows the zero-bias transmission probability for a molecular wire where both metal-molecule interfaces are similar to the thiol-bonded contact of Ni/OT/Ni (i.e., this transmission is for a Ni/ODT/Ni wire); Figure 4.10(b) is for both interfaces similar to the non-thiolated contact (i.e., for Ni/octane/Ni)[11].

The transmission resonances near the Fermi energy in Figure 4.10(a) (labeled u and d for the different spin orientations) are (as for Fe-molecular wires) due to interface states; they occur as a result of strong hybridization between the sulfur orbitals of ODT and Ni d-orbitals, and are located in the vicinity of the Ni density of states maxima for the respective spin configurations. Since Ni d-energy bands are energetically localized and spin-split, a relatively sharp interface state resonance occurs (at different energies) near the Fermi energy for spin up (u) and down (d) configurations. Similar spin-split resonances have been predicted as the primary source for strong magnetoresistance in symmetric Ni-molecular junctions [38, 42, 44]. However, as they are located here on the *same* side of E_F, resonant inversion under bias of MR (as was predicted for Fe-molecular wires) is suppressed in symmetric Ni-molecular wires.

Figure 4.10(b) displays the transmission probability for Ni/octane/Ni. Since the octane molecule is not strongly bonded to either contact, such a geometry is unlikely to be physically realizable. Nevertheless, it is instructive to consider the transmission through the junction and how it relates to that for Ni/OT/Ni. Since the molecule is not strongly bonded to either contact, strong hybridization of molecule-metal states does not occur and octane simply lowers the barrier for conduction; the resonant states labeled u and d are metal states for the different spin configurations (they are present also for vacuum tunneling between Ni contacts in the absence of any molecule).

---

[11] The symmetric junctions are created by geometrically mirroring the left or right spatial halves of the asymmetric Ni/OT/Ni junction (without further geometry relaxations). The Fermi energy alignment of the contacts is the same in all three model systems, using that of the Ni/OT/Ni wire as the reference. Parallel magnetization is assumed in all cases.

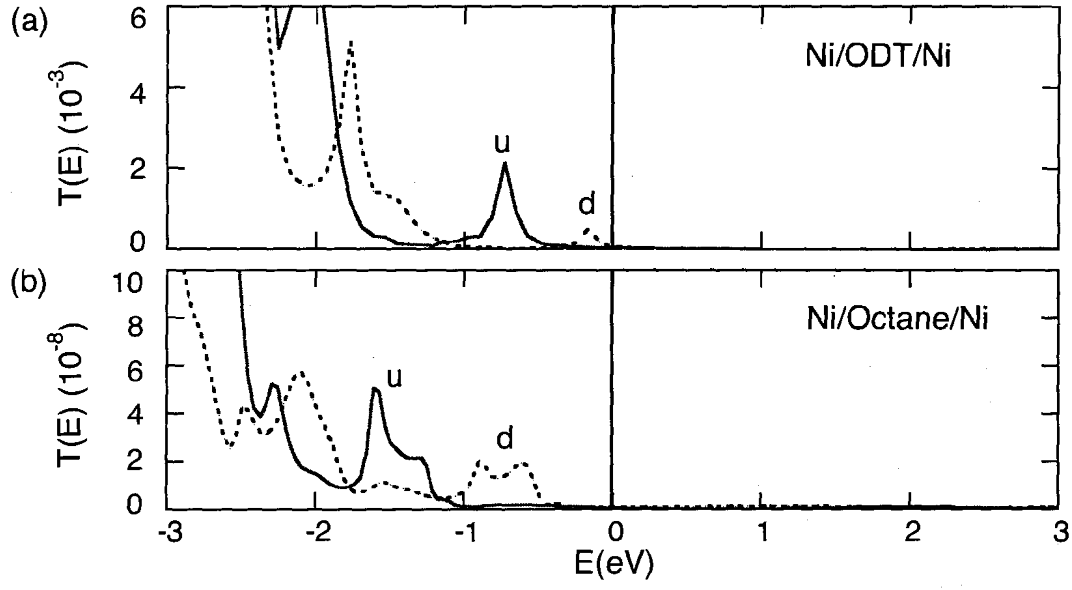

Figure 4.10: Spin-dependent transmission probabilities at zero bias for symmetric Ni-molecular wires. (a) Transmission probabilities for the spin u and d configurations for a Ni/ODT/Ni molecular wire. (b) Transmission probabilities for a Ni/octane/Ni wire.

The transmission features in Figure 4.9(a,b) for Ni/OT/Ni may now be understood as convolutions of the transmission functions in Figures 4.10(a,b) (see Eqn. (D.2)). In the case of parallel magnetizations of the two contacts, the resonances u and d in Figure 4.9(a) are located as those in Figure 4.10(a). They are clearly due to interface state formation at the Ni-S interface and are weaker than those in Figure 4.10(a) as interface states form only on one side of OT (the side thiol-bonded to the Ni contact). Transmission features due to the metal resonances of Figure 4.10(b) are also clearly present in Figure 4.9(a).

For anti-parallel magnetizations, the resonance labeled du for *down* → *up* transmission in Figure 4.9(b) is again due to the interface state resonance d in Figure 4.10(a). It is comparable in magnitude to d in Figure 4.9(a) as the interface state forms only on one side of OT. For *up* → *down* transmission, a significant transmission resonance emerges near $0.7eV$ below the Fermi energy. Here the interface state u in Figure 4.10(a) exactly overlaps the metal state d in Figure 4.10(b) and the transmission is greatly enhanced for the *up* → *down* spin configuration of OT. Therefore, the transmission resonances for Ni/OT/Ni (that dominate measurable quantities in the experimentally accessible moderate bias regime) are due to a combination of interface states and metal resonances.

While the transmission resonance labeled ud in Figure 4.9(b) decreases in magnitude with bias (as states on either side of the molecular junction are shifted apart), it maintains its dominance over a wide range of bias voltages. Hence, once the bias increases sufficiently so that the ud resonance enters the window of integration in Eqn. (2.1), the MR inverts, as displayed in Figure 4.9(d). Therefore, strong bias-dependence and inversion of the MR are predicted for *ideal* Ni/OT/Ni molecular tunnel junctions suggesting that such phenomena are not necessarily signatures of impurities (in contrast to the rationale provided by Petta *el al* [47]). Furthermore, the maximum MR predicted in Figure 4.9(d) is approximately 12%, inline with that obtained by the experiment [47], suggesting that the MR may *not* have been limited by the presence of impurities. Both the experimental value and the theoretical estimate are markedly lower than the 21% predicted by the Julliére formula (Eqn. (3.4)) with commonly accepted spin polarizations for Ni electrodes [91]. This apparent contradiction will be resolved in the following section.

Quantitative comparison with experiment [47] is, however, difficult. First, a titanium adhesion layer between the non-thiolated OT end and the Ni contact was employed in the experiment. Such a Ti layer is known to react with molecules, likely forming a Ti-carbide layer [128] that is not considered in the present theoretical study. Also, the MR was observed to decay on a voltage scale of approximately $50mV$ (roughly an order of magnitude faster than predicted in Figure 4.9(d)); such short MR decay scales have been attributed (among other factors) to the presence of impurities in conventional MTJs [98]. Strong temperature dependence, that has also been attributed to the presence of impurities [98], was also observed in the experiment. These observations suggest that, though perhaps not responsible for all of the observed phenomena, metal impurities may have been present within the experimental molecular film.

Moreover, because the device was realized with a 'nanopore' geometry (with an evaporated top metal contact) the surface orientation of the contacts is unknown (and may not even be crystalline). Experimental studies have indicated that thiolated molecules adsorb also on Ni (111) surfaces [129, 130, 131]. Calculations performed in the course of the present research for Ni/OT/Ni junctions with (111) surface orientations yielded similar bias-dependent and negative MR trends to those for (100) orientations. However, in some cases (depending on the binding site) a MR maximum of $\sim 30\%$ was predicted (*larger* than that predicted by the Julliére estimate) while in others, negative MR on the same small voltage scales (as was observed in the experiment) was calculated. The latter predictions were not, however, as robust to variations in model electronic and structural properties. Quantitative comparison between the present theory and experiment [47] thus requires atomic characterization of the experimental system that was not carried out experimentally, and better sample preparation techniques that do not rely on the inclusion of a titanium layer in the system.

4.5 Effective Spin Polarizations of Molecular Wires

In the preceding section, a maximum magnetoresistance of approximately 12% was calculated for a Ni/OT/Ni molecular wire with (100) Ni contacts, markedly lower than the 21% predicted with the Julliére formula (Eqn. (3.4)) and commonly accepted spin polarizations for Ni electrodes (P=0.31) [91]. The MR was predicted to be strongly bias-dependent and to become negative, also in apparent contradiction to the Julliére theory of SDT. Along with the predicted results for Fe-molecular wires displaying similar trends, these results suggest that the Julliére formula together with measured spin polarizations for bulk Ni electrodes is inadequate.

It is well known that the magnetoresistance of conventional MTJs is sensitive to interface effects [95, 96, 98, 100, 101, 102, 103, 104, 105, 106, 107]. In the preceding sections, interface effects were predicted to *dominate* the conduction for ferromagnetic systems bridged with molecules at moderate bias voltages. Hence, the present research suggests that if the Julliére formula is to be used reliably, the commonly accepted bulk spin polarizations must be replaced with *effective spin polarizations* due to each contact [101] that include the influence of the metal-molecule interface. The electronic simplicity of the Ni/OT/Ni molecular MTJ, namely the tunneling nature of the conductance (i.e., the HOMO is not strongly conducting), the large HOMO-LUMO gap, that the conducting states at low bias are located mainly within the Ni contacts, and the weak bonding between the Ni contact and the molecular carbon atom, allows quantitative values for effective spin polarizations to be extracted for this system.

A procedure for extracting bias dependent *quantitative* effective spin polarizations that are influenced strongly by both the ferromagnetic leads and the coupling to the molecule

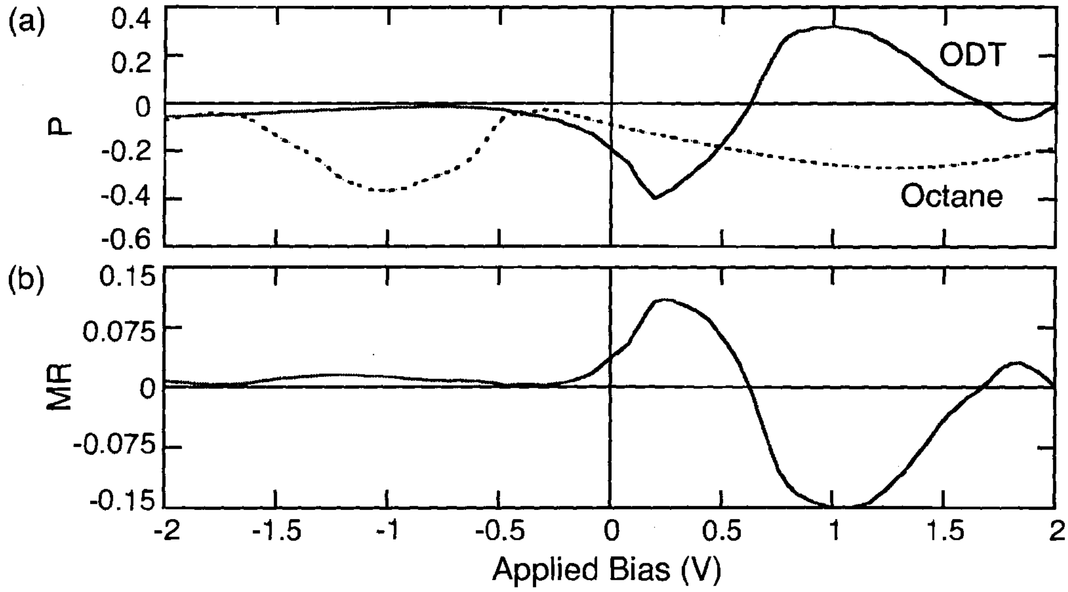

Figure 4.11: Effective spin polarizations and MR for a Ni/OT/Ni molecular wire. (a) Effective spin polarizations vs. bias voltage. ODT labels the spin polarization of the thiol-bonded Ni contact of the Ni/OT/Ni junction. Octane labels the spin polarization for the non-thiolated contact. (b) Magnetoresistance calculated with the Julliére formula and effective spin polarizations in (a).

is outlined in Appendix D. Together with the Julliére formula (Eqn. (3.4)), the calculated effective spin polarizations of each Ni/OT/Ni contact that are shown in Figure 4.11(a) reproduce the main features of the calculated magnetoresistance (Figure 4.11(b) is qualitatively similar to Figure 4.9(d)). As displayed in the figure, the resulting spin polarizations are strongly bias-dependent and very different from their commonly accepted bulk values [91]. These spin polarizations indicate that the bulk spin polarization of Ni should not be used as the basis for MR calculations once the Ni electrodes have been bridged by a molecule; as the calculated effective spin polarizations are bounded by neither +31% nor -31% (the measured values for Ni electrodes [91]), it is clear that bulk spin polarizations can not be used reliably even to calculate upper limits for the magnetoresistance. (This is supported by the calculated MR maxima of $\sim$ 30% for Ni-molecular wires with (111) surfaces predicted in the previous section.)

Similar effective spin polarizations may be obtained for the symmetric molecular wires based on Fe (though for conductive wires such as those involving BDT the analysis is strictly *qualitative*), however, the important conclusions are clearly demonstrated in Figure 4.11(a) for Ni/OT/Ni by the radically different spin polarizations associated with each of the asymmetric contacts. In Figure 4.11(a), the spin polarization of the thiol-bonded contact (labeled ODT) starts out negative at low bias due to the dominance of the spin *down* transmission near the Fermi energy as in Figure 4.10(a). As the interface states are shifted to higher energies under bias into the window of conduction, the effective spin polarization starts to increase becoming positive as the spin *up* resonance (as in Figure 4.10(a)) enters the window. Due to the dominance of the spin *down* Ni-metal states (as in Figure 4.10(b)), the effective spin polarization for the non-thiol-bonded contact is negative throughout the range of bias voltages shown in Figure 4.11(a). Thus, as the spin polarizations of the two contacts for Ni/OT/Ni become opposite in sign, the Julliére formula (Eqn. (3.4)) predicts negative magnetoresistance in Figure 4.11(b) similar to that predicted in Figure 4.9(d) by the full quantum mechanical calculation. Thus, if the commonly accepted spin polarizations for isolated ferromagnetic electrodes are supplanted by *effective* spin polarizations that include the influence of the metal-molecule contacts, the Julliére Eqn. (3.4) may yield reliable predictions for spin-dependent transport phenomena. However, since such an approach requires a full quantum mechanical calculation, while it provides intuitive insights, it offers no additional predictive power. However, the concept that the properties of an asymmetric molecular wire can be understood in terms of those of a pair of symmetric wires at zero bias (expressed quantitatively in Equations (D.3) and (D.4)) is extremely useful for identifying systems that may exhibit novel properties, as discussed in the two chapters that follow.

4.6 Conclusions

Molecular wires with ferromagnetic Fe contacts were predicted to exhibit pronounced magnetoresistance effects, i.e., to function as molecular spin valves. Bias-dependent and inverse magnetoresistance phenomena were predicted for systems where Fe electrodes are bridged by two very different molecules (conducting and insulating). The phenomena were attributed to states that develop at the Fe metal-molecule interface due to the strong chemical bonding between molecular sulfur orbitals and Fe d-electron orbitals; resonant enhancements in the interface state transmission (that dominate the current) for parallel and anti-parallel magnetizations on the source and drain contacts were predicted for some values of the applied bias voltage. Relatively large in magnitude and occurring at modest applied bias voltages, the negative magnetoresistance predicted here should be accessible with present day experimental techniques. Thus Fe-molecular wires may be attractive candidates for technological applications in devices based on molecular spintronics, but operated in the negative magnetoresistance regime.

Bias-dependent and negative magnetoresistance was also predicted for ferromagnetic nickel contacts bridged with an asymmetric octane-thiolate molecule. These results suggest that similar trends observed in experimental data may be *intrinsic* to such molecular tunnel junctions, i.e., not dependent on the presence of impurities within the molecular film. (However experiments on better quantity samples characterized at the atomic scale are clearly desirable.) The transport mechanism responsible for these phenomena in Ni/OT/Ni molecular wires was predicted to result from *asymmetric* interface state formation due to the spatial asymmetry of the octane-thiol molecule (as opposed to the negative magnetoresistance induced primarily by applied bias voltage for Fe-molecular wires). Thus, in principle, negative magnetoresistance for Ni/OT/Ni wires may be attainable at very low (or even *zero*) applied bias voltages.

The effects of asymmetry of the molecular junction (with symmetric nickel leads) and applied bias voltage are beyond the scope of the classical Julliére theory for spin-dependent transport with commonly accepted spin polarizations for nickel electrodes; a methodology for extracting quantitative *effective* spin polarizations of each contact under bias voltage was developed in this chapter. When used together with the Julliére theory (in place of the commonly accepted spin polarizations for Ni electrodes), the effective spin polarizations, that are strongly dependent on the Ni/OT/Ni metal-molecule interface and strong functions of applied bias, reproduce the bias-dependent magnetoresistance predicted by detailed quantum mechanical calculations.

Chapter 5

Interface States, NDR and Rectification in Molecular Wires with Transition Metal Contacts

5.1 Introduction

The results presented in Chapter 4 for molecules bridging electrodes of different contact materials and surface structures demonstrate that the structural and chemical characteristics of the metal-molecule interfaces are expected to significantly affect the transport properties of molecular wires. Many theoretical studies have elucidated the nature of such effects in gold/molecule/gold junctions for which the influence of the specifics of the molecules themselves and of the atomic geometry of the Au interface on transport has been investigated in great detail [5, 25, 26, 27, 29, 30, 67, 120, 132, 133, 134, 135, 136]. There has also been interest in molecular wires with other noble metal contacts including silver, copper, and aluminum with transport results comparable to those for Au [132, 137].

For thiolated molecules bridging Au electrodes, some studies have predicted very weakly transmitting hybridized molecular-contact states to appear within the molecular HOMO-LUMO gap [135, 136]. These metal-induced gap states (MIGS) or interface states form as a result of hybridization between molecular thiol groups and surface states of the metal contacts. In Au/molecule/Au molecular wires, these interface states have been shown to play only a *minimal* role in transport [135, 136].

In contrast, metal-molecule interface states were, in the previous chapter, predicted to *dominate* the transport for molecular wires with iron electrodes leading to unusual transport phenomena including inversion of the magnetoresistance under bias [43]. Also interface states were (and have previously been [38, 42, 44]) predicted to dominate the current in molecular wires with nickel electrodes. Important differences between the Au and magnetic metal-molecule wires that lead to the crucial role played by interface states in systems of the latter type are due to the non-trivial d-electron character of the magnetic electrodes near the Fermi energy. Similarly, interface states that form near the Fermi energy due to hybridization between thiolated molecules and d-electron states of platinum [132, 138], palladium [132] and other transition metal [132] electrodes have been predicted to produce larger low bias conductances than for systems based on Au where d-orbitals play a relatively minor role.

In this chapter, the transport properties that emerge when simple organic molecules bridge *non-magnetic* transition metal electrodes that have more complex electronic structure than Au leads will be systematically investigated. As a prototype system, a single 4 carbon alkane-dithiolate molecule (or butyl-dithiolate, hereafter denoted AT4)[1] bridging Pd contacts[2] will be considered, however, the qualitative findings are applicable to a wide range of molecular wires consisting of different thiolated molecules bridging a variety of metal contacts with d-electronic states near the Fermi energy.

The non-trivial d-electron character of the transition metal electrodes will be shown to result in interesting transport properties (different from those of Au molecular wires) that are due to hybridized interface states between the molecular sulfur atoms and the metal contacts that form within the molecular HOMO-LUMO gap [49, 50]. These interface states *dominate* the transmission through the junction at moderate bias. Under bias, the energies of these interface states *lock* to the shifting electrochemical potentials of the contacts and, for some values of the bias, resonantly enhance the transmission (similar to the mechanism that

---

[1] Butyl-dithiolate is similar to octane-dithiolate but with a backbone consisting of four carbon atoms instead of eight. The molecules have similar electronic properties.

[2] Some previous studies have indicated that small Pd nanoclusters possess weak ferromagnetism, but that magnetism is limited to very small nanoclusters and even then is controversial [139]. As the Pd clusters considered in the following sections are of appreciable size (54 atoms) and employed to model real macroscopic leads, ferromagnetism is not relevant here.

was predicted to yield negative MR for Fe-molecular wires in the previous chapter), giving rise to non-linear transport phenomena including negative differential resistance (NDR)[3] and rectification. Thus a new mechanism for both NDR and rectification in molecular wires will be introduced [49, 50], that differs from previously proposed mechanisms[4] [1, 5, 7, 10, 12, 18, 22, 23, 32, 34, 134, 143, 144, 145, 146, 147, 148, 149, 150, 151, 152, 153, 154, 155, 156, 157, 158, 159, 160, 161] in that here resonant *interface state transmission* is the source of these phenomena. This prediction is far from obvious *a priori* since alkane-thiols are insulators and thus for simple metal contacts such as gold they display featureless, monotonic current-voltage characteristics (See for example Ref. [13]). Furthermore, the present results indicate that these transport phenomena are strongly dependent on the atomic parameters of the molecular junctions, which in principle will depend on how samples are fabricated and thus offer avenues for control of the properties of non-linear molecular electronic devices.

In Section 5.2, the methodology developed in Chapter 2 is applied to study Pd/AT4/Pd molecular wires at zero bias and the nature of the interface states that dominate the transmission probability at moderate bias is discussed in detail. The evolution of the interface states as the Pd electrodes are brought into increasingly close contact with the molecule is investigated. Next the dependence of the shape, strength and energy location of the interface state transmission resonances on the interfacial binding site and Pd crystal surface orientation is examined. The effect that increasing the length of the molecular carbon backbone has on the interface state transmission is also discussed and a decay parameter, β is extracted from the transmission calculations. Once the nature of the interface states has been elucidated, the effect of finite bias on the transmission is considered explicitly in Section 5.3. Because the interface states are localized mainly within the metal electrodes, their energies accurately track the electrochemical potentials of the contacts when a variable bias is applied

---

[3] Negative differential resistance is a *decrease* in current occurring in response to an *increase* in the bias voltage applied across an electronic circuit element. NDR has important device applications including high frequency oscillators [140], analog-to-digital converters [141], and logic [142].

[4] A number of possible explanations of NDR in molecular wires have been proposed including: current-induced charging or conformational changes in the molecules [7, 10, 143, 144, 145, 146, 147, 148], metal filaments [149] or impurities [150, 151] within the molecular layer, bond fluctuation [34], vibronic mediation [152, 153], and polaron formation [154]. These proposed mechanisms are complex and controversial and the NDR has been difficult, at best, to control experimentally.

across the junction leading to enhancements in the transmission for some values of applied bias. As introduced in Section 5.4, such resonant enhancement and reduction of the interface state transmission results in negative differential resistance in molecular wires with Pd nanocontacts. Moreover, the NDR may be *tailored* by suitably choosing the nanocontact materials: If a Rh electrode is substituted for one Pd contact, enhancement of these NDR effects is predicted. The same mechanism is also predicted to produce rectification in Pd/molecule/Au wires; the details are discussed in Section 5.5.

5.2 Interface States in Molecular Wires with Transition Metal Contacts

5.2.1 Nature of the Interface State Transmission

Palladium contacts are selected here as the prototypical material for studying molecular wires with transition metal electrodes[5]. Pd can be prepared with either (100) or (111) oriented surfaces[6]. Thus while Pd (100) oriented electrodes are assumed at the outset, molecular wires with Pd (111) electrodes are also investigated in the sections that follow. Hollow site molecular binding is assumed; top binding sites for thiols on Pd (111) and Pt (111) surfaces have been predicted least stable [162]. Each Pd cluster included in the Pd/AT4/Pd extended molecule (not shown) is built from $5 \times 5, 4 \times 4, 3 \times 3, 2 \times 2$ (100)-oriented layers (54 atoms total) of atoms in the bulk geometry of FCC Pd. The sulfur atoms of AT4 are estimated to sit 1.74Å above the four-fold Pd hollow site [65] and the molecular S-C bond is assumed perpendicular to the surface.

As for the ferromagnetic metal-molecular wires in the preceding chapters, the electronic structure of the (Pd, Pt, Rh, and Au) molecular wires in this chapter is described by the hybrid semi-empirical tight-binding model of Section 2.6. Thus the tight-binding parameters for the metal clusters, $H_C^{L,R}$, are based on fits to *ab initio* non-magnetic band

---

[5] Calculation and experiment have demonstrated that thiolated molecules chemisorb on both palladium and platinum surfaces [162, 163, 164].

[6] Atomic reconstructions of the electrodes, that may occur physically as macroscopic Pd electrodes come together in a nanoscale region to contact a molecule, are not considered.

structures of the metal crystals [64][7]. The molecular electronic parameters, H^M, as well as the electronic parameters describing the molecular coupling, $W_M^{L,R}$, to the electrodes are described by the (unmodified) tight-binding formalism based on extended-Hückel theory. For Pd contacts, the separation between the Fermi energy and HOMO of AT4 is estimated to be $\Delta E = 1.49eV$.

The calculated transmission probability at zero bias for the Pd/AT4/Pd molecular wire is shown in Fig. 5.1. The nearly degenerate molecular HOMO gives rise to the broad transmission $1.5 - 2eV$ below the Fermi energy $E_F = 0eV$; it is weakly transmitting because the HOMO of AT4 is primarily localized on the sulfurs and only weakly de-localized on the carbon backbone. The LUMO resonance lies outside of the plotted energy range due to the large HOMO-LUMO gap of AT4. More important, however, as they influence the current at lower bias, are resonant states within the HOMO-LUMO gap (similar to those that were predicted for Fe-molecular wires in Chapter 4) arising from strong hybridization between the molecular sulfur and Pd d-electron surface states. In Fig. 5.1 these states give rise to the relatively sharp transmission features (the double-peaked feature) between the Fermi energy and the HOMO resonances mentioned above. The inset in Figure 5.1 shows a representative molecular orbital for an interface state with energy in the range of the transmission peak closest to the Fermi energy; interface states responsible for each peak have similar molecular orbital character. The electronic wavefunction is spatially localized on the sulfur-metal region, (the metal-molecule interface) therefore these molecular orbitals are *interface states*; not much of the wavefunction lies on the carbon backbone. (As they result from hybridization of the molecular HOMO, the interface state molecular orbitals on the atoms of the molecule have similar character to that of the HOMO for isolated AT4.)

An important difference between the interface state and the HOMO resonances in Figure 5.1 is that the former appear well within the molecular HOMO-LUMO gap very near the Fermi energy. Another difference is that the interface resonances are due primarily to hybridization of the molecular HOMO with metal d-orbitals whereas the HOMO resonance arises primarily from hybridization between the molecular HOMO and metal s and p-orbitals; the interface state resonances completely disappear if the coupling between the metal d-orbitals and the molecule is switched off. The HOMO resonance does not. The energies of the interface state resonances are comparable to those of Pd electrode d-electron

---

[7] The transmission probability is spin-independent thus a multiplicative factor of 2 appears in Eqn. (2.1).

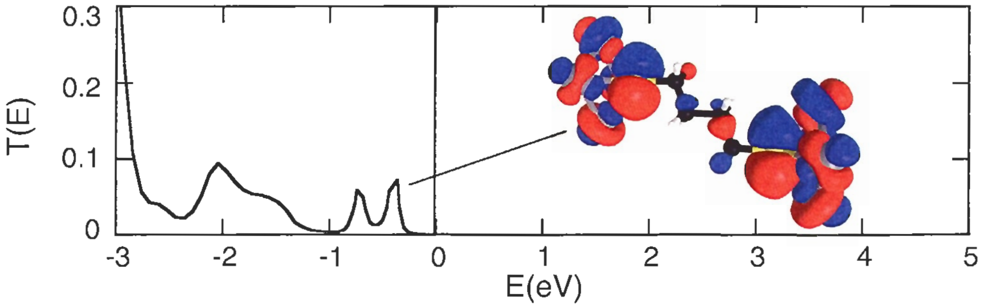

Figure 5.1: Transmission probability at zero bias for the Pd/AT4/Pd molecular wire. $E_F = 0eV$. The inset displays a ball-and-stick model of the molecule and four surface atoms of each contact with a molecular orbital plot for an interface eigenstate (of the entire extended molecule) with energy in the range of the transmission peak closest to the Fermi energy.

orbitals as determined from maxima in the bulk [64] and (100) surface [165] densities of states for Pd. The sharpness of the interface state transmission features near the Fermi energy relative to the resonances associated with the HOMO reflects the fact that Pd d-electron bands are energetically localized; because transmission through the HOMO is dominated by Pd s and p-electrons, which are described by broader energy bands, the molecular HOMO broadens severely (Figure 5.1).

These interface state transmission features can be contrasted to Au-BDT systems (Refs. [30, 135] for example), and results for Au-AT4 obtained in the course of the present research, where the d-electron states for Au are below the molecular HOMO in energy and so are largely out of range at low bias, hence, interface state formation is negligible. In molecular-transition metal systems, such as BDT or AT4 bridging Pd, Pt, Rh, Cr, Mo, Ni or Fe, where the electron d-states are close in energy to the Fermi energy, interface states have been found in the present work to be the dominant features at low bias. In particular, once the interface states have been formed (the molecule-lead separation is at its equilibrium value so that the molecule-lead coupling is strong) the interface state resonances in general appear close in energy to the maxima in the transition metals' densities of states (both bulk and surface DOS are relevant as noted in the previous chapters for molecular wires with Fe electrodes), which are dominated by d-electronic states.

The interface states are located primarily within the metal contacts. Because of this, as will be shown in Section 5.3, the energies of the interface states under bias lock to the shifting electrochemical potentials of the contacts, making these energy levels strongly dependent on the bias, leading to resonant enhancements in the transmission (and current through the molecule) for some ranges of bias.

5.2.2 Evolution as Molecule is Contacted

More insight into the interface states and their formation can be gained by studying their evolution as the molecule is brought into contact with the leads. To that end, the transmission through the Pd/AT4/Pd system will now be studied as a function of separation between the thiols and the Pd contacts. Figure 5.2(a-d) shows the transmission at zero bias as a function of increasing thiol-Pd separation, where symmetry of the system is maintained by simultaneously varying the Pd-S separations on *both* ends of the molecule. For comparison, Figure 5.2(e-h) shows transmission results for a sequence of geometries that should be more readily accessible experimentally; here the thiol-Pd distance is fixed at its equilibrium value on one side of the molecule (the molecule is bonded to that contact), while the distance between the other contact (which may represent an STM tip) and the molecule is allowed to vary. Similar results are predicted in both cases, but the differences arising from increasing the separation are more prominent in the symmetric case.

As the thiol-contact separations are increased from the predicted 1.74Å equilibrium value (Figure 5.1) to 2Å, the result for which is shown in Figure 5.2(a), the transmission near the Fermi energy remains dominated by interface states. Hybridization of the HOMO occurs for a slightly smaller energy range of Pd electron states and as a result the interface state resonances are located slightly further from the Fermi energy (closer to the molecular HOMO). The interface state resonance becomes larger in magnitude, while the structure of the HOMO resonance also changes. As discussed below, such effects arise not only from changes in the Pd-S coupling, but as a result of changing properties of the *whole* system and therefore are difficult to quantify *a priori*. As the separation is increased to 2.3Å, as in Figure 5.2(b), the transmission becomes more energetically localized near the HOMO resonance where it grows in magnitude (note the change in y-axis scale in Figure 5.2(b)) while the interface state resonance is diminished. Also the interface state resonance shifts further towards the broadened HOMO, as hybridization occurs with an even smaller range

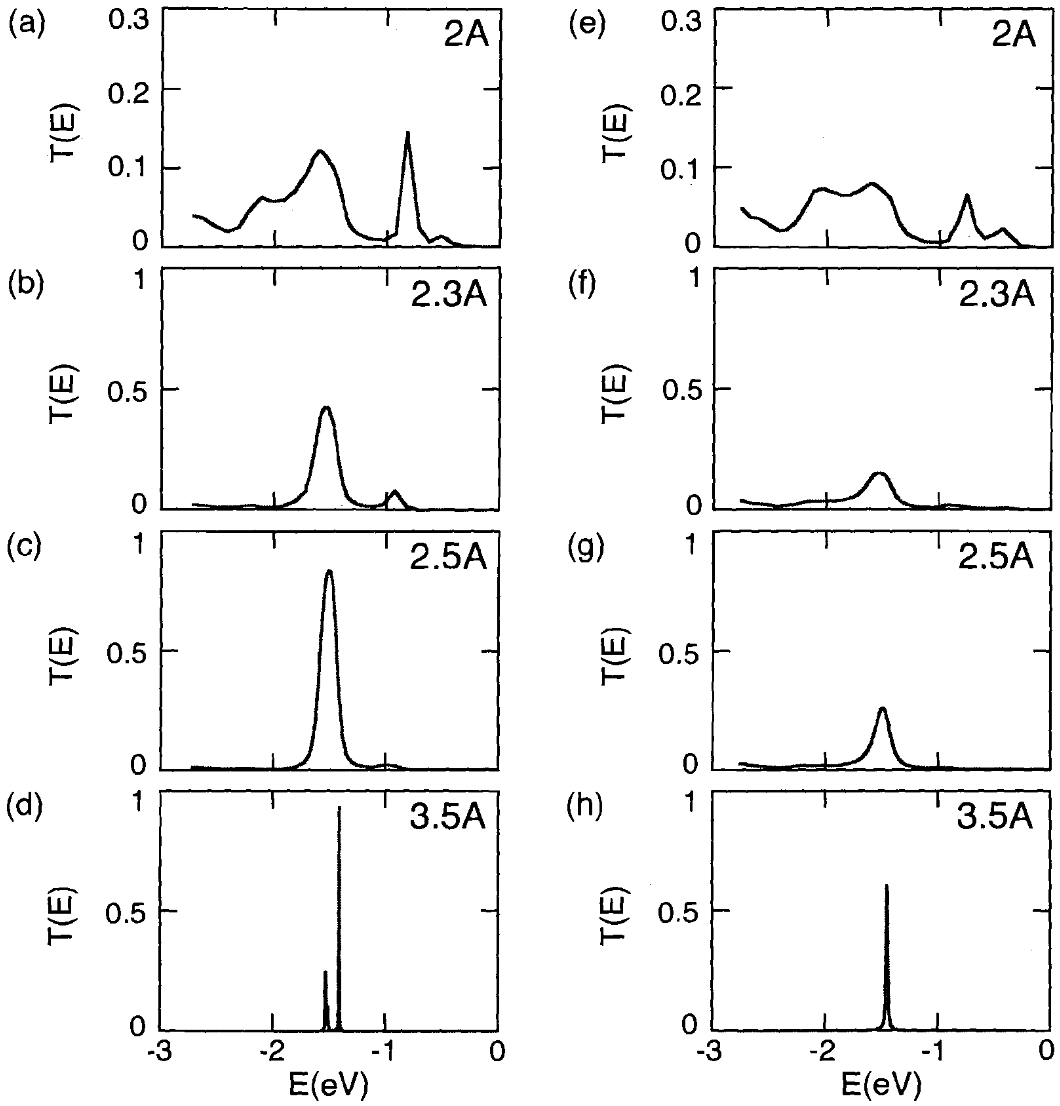

Figure 5.2: Transmission probabilities at zero bias for increasing thiol-Pd contact separation for the Pd/AT4/Pd molecular wire. $E_F = 0eV$. (a) Transmission probability with the Pd-S separation increased to 2Å for both contacts symmetrically. (b) 2.3Å Pd-S separation. (c) 2.5Å. (d) 3.5Å. (e-h) Corresponding transmission probabilities for a sequence of STM-like geometries with one Pd-S distance fixed at the equilibrium value (1.74Å) and the other varied as in (a-d), respectively.

of Pd electron states. This trend continues as the separation is increased to 2.5Å (Figure 5.2(c)), where only very slight formation of interface states occurs at the high energy side of the broadened HOMO resonance. As a result of the lack of sulfur hybridization with Pd electron states with energies much different from the HOMO, the HOMO resonance becomes quite localized and strong. As the distance is increased further to 3.5Å, as in Figure 5.2(d), no hybridization of the HOMO into interface states occurs, and the transmission through the HOMO evolves into two closely spaced peaks that are very narrow because of the weakness of the coupling between the molecular thiol groups and the electrodes at this separation; the HOMO of the isolated AT4 molecule (that is located primarily on the thiol end groups) is similarly split in energy.

The trends presented in Figure 5.2 can be understood as follows: For large Pd-S separations, the molecule is only weakly coupled to the Pd contacts and so molecular orbitals only weakly transmit. As the separation is decreased, the HOMO couples more strongly to the surface states of the Pd contacts and broad transmitting states begin to form. As the distance is decreased further, the distance-dependent wave function overlaps between the HOMO and Pd surface states with *different* energies become non-negligible, and the HOMO couples to more surface states resulting in stronger hybridization (energetically well-separated quantum states couple and mix together only once their hopping or coupling energies are comparable to their energy spacings). Since the maximum in the Pd DOS is energetically localized and slightly below the Fermi energy and mostly of d-electron character [64] (this is true for the surface DOS as well [165]), as the separation is decreased, the HOMO couples to more and more d-states near the Fermi energy, causing the overall upwards shift in energy of the interface state resonances. Near the equilibrium separation these transmitting states are well separated from the HOMO resonance and have evolved into interface states. Since the HOMO of AT4 is primarily localized on the sulfurs (only very weakly de-localized on the carbon backbone), as the coupling between the sulfurs and the Pd is increased, the nature of the HOMO changes significantly and the transmission through the HOMO is dramatically affected (reduced).

At this point it is worthwhile to point out a subtle distinction that exists between the coupling between the metal surface states and the sulfur orbitals, which gives rise to interface states (i.e., if the coupling is too weak, no hybridization into interface states occurs) and the coupling between electronic states deep in the lead and the interface states themselves.

The latter coupling controls the width and overall shape of the interface state resonances and is strongly dependent on the properties of not only the interface, but of the whole system. Therefore, this coupling is difficult to quantify *a priori*. This is exemplified by the variations in shape of the interface state and HOMO transmission resonances mentioned above and the differences in resulting transmission resonances that emerge upon binding the molecule at different surface sites, as discussed in the following section.

Also, as alluded to above, once the equilibrium separation has been reached, the energies of the interface states are strongly correlated with maxima in the bulk and surface metal DOS. For BCC transition metal leads, whose DOS show two distinctly separated maxima, interface states resonances are found to occur near each (as demonstrated for spin *down* transmission for Fe-molecular wires in Figure 4.4(a)). For FCC metal electrodes, interface state resonances such as those displayed in Figure 5.1 are predicted very near the maximum in the densities of states (bulk and surface DOS are relevant). Their *precise* energies, however, are dependent on the properties of the interface and of the whole system.

As an aside, it is clear from Figure 5.2(a) that if the equilibrium S-Pd separation were 2Å instead of the 1.74Å predicted by density functional calculations, interface state resonances would still dominate measurable quantities at low bias. Therefore the qualitative predictions presented here are not overly sensitive to the S-Pd separation.

5.2.3 Dependence on Surface Orientation and Binding Site

Pd can be prepared with either (100) or (111) oriented surfaces and molecules will adsorb on both. The effect on the interface states when AT4 molecules adsorb on (111) oriented Pd is now investigated. The transmission is calculated for each AT4 molecular sulfur atom symmetrically bonded over the (111) FCC and HCP hollow sites as well as a bridge site and a bri-FCC site[8], all of which have been predicted stable or nearly stable sites for thiol adsorption on Au [122, 166, 167]. The thiol-Pd distances are based on estimates from density functional calculations [65]. They are predicted to be 1.83Å for the hollow sites and 1.9Å for the bridge sites.

---

[8] The HCP site is a three-fold hollow site on the (111) surface in which a metal atom is present directly below in the second layer. No metal atom is present in the second layer for FCC sites. A bridge site is midpoint between two surface atoms and in the bri-FCC site, the molecule is adsorbed halfway between the bridge and FCC sites.

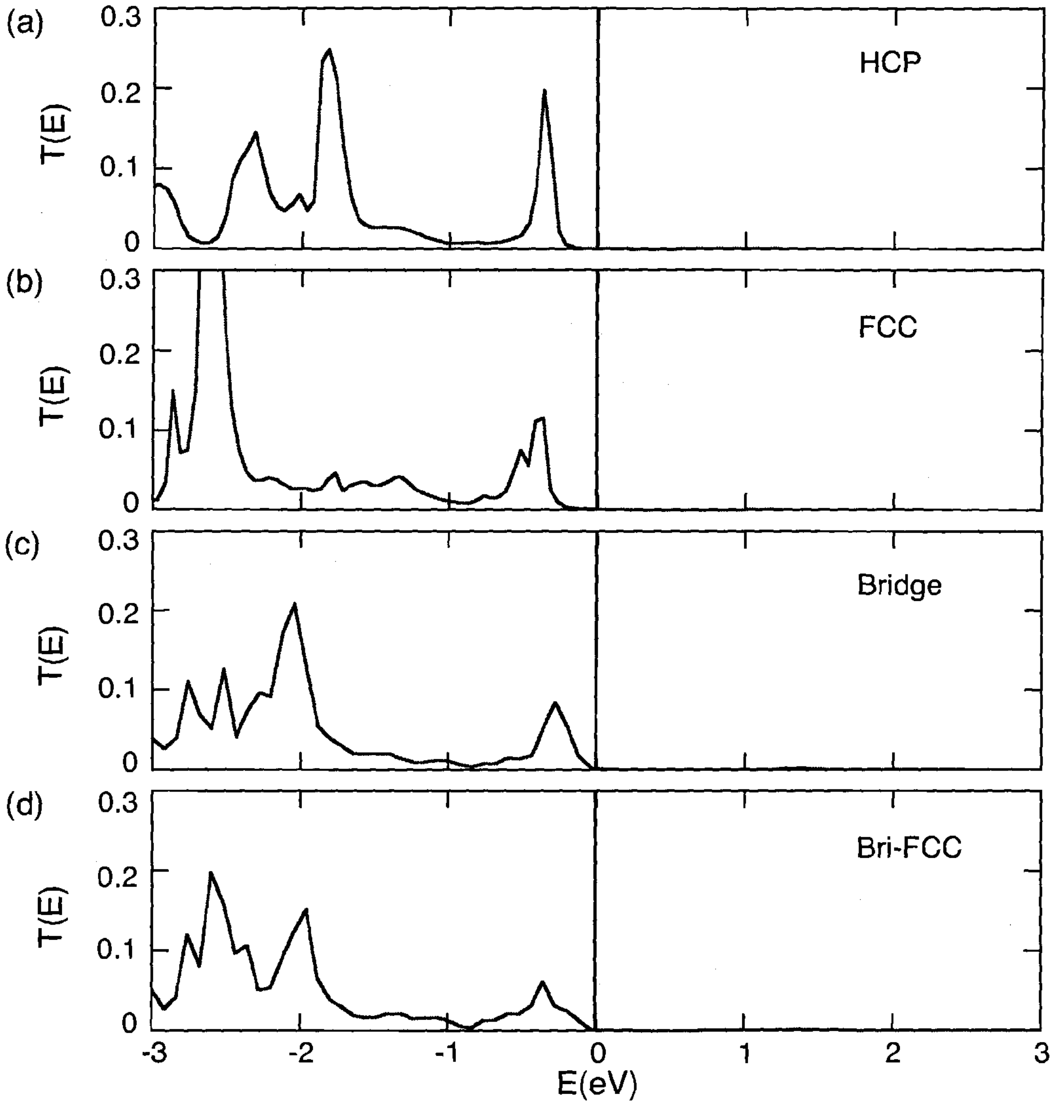

Figure 5.3: Transmission probabilities for different AT4 binding sites on (111) Pd contacts. (a) Molecular sulfur atoms adsorbed at HCP surface sites. (b) FCC surface sites. (c) Bridge site. (d) Bri-FCC site (sulfur atom adsorbs halfway between the FCC and bridge sites).

The results presented in Figure 5.3 (and Figure 5.1) reveal interface states to form near the Fermi energy for all binding sites and to be similarly located for all binding sites and surface orientations; subtle differences in the exact energies and differences in the size and shape of the interface state resonances are apparent for the different binding sites. These differences are due to the different geometries, i.e., S-Pd distances, different numbers of S-Pd bonds and different coordination numbers of Pd atoms at the surface, all of which strongly affect the overlaps between sulfur and Pd-*d* electron orbitals. The results indicate that the HCP binding site gives rise to the strongest interface state resonance (Figure 5.3(a)), while the bri-FCC site results in the weakest (Figure 5.3(d)). Both the bridge (Figure 5.3(c)) and bri-FCC site junctions result in the appearance of an interface state resonance closer to the Fermi energy than for the (100) surface site (Figure 5.1), while for the HCP and FCC (Figure 5.3(b)) sites it is only slightly closer. Additionally, the double-peaked interface state transmission feature, as in Figure 5.1, is present but not as prominent for the FCC binding site while only a single feature is present for the HCP and bridge site. The resonance is more broadened in the case of bri-FCC binding. Since the transmission resonances near the Fermi energy are associated with *interface* states, it is not surprising that differences emerge when switching orientations or binding sites and therefore changing the atomic structure of the interface.

The strength and shape of the HOMO resonance is also strongly dependent on surface orientation and binding site; the HOMO of AT4 is localized mainly on the sulfur atoms thus the resonance is sensitive to atomic variations in the S-Pd interface. As discussed above, the characteristics of both interface state and HOMO resonances are also strongly dependent on the properties of the whole system that extend beyond the metal-molecule interface.

5.2.4 Dependence on Length of the Molecule

To determine the relationship between interface state transmission and length of the insulating molecule, the transmission through molecular wires where n alkane-dithiolates (with $n = 4,6,8$ carbon atoms) bridge Pd contacts was also investigated. Both at zero bias, and under finite bias (see Section 5.3 below), the calculated transmissions for the three different molecules are quite similar in shape, differing by a scaling factor: The transmissions were found to scale as $e^{-\beta n}$ where n is the number of carbons and $\beta = 1.08$. This can be compared to theoretical results for n alkane-thiolates bridging Ni contacts ($\beta = 0.88$) [42], as well as theoretical ($\beta = 0.95$) [136] and experimental conducting AFM ($\beta = 1.2$ [9] and $\beta = 0.8$ [11]) and STM ($\beta = 1.0$) [19] results for Au contacts (see also [13]). This scaling of not only the very low bias tunneling background, but also of the resonances associated with the interface states reflects the fact that interface states allow electrons to resonantly tunnel into and out of the molecule-metal interface, reducing the width of the tunnel barrier. As the length of the molecule increases, so too does the width of the tunnel barrier and the resonances due to interface states scale with the background tunneling transmission.

5.3 Bias-Dependence of Interface State Transmission

In the previous sections the transmission characteristics at zero bias have been considered, however, interesting non-linear current-voltage and behavior of the transmission features due to interface states emerge once the effects of finite bias are explicitly included. As with the magnetic-molecular wires studied in Chapter 4, finite bias effects will be included through the heuristic model outlined in Section 2.9; one-third of the applied bias is assumed to drop at each interface and the remaining one-third linearly over the length the molecule [29, 58, 118]. As discussed below, the predictions are not sensitive to the details of the assumed potential profile.

The transmission probability as a function of energy for increasing bias for the (100) Pd/AT4/Pd molecular wire is shown in Figure 5.4. As shown in Figure 5.4(b), compared to the zero bias transmission probability in Figure 5.4(a), the applied bias results in an overall decrease of the strength of the resonances associated with the hybridized interface states. The reason for this is as follows: The wave functions of the interface states responsible for transport at moderate bias are located primarily on the Pd electrodes and are only weakly coupled through the molecule. (The molecular orbital plot in the inset of Figure 5.4(a) shows only the portion of the interface states on a ball-and-stick model of the molecule and surface layers of the electrodes.) Approximately 90% of the interface state wave functions reside on the Pd electrodes, while most of the remaining 10% is located on the sulfurs. Therefore the energy levels of the interface states are pinned to the electrodes and follow the electrochemical potentials of the their respective electrodes with applied bias; as the magnitude of the bias increases, the electrostatic potential energy of electrons on the drain decreases while that of electrons on the source electrode increases and the interface state resonances follow.

This is illustrated in Figure 5.5 where the energies S_1 and S_2 (D_1 and D_2) of the two interface states at the source (drain) Pd electrodes are seen to track the electrochemical

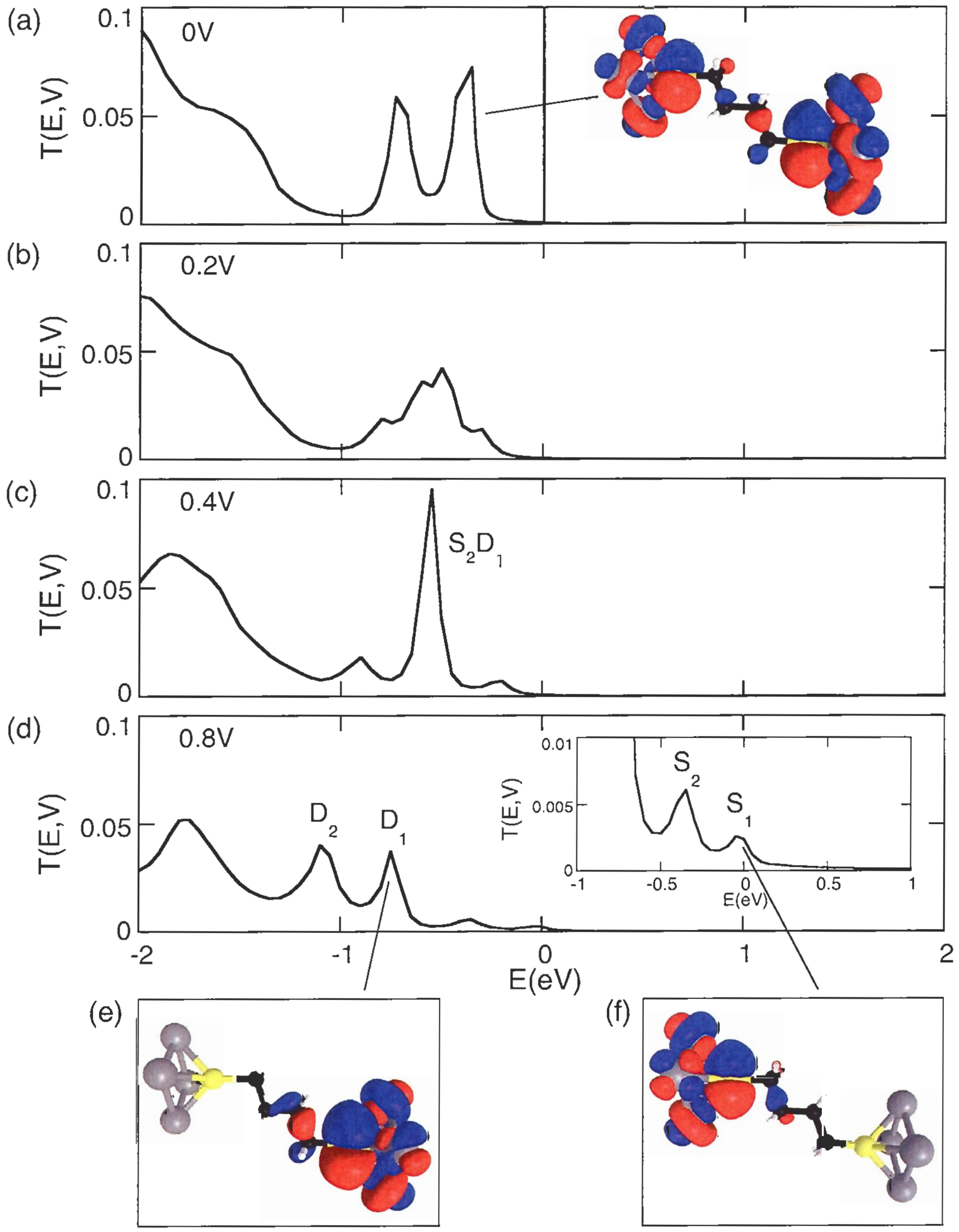

Figure 5.4: $T(E, V)$ for the (100) Pd/AT4/Pd molecular wire. (a) Transmission probability at zero bias. (b) $0.2V$ bias. (c) $0.4V$. (d) $0.8V$. Under bias the interface state in the inset of (a) is replaced with interface states associated with the drain (e) or source (f) electrodes.

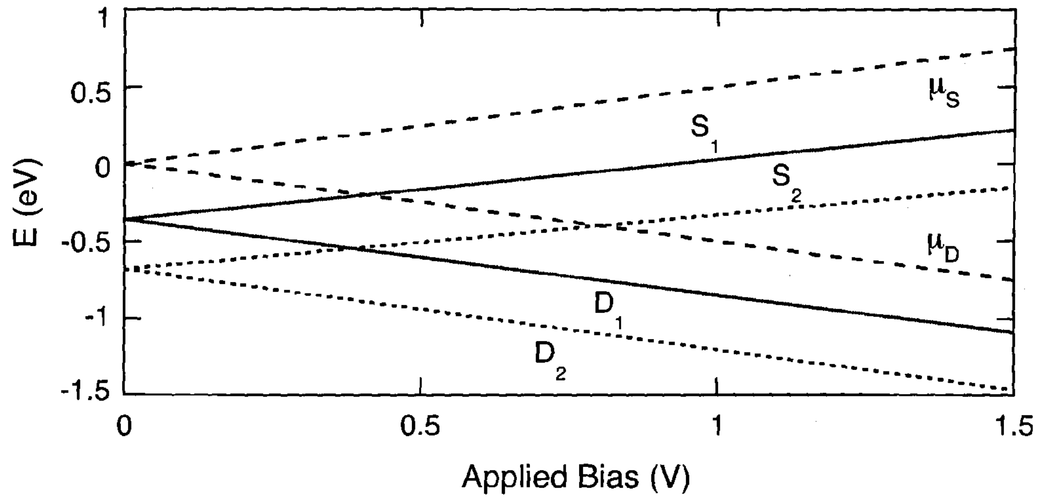

Figure 5.5: Energies of interface state resonances (solid and dotted lines) and electrode electrochemical potentials (dashed) labeled according to the respective electrode vs. bias applied across the Pd/AT4/Pd junction. S(D) stands for the electron source (drain) electrode, while 1(2) stands for the high (low) energy interface state.

potentials μ_S (μ_D) of their respective electrodes. At zero bias, interface states on the source and drain electrode are degenerate, and molecular orbitals form near the Fermi energy with significant wavefunction weight on *both* source and drain interfaces, as in the inset of Figure 5.4(a), resulting in the relatively strong transmission below the Fermi energy in Figure 5.4(a). As the interface states on the source and drain move apart with increasing bias, hybridization typically only occurs strongly at one end of the molecule at a given energy and the transmission at those energies is therefore diminished.

This effect is most clearly demonstrated at larger applied bias when the interface state resonances on the source and drain become well separated: Figures 5.4(e,f) show the effect of $0.8V$ applied bias on the interface state displayed in the inset of Figure 5.4(a), corresponding to the transmission probability in Figure 5.4(d). As the electronic states of the drain electrode are shifted down $0.4eV$ in energy, and the source up $0.4eV$ in energy, the degeneracy is lifted and the zero bias interface state in Figure 5.4(a) is replaced with interface states coupled to either the drain (Figure 5.4(e)) or the source (Figure 5.4(f)) electrodes. These two separated interface states give rise to the separated resonance peaks S_1 and D_1 (each being the higher energy peak of a double-peaked feature as in Figure 5.4(a)) in Figure

5.4(d) (A closer view of $T(E,V)$ due to interface states near $0eV$ is shown in the inset).

This mechanism results in the reduction of the transmission resonance near the Fermi energy as $0.2V$ bias is applied across the molecular junction (Figure 5.4(b)). At $0.4V$ applied bias (Figure 5.4(c)), the interface states responsible for the lower energy resonance of the double-peaked zero bias interface state transmission feature (near $0.8eV$ below E_F in Figure 5.4(a)) shift into resonance with those responsible for the higher energy peak (near $0.4eV$ below E_F in Figure 5.4(a)) and the transmission is *enhanced* at $0.6eV$ below the zero bias Fermi energy (labeled S_2D_1 in Figure 5.4(c)). As this enhancement of the transmission remains outside of the window of integration in Eqn. (2.1), (interface states D_1 and S_2 cross *outside* of the energy range between μ_S and μ_D at an applied bias of $0.4V$ in Figure 5.5) it will not *directly* contribute to the current, but can contribute weakly in an off-resonant fashion. Resonant enhancements and reductions in the transmission, especially when occurring *within* the current window, can give rise to non-linear transport phenomena such as NDR, as will be discussed in Section 5.4. They were also predicted in Chapter 4 to produced negative magnetoresistance for molecular wires with iron electrodes under bias. An intuitive, analytic two-level quantum model is presented in Appendix E to better understand these resonant enhancements.

Once the two transmission resonances have passed through one another, the interface states on the source and drain electrode continue to part in a monotonic fashion as in Figure 5.4(d). Departure from this trend occurs once the interface states on the drain contact shift into resonance with the broadened HOMO states $1.5-2eV$ below the zero bias Fermi energy. As this occurs well outside of the window of integration in Eqn. (2.1) for the low bias results presented here (up to $2V$ in Sections 5.4, 5.5), this will not be discussed further. As the interface states on the source side of the molecule are shifted higher in energy, the double-peaked interface state feature (on the source side of the molecule) shifts with them, as can be seen in the inset of Figure 5.4(d). The magnitude of that transmission feature diminishes as a function of increasing bias, as the interface states are shifted away from the HOMO; surface Pd d-states become more energetically separated from the molecular HOMO under bias and the hybridization is weaker (see Section 5.2.2)[9].

The model potential profile assumed above is expected to be a reasonable approxima-

---

[9] Notice that this is also why the spin *up* interface state resonances in Chapter 4 for Fe-molecular wires are stronger than those for spin *down*: Spin *up* d-electrons are closer in energy to the molecular HOMO.

tion to the full self-consistent potential profile. Nevertheless, to assess the dependence of the results on this assumed model profile, two additional potential profiles have been studied: one in which all of the bias drops at the two metal-molecule interfaces, and one in which the applied bias drops linearly between the ends of the two Pd contacts (these are the analogues of the potential profiles assumed for Fe quantum point contacts under bias in Chapter 3). Nearly identical transmission characteristics to those in Figure 5.4 emerge in all bias models. This reflects the fact that the wave functions of the interface states lie primarily within the Pd contacts, and so the energy levels of the interface states are pinned to the electrochemical potentials of the contacts, and move rigidly with applied bias. Therefore measurable quantities such as the current and conductance show no significant differences under the different potential profiles up to $2V$. Thus the details of the model potential profile are not crucial to the predictions at moderate bias presented in this thesis.

As explained in Chapter 4, molecular charging under bias is not expected to be significant for the results up to $2V$ presented here; the assumed potential profile that includes the effects of capacitive charging of the electrodes in an averaged sense is expected to be reasonable. This is supported by the robustness of predictions to variations in the model potential profile. The sensitivity of the interface states to charge transfer effects (due to the electronegativity of sulfur) was also investigated (as in Chapter 4) by introducing variations in ΔE. The HOMO resonance was found to be sensitive to such shifts while the energies of interface state resonances were not, being pinned to features in the d-band density of states of the contacts, although the *strength* of the interface state resonances was influenced by such shifts. This is reflected also in the inset of Figure 5.4(d) where the qualitative character of the interface state transmission in unchanged by the applied bias voltage (which mimics the effects of variations in ΔE on the source contact), as noted above. Thus charge transfer effects may influence quantitative results but the qualitative predictions presented here are expected to be robust.

5.4 Negative Differential Resistance in Molecular Wires with Transition Metal Contacts

In his seminal theoretical paper elucidating NDR in mesoscopic junctions, Lang considered a pair of bulk electrodes in contact through a pair of aluminum atoms [155]. The atoms were weakly bonded to the bulk electrodes and their energy levels did not hybridize strongly with the energy bands of the electrodes; thus the transmitting states near the Fermi energy remained sharp. Lang showed [155] that negative differential resistance (NDR) is to be expected when sharp transmitting states of such an atomic chain are resonantly shifted past one another under bias. By contrast, for the Pd/AT4/Pd molecular wire considered here, the predicted sharp transmitting states are due to interface states that form due to *strong* hybridization between molecular sulfur states and Pd d-electron bands; these interface states are located mainly within the contacts (rather than in the wire connecting them as in the system studied by Lang [155]). Nevertheless, as shown in Section 5.3 and analyzed in Appendix E, these sharp transmitting states should also move relative to each other under bias, suggesting that such interface states may also give rise to NDR. The present class of systems, being based on metal-thiol chemistry, should be easier to fabricate and much more robust chemically, and thus better suited to potential applications in nanoelectronic devices.

5.4.1 NDR in Molecular Wires with Symmetric Transition Metal Contact Materials

Appreciable NDR is expected when interface state resonances appear close to the zero bias Fermi energy so that much of the enhancement (as in Figure 5.4(c)) and subsequent decrease of the transmission when interface states are resonantly shifted past one another will occur within the window of integration in Equation (2.1) when calculating the current as a function of bias. Since for the Pd/AT4/Pd system the interface state resonances are not located at E_F (and the enhanced transmission occurs outside of the conduction window, as depicted in Figure 5.5), only a small portion of the resonantly enhanced transmission contributes (off-resonantly) to the current. Therefore, the magnitude of NDR, determined by the maximum peak-to-valley ratio of the current, is in this case quite small. This can be seen in Figure 5.6 where the calculated current for the Pd/AT4/Pd molecular wire is shown

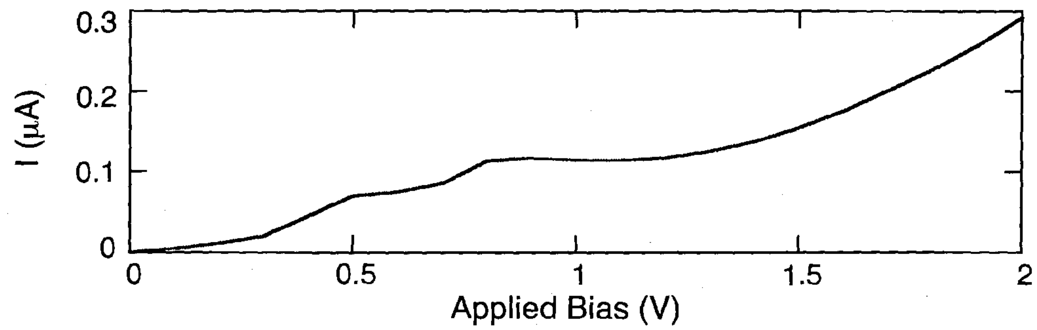

Figure 5.6: Current-voltage characteristic for the Pd/AT4/Pd molecular wire.

as a function of applied bias; this result is obtained from Eqn. (2.1) with $T(E,V)$ as shown in Figure 5.4. Though weak, NDR is present near $1V$.

At low bias the current through the Pd/AT4/Pd wire increases with bias in Figure 5.6 because (as shown in Figure 5.5) the transmission resonance due to the high energy interface state on the source electrode (S_1) is approaching the energy window between the source and drain electro-chemical potentials ($\mu_{S,D}$) in which (according to Equation (2.1)) electron transmission contributes the most effectively to the current. Once the S_1 interface state resonance has fully entered the window, the current begins to plateau until the second transmission feature of the doublet (S_2) approaches and enters the window.

Once S_2 has fully entered the window in Figure 5.5 the current begins to decrease due to the decaying amplitude of the resonance with increasing bias as it continues to separate in energy from the interface state resonances on the drain (D_1 and D_2)[10]. This results in the subtle NDR near $1V$ in Figure 5.6[11]. As the bias increases further, the current begins to increase again because of the increasing width of the window between μ_S and μ_D and the decreasing importance of the interface state transmission resonances relative to the background transmission due to non-resonant tunneling through the AT4 molecule.

Since enhancements and subsequent decreases in the transmission (the crossing of S_2 and D_1 in Figure 5.5) occur outside of the window of integration and contribute only off-resonantly to the current, the full potential NDR via this mechanism will not be realized

---

[10] As can be seen in the inset of Figure 5.4(d), some small but non-negligible overlap remains close to the edge of the window of integration at $0.8V$.

[11] Slightly stronger NDR is predicted for a molecular wire with symmetric *platinum* contacts (as will be displayed in Figure 5.11) as the interface state resonances are stronger than for Pd.

for this system. However it will be shown next that stronger NDR should occur in systems for which interface states form on *opposite* sides of the zero bias Fermi energy and thus can be shifted *into* resonance (within the energy window of integration in Equation (2.1)) by the application of bias. Energetically separated interface state resonances have already been predicted in this thesis for BCC transition metals, where the DOS contains two well resolved maxima on either side of the Fermi energy (see for example spin *down* transmission for Fe-molecular wires in Figure 4.4(a)). However, in all of the considered BCC metal-molecule systems, these interface state resonances are not sharp enough in energy to provide NDR; the mechanism for negative magnetoresistance introduced in Chapter 4 does not require *sharp* interface state transmission resonances.

5.4.2 NDR in Molecular Wires with Asymmetric Transition Metal Contact Materials

The analysis developed in Appendix D for the factorization of the transmission function for an asymmetric insulating molecular wire into functions for two symmetric wires (Eqn. (D.2)) suggests another approach to maximizing NDR via this mechanism based on the integration of *asymmetric* FCC contacts, where the source electrode has DOS maxima *below* the zero bias Fermi energy, as for Pd, while the drain electrode has DOS maxima *above* the Fermi energy (both surface and bulk DOS are again relevant). Substituting a (100) Rhodium electrode for the Pd drain electrode of the Pd/AT4/Pd molecular wire satisfies this criterion [64]: The zero bias transmission probability is shown in Figure 5.7(a) for AT4 bridging symmetric (100) Rh contacts. Here the contacts are again constructed from 54 Rh atoms arranged in a bulk Rh FCC geometry and the equilibrium S-Rh separation is predicted to be 1.82Å [65]; the qualitative predictions are not sensitive to this separation[12]. Near $2eV$ below the Fermi energy, there is weak transmission due to the broadened HOMO, but more importantly, a strong, sharp interface resonance appears just above the Fermi energy. Thus, as displayed in Figure 5.7(b), the *combined* Pd/AT4/Rh system possesses a doubly-peaked interface state on the Pd source side (labeled Pd_1 and Pd_2) below the zero bias Fermi energy

---

[12] If a Rh-S separation of 2Å is assumed, the transmission (and resulting current calculations) are not significantly affected. In fact, for 2Å separation, the interface state resonance occurs closer to the Fermi energy causing an earlier onset of NDR for the following system. It is only slightly diminished in magnitude.

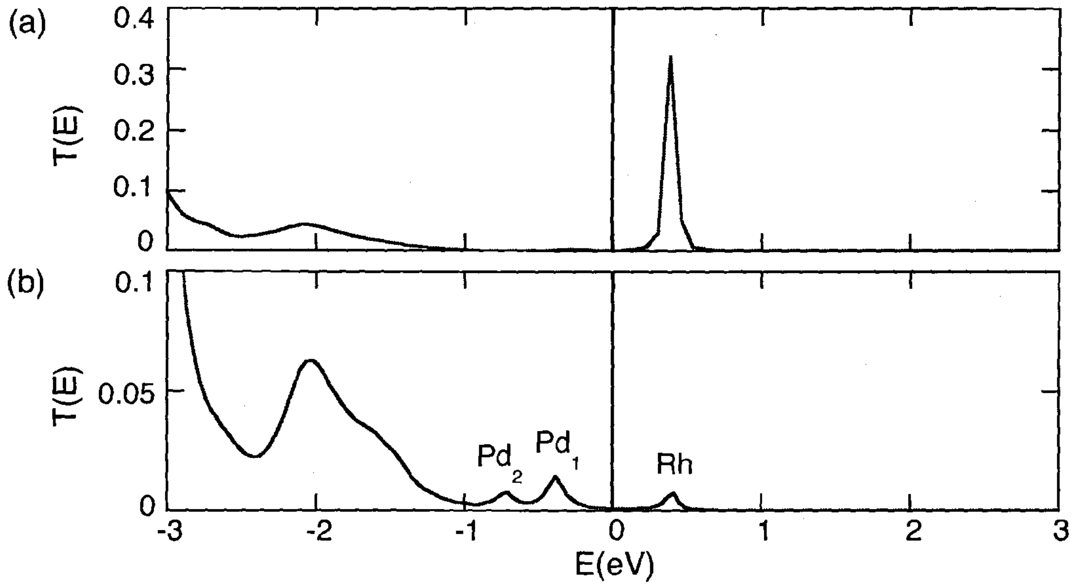

Figure 5.7: Transmission probabilities for molecular wires with Rh contacts. (a) Zero bias transmission probability for a symmetric Rh/AT4/Rh molecular wire. (b) Transmission probability for the Pd/AT4/Rh molecular wire.

and an interface state on the Rh drain side (labeled *Rh*) which is above the Fermi energy[13]. The interface state resonances are weaker in Figure 5.7(b) than in either Figure 5.4(a) or 5.7(a) as interface states form only on one side of the molecular junction at a particular energy.

The effect of applied bias (employing the assumed potential profile discussed in Section 5.3) on the interface state resonances in Figure 5.7(b) for the Pd/AT4/Rh molecular wire is

---

[13] Since the work functions of Pd and Rh are different, once AT4 has bridged the leads, a current will flow (at zero bias) between to two contacts until an equilibrium Fermi energy has been established, creating an electric field in the vicinity of the molecule. This electric field (or *contact potential* [168]) is treated in an similar way to that created by application of bias, where the molecular energy levels are shifted under the assumed potential profile, as discussed in Section 5.3. Calculations have been carried out for other choices of the model potential profile arising from the difference in work function between Rh and Pd with almost identical results. The reason for this insensitivity to the details of the potential profile is that the interface states that mediate transport in this system are located mainly within the metal contacts while the insulating AT4 molecule behaves qualitatively like a simple potential barrier; thus neither is sensitive to the *details* of how the electrostatic potential drops between the metal contacts.

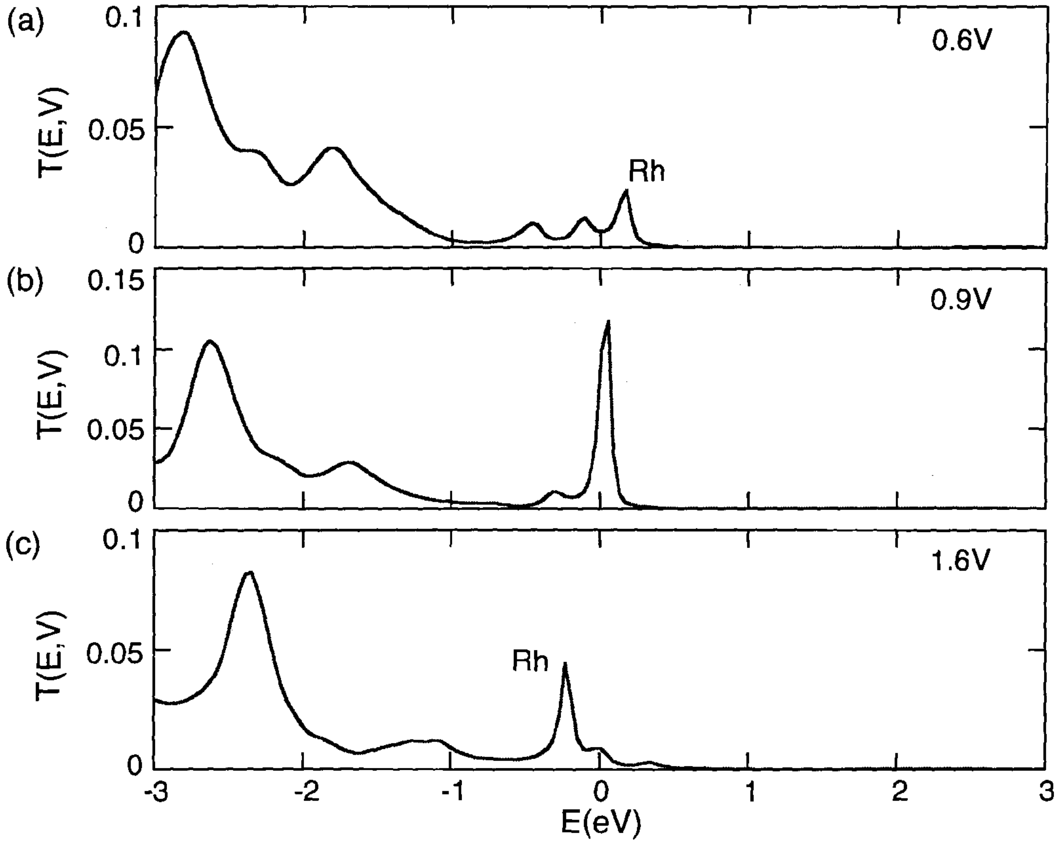

Figure 5.8: Transmission probabilities as different bias is applied across the Pd/AT4/Rh molecular wire. (a) Transmission probability vs. energy at 0.6V. (b) 0.9V bias. (c) 1.6V.

clearly demonstrated in Figure 5.8, where the transmission probability for increasing bias voltage applied to the Rh contact is plotted. (Forward bias is defined as the bias that causes electrons to flow from the source Pd electrode to the drain Rh electrode, i.e., with the Rh contact at a positive electrostatic potential relative to the Pd.) As the magnitude of the bias increases, the electrostatic potential energy of electrons on the Rh electrode decreases while that of electrons on the Pd electrode increases. Therefore, since the interface state responsible for the transmission resonance that is above the Fermi level (*Rh* in Figure 5.7(b)) is located predominantly at the Rh electrode, the energy of that resonance decreases with increasing bias. Similarly the energy of the interface state transmission resonances that are below the Fermi level (Pd_1 and Pd_2 in Figure 5.7(b)) increase with increasing bias because those states are located at the Pd electrode. Hence, in Figure 5.8(a) for $0.6V$ applied bias,

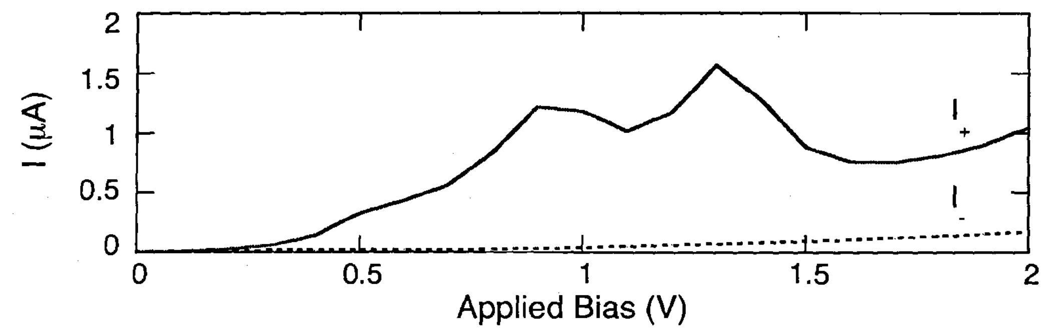

Figure 5.9: Currents for the Pd/AT4/Rh molecular wire. Solid curve is current for forward bias, dashed curve is magnitude of current for reverse bias, $|I_-|$. Forward bias induces a net electron flux in the direction from the Pd source electrode to the Rh drain electrode.

the separation between the energies of the interface states on the Pd and Rh contacts has decreased relative to that in Figure 5.7(b). At an applied bias of 0.9V (Figure 5.8(b)), the interface state Pd_1 shifts into resonance with the Rh state (the resonantly transmitting state has strong contributions at *both* metal-molecule interfaces) and the transmission is greatly enhanced (note also the change in y-axis scale). At 1.6V, the Rh interface state has shifted past both Pd states and the transmission has weakened.

The predicted currents for the Pd/AT4/Rh molecular wire are shown in Figure 5.9. As suggested by the weakening of the transmission in Figure 5.8(c), pronounced NDR is apparent in the forward bias direction (solid curve in Figure 5.9) near 1.1V and 1.6V. ($I(-V) \neq -I(V)$ as the system is not mirror symmetric.) The two occurrences of NDR are related to the double-peaked interface state transmission feature (Pd_1 and Pd_2) in Figure 5.7(b): The sharp Rh interface state resonance above the Fermi energy in Figure 5.7(b) scans through both Pd interface transmission resonances, as depicted in Figure 5.10, crossing the high (Pd_1) and low (Pd_2) energy Pd interface states resonances near 0.9V (corresponding to the enhanced transmission in Figure 5.8(b)) and 1.4V, respectively. The *decrease* in current with *increasing* voltage (i.e., NDR) seen above the current peaks in Figure 5.9 is due to the overall weakening of the resonant transmission as the energies of the transmitting interface states separate with further increase of bias voltage (as in Fig. 5.8(c)). Thus there are two enhancements and subsequent decreases in the transmission within the window of integration between μ_S and μ_D in Figure 5.10, corresponding to the

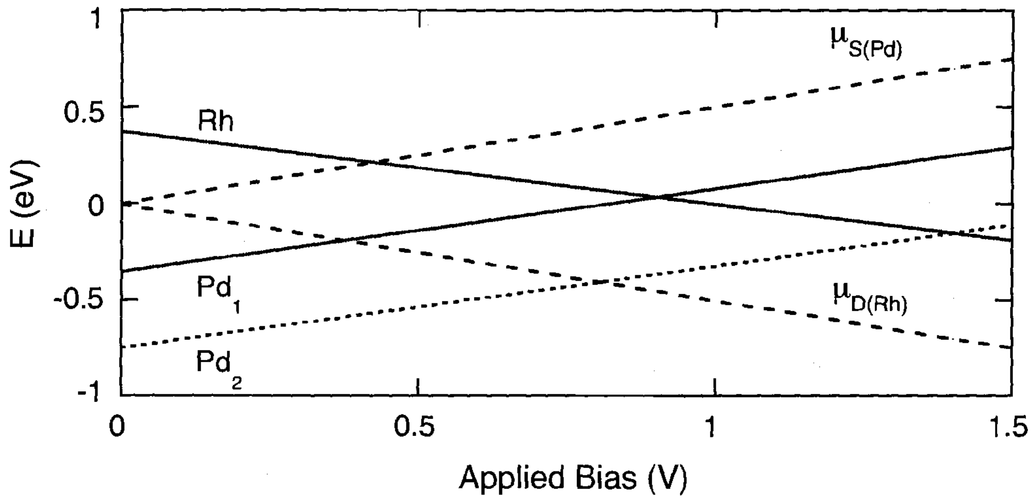

Figure 5.10: Energies of interface state resonances (solid and dotted lines) and electrode electrochemical potentials (dashed) labeled according to the respective electrode vs. (forward) bias applied across the Pd/AT4/Rh molecular wire. 1(2) stands for the high (low) energy Pd interface state.

two peaks and valleys in the current in Figure 5.9.

The predicted significant NDR for Pd/AT4/Rh suggests potential avenues for controlling negative differential resistance in molecular wires: Though the qualitative predictions are robust, quantitative current-voltage characteristics, and values of NDR, are dependent on the interface properties of the molecular junction. This is demonstrated in Figures 5.11(a,b) which display the current-voltage characteristics for AT4 bridging asymmetric Pd and Rh contacts with (111) surface orientations where the molecular sulfur atoms chemisorb at HCP and FCC sites, respectively. Due to the strength of the AT4-Pd (111) interface state resonance shown in Figure 5.3(a) for the HCP binding configuration, the predicted NDR in Figure 5.11(a) is also quite strong for the HCP adsorption site. It is weaker for the case of FCC site binding (Figure 5.11(b)). Since the geometry and interface properties in general depend on how samples are fabricated, these results suggest that improved control over sample preparation may offer further control over NDR transport phenomena.

The NDR can also be tailored by choosing different transition metals for the contacts. For example, similar calculations performed in the course of the present research predict that if the Pd (111) electrode is replaced with Pt (111), the onset of NDR should occur at

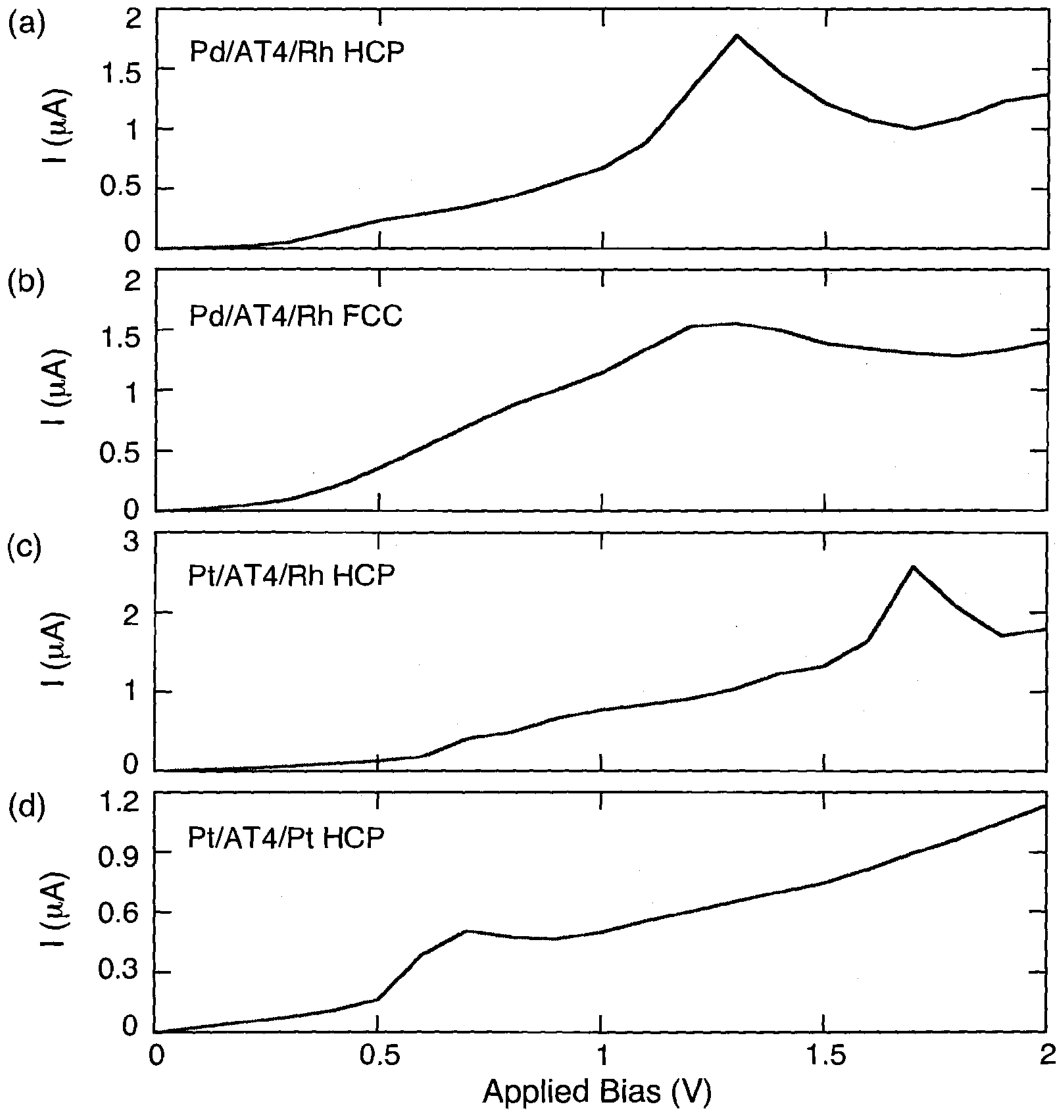

Figure 5.11: Calculated $I(V)$ for molecular wires with (111) metal contacts. Pd/AT4/Rh molecular wire with (a) HCP site adsorption. (b) FCC site adsorption. (c) Pt/AT4/Rh wire with HCP site binding. (d) Symmetric Pt/AT4/Pt junction with HCP site binding.

higher bias, as in Figure 5.11(c). As displayed in Figure 5.11(d), relatively strong NDR may also occur at earlier bias if *symmetric* Pt (111) contacts are bridged by AT4. The mechanism is similar to that depicted in Figure 5.5 for symmetric Pd contacts, but here the interface state resonances are stronger, singly peaked and located slightly closer in energy to E_F, thus the NDR is stronger and occurs earlier. These results suggest for the first time that it may be feasible to *design* the non-linear current-voltage characteristics (NDR) of molecular nanoelectronic devices by appropriate choices of the specific transition metals used for the contacts and their crystallographic orientations.

Also, since transmission enhancements due to interface states on the source electrode shifting into resonance with interface states on the drain do not involve any structural rearrangement of the molecule or contacts, this mechanism for NDR is not expected to be accompanied by hysteresis. Since hysteresis has been found experimentally in many metal/molecule/metal devices exhibiting NDR to date, *lack* of hysteresis accompanying the NDR in a molecular device (in which d-electron interface states are expected) should be an important experimental characteristic of the NDR mechanism that has been identified here.

It is clear that because this NDR mechanism requires the relative shifting of interface states on the source (Pd) upwards in energy and into resonance with interface states on the drain (Rh), NDR will only occur for one direction of applied bias. In fact, in the reverse direction of bias, no significant transmission features enter the window of integration and the current is weak as displayed by the dashed curve in Figure 5.7(c) ($|I_-|$ vs. $|V|$ is plotted in the same quadrant as positive bias for easy comparison). Therefore, the Pd/AT4/Rh molecular wire is predicted to also act as a rectifier, yielding appreciable rectification.

5.5 Rectification in Molecular Wires with Transition Metal Contacts

To explore molecular rectification further, the possibility of rectification when molecules form a bridge between Pd and Au contacts will now be investigated. (100) surface orientations are considered; very similar results are found for other surface orientations and binding sites. The Au-S separation is taken to be 2Å, as predicted with density functional calculations [65], where the sulfur adsorbs above a four-fold Au hollow site.

The transmission, and currents for both directions of bias, for a Pd/AT4/Au molecular wire are shown in Figure 5.12. The double-peaked interface state transmission resonances below the Fermi energy in Figure 5.12(a) are weaker than those in Figure 5.4(a) as interface states form there only on one (the Pd) contact for the Pd/AT4/Au system; as alluded to

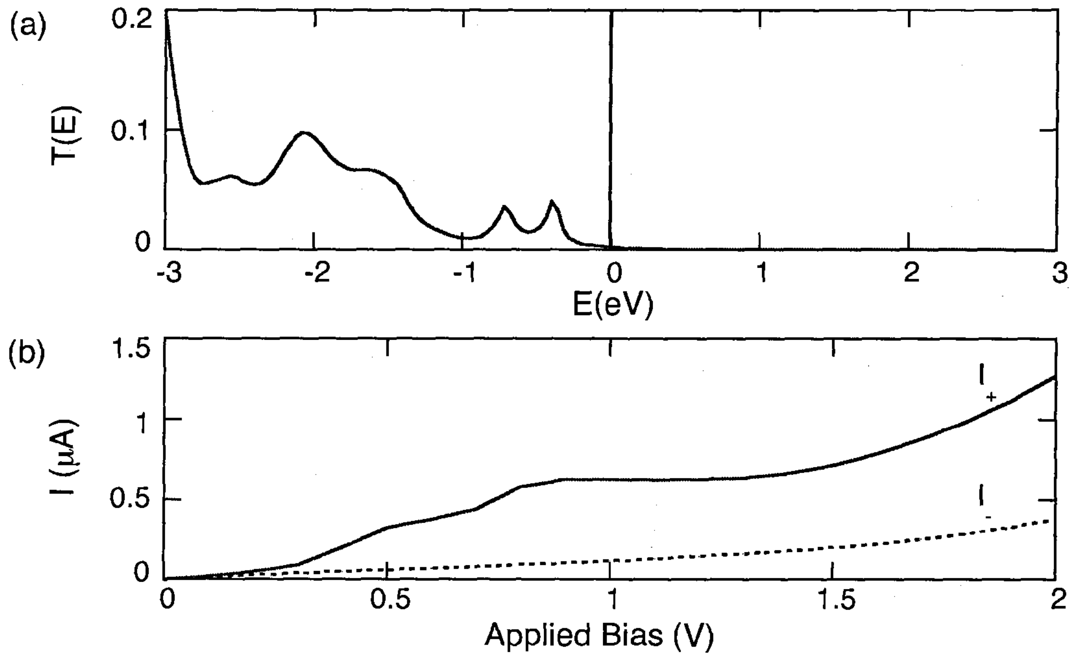

Figure 5.12: Currents displaying rectification. (a) Transmission probability at zero bias for a Pd/AT4/Au molecular wire. (b) $I(V)$ for Pd/AT4/Au molecular wire. Solid curve is current for forward bias, dashed curve for reverse bias. Forward bias induces a net electron flux in the direction from the Pd source electrode to the Au drain electrode.

earlier, interface states do not form near the Fermi energy on the Au contact. The solid curve of Figure 5.12(b) is the current for the forward bias direction, I_+ (i.e., positive bias applied to the Au contact); the dashed curve is the current for the reverse direction, $|I_-|$. As can be seen I_+ saturates near $1V$, once both Pd interface transmission features in Figure 5.12(a) have completely entered the window of integration. The current profile for forward bias is quite similar to that predicted for Pd/AT4/Pd (Figure 5.6) because the latter current is dominated by resonant transmission from interface states on the source once they enter the window of integration (as in Figure 5.5 for S_1 and S_2), which are also present for Pd/AT4/Au (Figure 5.12(a)), and is only weakly modified by off-resonant transmission tails of interface states on the Pd/AT4/Pd drain electrode, that are not present for Pd/AT4/Au. However there is no appreciable NDR for Pd/AT4/Au.

In the reverse bias direction (dashed curve in Figure 5.12(b)), no appreciable transmission features enter the window of integration; the interface state resonances shift with the electrochemical potentials of the Pd contact and remain outside of the current window (as in Figure 5.5 for D_1 and D_2), while no significant resonant transmission features are present near the Fermi energy on the Au contact. Therefore, an appreciable rectification ratio ($I_+/|I_-|$) is predicted, reaching a value of roughly 6 near the $1V$ saturation bias.

An asymmetric molecular wire system is necessary for a rectifying current-voltage characteristic. However, since the rectification in the present system emerges from interface states forming on the S-Pd contact and the lack of interface states on the S-Au contact, increasing the asymmetry by switching to a molecule with a *single* thiol does *not* drastically increase the rectification, provided that the thiol bonds to the Pd contact[14]. In fact quite similar current-voltage characteristics to those in Figure 5.12(b) are predicted for Pd/butyl-thiolate/Au, up to a scaled decrease in the magnitudes of both forward and reverse currents due to the lack of strong bonding at the Au interface. Similar rectification is predicted for *symmetric* Pd leads bridged with an asymmetric molecule such as butyl-thiolate where significant interface states also form only on *one* side of the junction.

Hence, interface states can provide rectification in such asymmetric systems: Resonances associated with interface states close to the zero bias Fermi energy shift rigidly (pinned to one contact) with bias but occur only on one side of molecule, either because only one contact is bonded to the molecule or because no d-states are present near the Fermi energy for one of the electrodes. Therefore, interface state resonances will enter the current window in Eqn. (2.1) only in one direction of applied bias.

5.6 Conclusions

Calculations were presented that indicate interface states in molecular wires should play a non-trivial role in transport when d-electron orbitals of the metal electrodes make a significant contribution to the density of states of the metal near the Fermi energy. As an example, butyl-dithiolate bridging Pd contacts was considered in detail and it was determined that electron transmission through the junction at moderate bias is dominated by interface states resulting from the strong chemical bonding between the thiolated ends of the molecule and the Pd d-orbitals. Resonant enhancements and reductions in the transmission due to in-

---

[14] No significant rectification is expected if thiols bond only to the Au contact. In this case, interface states are not expected to be significant.

terface states were predicted to occur when a bias voltage is applied across the junction. This was shown to result in non-linear transport phenomena including negative differential resistance and rectification, even for such simple molecules as alkane-thiols. Potential avenues for tailoring these non-linear transport phenomena were also considered by replacing one Pd electrode with other transition metals: Integration of a Rh electrode was predicted to yield both strongly enhanced NDR and rectification. The strength of the NDR and the range of bias voltage in which it occurs were found to depend strongly on both the specific transition metals used as electrodes and their crystallographic orientations. These findings raise the prospect of designing the NDR of molecular wires for nanoelectronic device applications by appropriate choice of transition metal electrodes and their surface structures.

It is reasonable to expect the *qualitative* prediction that NDR should occur in Pd/AT4/Rh (and Pt/AT4/Rh) systems to be model-independent for the following reasons: The Pd electrode has its d-orbital density of states maxima *below* the zero bias Fermi energy, while the Rh electrode has its d-orbital density of states maxima *above* the Fermi energy [64]. Since the interface states are located primarily in the contacts and have transition metal d-orbitals character there, their energies are pinned to the maxima of the Rh and Pd d-orbital densities of states. Therefore the strong difference between the d-electronic structures of Rh and Pd must result in the interface states on the Rh and Pd electrodes occurring at well-separated energies at zero bias. Furthermore since these interface states are each confined mainly to *one* electrode, when a bias is applied across the junction the energies of these interface states must follow the electrochemical potentials of their respective electrodes. Therefore if the bias is increased sufficiently (with the appropriate sign) the interface state energies must cross resulting in enhancement followed by weakening of the transmission and hence NDR. These qualitative considerations should hold for any realistic model of this system, and therefore the prediction that NDR should occur in this system is expected to be robust.

Chapter 6

Spin Current Rectification in Molecular Wires

6.1 Introduction

As illustrated in Chapter 5, spatial asymmetries that manifest as asymmetries in the electronic characteristics of a molecular wire may produce rectification of electric current ($I(-V) \neq -I(V)$). Positive or negative bias voltages applied across the two terminals of the asymmetric device give rise to electronic eigenstates that contribute differently to the current causing the asymmetry under bias inversion. Such spatial asymmetry, and therefore rectification, may result from the use of spatially asymmetric molecules, different materials for source and drain electrodes, asymmetric molecule-lead binding, or a combination of all three [1, 22, 23, 32, 50, 157, 158, 159, 160, 161].

As with the electronic (charge) current, spatial asymmetry in a molecular wire with one or more *magnetic* electrodes may result in the net *spin* current, I_S, being asymmetric under bias inversion. However, although there have been several theoretical studies of spin transport through molecular wires [38, 39, 40, 41, 42, 43, 44], the possibility of spin current rectification in such systems has not been explored. This topic is addressed in the present chapter.

While thermodynamics requires the electronic current to *reverse* direction when the bias is reversed, there is no such requirement for the spin current. Therefore it is proposed here that spin current rectification of two kinds should be possible in principle in spatially asymmetric systems:

(1) *Weak* spin current rectification where the direction of the spin current reverses and the magnitude of the spin current changes when the applied bias is reversed; this is the spin analog of charge current rectification.

(2) *Strong* spin current rectification where the direction of the spin current remains *unchanged* when the applied bias is reversed. This effect has no charge current analog.

The possibility of spin current rectification occurring in specific asymmetric molecular wires is explored theoretically in this chapter. It will be predicted that both *weak* and *strong* spin current rectification should be realized in practice, depending on the details of the system and the magnitude of the applied bias voltage [51].

As with charge current rectification, spin current rectification is a *non-linear* transport phenomenon; at infinitesimal bias (in the linear response regime) no rectification is possible. *Weak* spin current rectification becomes possible in asymmetric magnetic wires as the system exits the linear response regime with increasing bias, and *strong* spin current rectification is predicted to be attainable in some systems at still higher bias. Therefore the predictions summarized above regarding the nature of spin current rectification are relevant to asymmetric junctions that can sustain a significant bias voltage, such as molecular and nanoscale atomic junctions and metal/insulator/metal thin-film systems[1].

Because weak spin rectification is closely tied to current rectification, these findings demonstrate that it should be possible to design molecular electronic devices that *simultaneously* function as current rectifiers and spin rectifiers, thereby providing such molecular wires with dual functionality based on the transport of both charge and spin. Such functionality may ultimately allow both logic and memory to be implemented with a single device, and the design of such a device based on molecules may allow for its construction using the smallest possible circuit elements.

In the following section, the formalism, analysis and general understanding of molecular wires with transition metal electrodes, developed in the preceding chapters, are applied to asymmetric wires where a single octane-thiolate (OT) or octane-dithiolate (ODT) molecule bridges the gap between Au or Pd and ferromagnetic Fe electrodes. These molec-

---

[1] Experimental work has demonstrated a variety of molecular wires to support applied bias voltages in excess of 1 Volt without breaking down; see for example Refs. [4, 169]

ular wires are predicted to function as current and spin current rectifiers, and to exhibit both *weak* and *strong* spin current rectification, depending on the value of the applied bias. In Section 6.3, a junction in which an OT molecule bridges Au and Ni electrodes is considered. Less pronounced charge and spin current rectification effects are predicted for this system than in the corresponding one with an Fe contact.

Spin-flip processes are not considered, consistent with weak spin-orbit interaction in molecules and the high degree of spin polarization retained in observations of spin-dependent transport in molecular wires [45, 46, 47]; transmissions and currents (Eqn. (2.1)) are calculated independently for spin *up* ($I_\uparrow(V)$) and *down* ($I_\downarrow(V)$) electrons. The total current through the molecular device is given by the sum of the currents for the separate spin channels, $I(V) = I_\uparrow(V) + I_\downarrow(V)$, while the net spin (angular momentum) current is defined as

$$I_S(V) = \frac{\hbar}{2e}(I_\downarrow(V) - I_\uparrow(V)). \tag{6.1}$$

6.2 Spin Current Rectification in Molecular Wires with Fe Contacts

6.2.1 Au/OT/Fe Molecular Wires

The extended molecule for the Au/OT/Fe molecular wire is shown in Figure 6.1. Each metallic cluster of the extended molecule is built from $5\times5, 4\times4, 3\times3, 2\times2$ (100)-oriented layers (54 atoms total) of atoms in the bulk geometry of the metal. The sulfur atom is estimated to sit 2Å above the four-fold FCC Au hollow site [65], while the BCC Fe electrode surface is estimated to be 4.1Å from the molecular carbon atom[2]. Such molecular junction geometries may be realized with STM or break junction systems where the Fe-C distance may vary. However, while the magnitudes of the currents depend exponentially on the Fe-C separation, the qualitative transmission features and ratios of currents are insensitive to the separation for a wide range of values. The qualitative predictions are also not overly sensitive to the metal-S distance.

The electronic structure of the molecular wires with asymmetric contacts studied in this chapter is described by the hybrid semi-empirical tight-binding model of Section 2.6. When

---

[2] This estimate is based on a geometry relaxation of a *Ni* surface over OT.

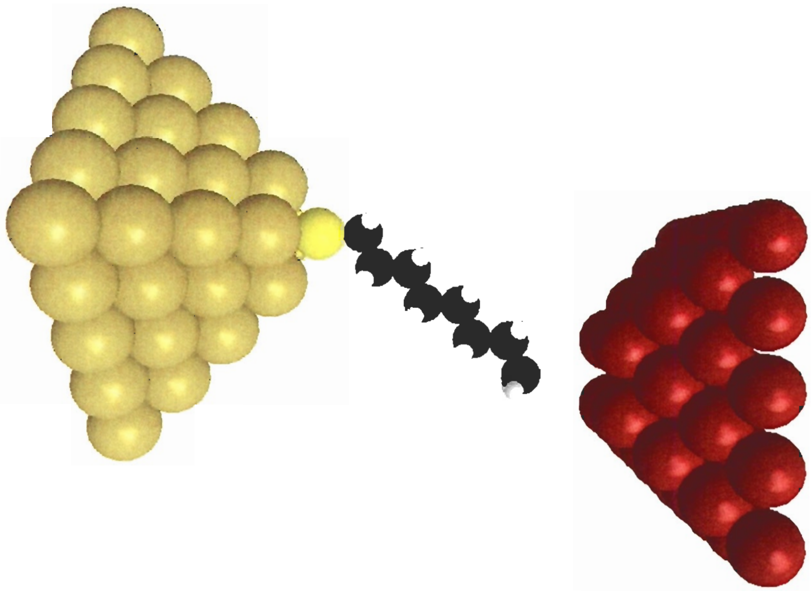

Figure 6.1: Extended molecule for an Au/OT/Fe molecular wire. Each metal cluster consists of 54 atoms that coincide with sites of (100) crystal lattices.

different metals are used for the two electrodes of the molecular device, their differing work functions give rise to electrostatic fields between the electrodes even if no bias is applied across the device. This *contact potential*-related field [168] is included approximately in the model: It is treated in an similar way to that created by application of bias (discussed below), but with the molecular atomic site energies being shifted according to a linear potential profile.

Rectification of electronic current is attainable only under the application of significant bias. Most of the molecular bridges considered in this chapter are monothiolates; for these systems a substantial spatial gap is predicted at the interface between the metal contact and the non-thiolated molecular end (in contrast to the relatively small separations predicted for dithiolated molecules in the previous chapters). In the numerical results presented here for these systems, for simplicity, it is assumed that half of the applied bias drops at this interface and half drops across the molecule (see Section 4.4). The predictions regarding the *strong* and *weak* spin current rectification regimes do not change qualitatively if other model potential profiles are adopted.

The calculated transmission probabilities at zero bias for spin *up* (u) and *down* (d) electrons are displayed in Figure 6.2(a) for the Au/OT/Fe wire; the common Fermi level of the metal contacts is at $0eV$. The mechanisms that give rise to the resonant transmission features that are visible near $-1eV$ and $0.8eV$ at zero bias in Figure 6.2(a) control both the charge current I (Figure 6.3(a)) and the spin current I_S (Figure 6.3(b)) at moderate bias. These mechanisms involve interactions of the molecule with both metal interfaces; to understand them it is helpful to examine the roles of the two different metal-molecule interfaces separately (i.e., by way of Eqn. (D.2)). This is accomplished by considering a pair of closely related *symmetric* molecular wire systems, Au/octane-dithiolate/Au and Fe/octane/Fe. In the former system both metal-molecule interfaces are similar to the Au/molecule interface of Au/OT/Fe while in the latter both are similar to the Fe/molecule interface of Au/OT/Fe[3]. The calculated zero bias transmission probabilities for these two symmetric systems are plotted in Figure 6.2(b) and Figure 6.2(c) respectively; for the Fe/octane/Fe system parallel magnetization of the two Fe electrodes is assumed and both the spin *up* and spin *down* electron transmission probabilities are shown. Since the transmission features due to the interaction of the molecule with the source and drain interfaces are degenerate at zero bias for spatially symmetric wires, the analysis of the transmission probabilities in Figures 6.2(b,c) is more straight forward than of those in Figure 6.2(a):

For the symmetric Au/ODT/Au junction, the weak transmission resonance near $-1.5eV$ in Figure 6.2(b) is due to resonant conduction through the molecular HOMO. The conduction is weak because the HOMO is localized mainly at and near the sulfur atoms and decays rapidly along the molecule's carbon backbone. The transmission probability decreases towards the Fermi energy where it is due to off-resonant conduction via the tail of the HOMO resonance. The large transmission below the HOMO resonance is due to molecular conducting states lower in energy, including the HOMO-1. The lowest unoccupied molecular orbital (LUMO) is located above the plotted energy range due to the large molecular HOMO-LUMO gap and does not contribute significantly to the current for any of the results presented here. Due to the resonant conduction through the HOMO and its off-resonant

---

[3] The geometries of the symmetric junctions are obtained by geometrically mirroring the asymmetric Au/OT/Fe junction to the left and to the right without further geometry relaxations. The Fermi energy alignment of the contacts is the same in all three model systems, using that of the Au/OT/Fe wire as the reference, as required by Eqn. (D.2).

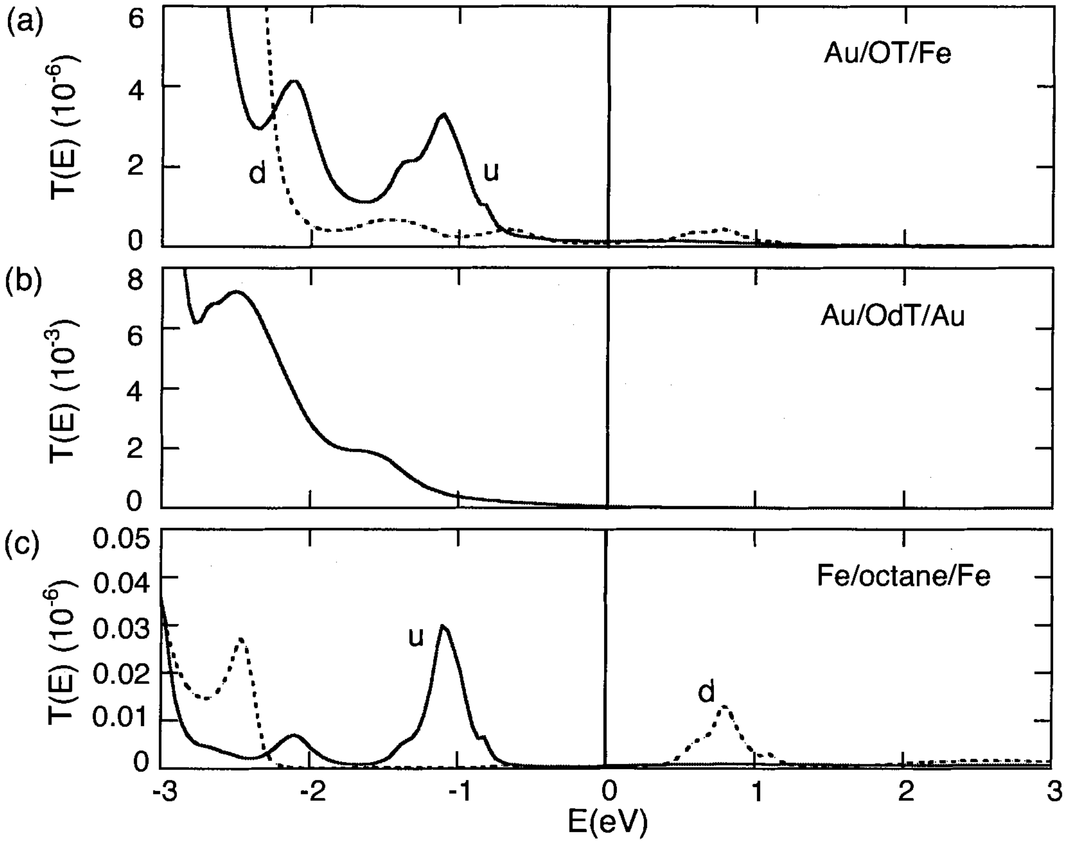

Figure 6.2: Transmission probabilities vs. energy at zero bias for (a) Spin *up* (u) and spin *down* (d) electrons for the Au/OT/Fe molecular wire. Fermi energy= $0eV$. (b) An Au/ODT/Au junction. (c) An Fe/octane/Fe junction.

transmission near the Fermi energy, the transmission probability for Au/ODT/Au is very asymmetric about the Fermi energy ($E_F = 0eV$). Nevertheless, for a *spatially* symmetric junction, $I(-V) = -I(V)$ and rectification is prohibited. However, the asymmetry of $T(E)$ about E_F for the Au/molecule contact can result in strong rectification when this contact forms part of an *asymmetric* molecular wire (as for Au/OT/Fe) and the total transmission at the second contact is symmetric about E_F.

Such is nearly the case for the Fe contact, as is displayed in Figure 6.2(c) (while the total transmission $T(E) = T_\uparrow(E) + T_\downarrow(E)$ is asymmetric about the Fermi energy, with the magnitudes of the u and d transmission peaks differing by roughly a factor of 2, it is much less so than $T(E)$ in Figure 6.2(b)). As is the density of states for bulk Fe [64] (see Figure

3.1), the transmission features in Figure 6.2(c) are highly spin split: The transmission features near $1eV$ below E_F for spin *up* and $0.8eV$ above E_F for spin *down* in Figure 6.2(c) are due to Fe metal states. They are present even in the *absence* of molecules (as reported in Figure 3.10(a) for vacuum tunneling between Fe nanocontacts); since no strong hybridization occurs between the octane molecule and either Fe contact, the main role of the octane is to effectively lower the barrier for conduction (relative to vacuum) in the Fe/octane/Fe wire.

The origin and qualitative characteristics of the important features in the transmission of the asymmetric Au/OT/Fe molecular wire seen in Figure 6.2(a) are now readily understood as manifestations of consecutive transmission of electrons through the Au/OT and OT/Fe interfaces: The prominent spin *up* transmission feature in Figure 6.2(a) around $-1eV$ is due to the peak in the spin *up* transmission between the Fe and the molecule in this energy range (Fig. 6.2(c)) coinciding with the molecular HOMO-mediated transmission at the Au/OT interface (Fig. 6.2(b)). The much weaker spin *down* transmission feature around $0.8eV$ in Figure 6.2(a) is due to the corresponding peak in the spin *down* transmission between the Fe and the molecule (Fig. 6.2(c)) occurring in an energy range where there is no transmission resonance associated with the Au/OT interface. The similarly weak spin *down* transmission around $-1eV$ in Figure 6.2(a) is due to weak spin *down* transmission at the OT/Fe interface coinciding with the (broad) molecular HOMO-mediated transmission resonance associated with the Au/OT interface.

The total charge current, $I(V) = I_{\uparrow}(V) + I_{\downarrow}(V)$, displayed in Figure 6.3(a) as a function of applied bias voltage V is calculated according to the Landauer expression, Equation (2.1) from the bias-dependent transmission probability $T(E,V)$. The latter quantity differs from $T(E,0)$ that is plotted in Figure 6.2(a) in that $T(E,V)$ includes the effects of the bias voltage on the energies of the electronic states within the metal contacts as well as on the potential profile of the molecular junction. However, the behavior of the current can still be understood qualitatively in terms of electron transmission through the two molecule-metal interfaces discussed above if their bias-dependence is taken into consideration (i.e., in the spirit of Eqn. (D.4)): With increasing positive bias (applied to the Fe electrode) the transmission features due to the molecular HOMO levels that are associated with the Au/molecule interface (Figure 6.2(b)) move to higher energies relative to the the transmission features due to the Fe/molecule interface (Figure 6.2(c)). This results in an overall

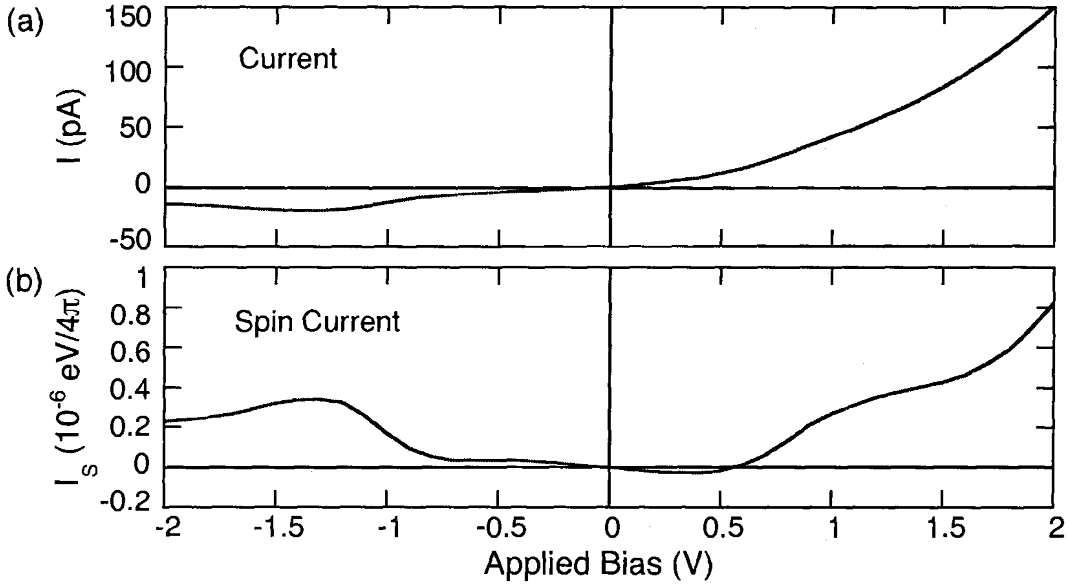

Figure 6.3: Currents exhibiting rectification for the Au/OT/Fe wire. (a) Calculated current vs. voltage. (b) Calculated net spin *down* current given by Equation (6.1) vs. voltage.

enhancement of $T(E,V)$ relative to $T(E,0)$ within the window of conduction between the electrochemical potentials of the source and drain electrodes, defined by Equation (2.1). By contrast, for negative applied bias the transmission features due to the Au/molecule interface (Figure 6.2(b)) move to lower energies and remain *outside* the window of conduction, resulting in an overall weakening of $T(E,V)$. Thus the magnitude of the current, I, at positive bias is markedly larger than that at negative bias, so that the Au/OT/Fe molecular wire behaves as a charge current rectifier as is evident in Figure 6.3(a).

The net spin current given by Equation (6.1) is displayed in Figure 6.3(b). As expected from the general considerations discussed above, there is a linear response regime at low bias (in this case for $|V|$ below approximately $0.4V$) where there is no appreciable spin current rectification, followed by (for $|V|$ below approximately $0.6V$) the onset of appreciable non-linearity with an associated *weak* spin current rectification regime where $I_S(V) \neq -I_S(-V)$ although $I_S(V)$ and $I_S(-V)$ have opposite signs. However at still larger bias, the calculation predicts a qualitative change in the nature of the spin current rectification: The net spin current is positive for *both* directions of applied bias voltage over a substantial voltage range beginning near $\pm 0.6V$, i.e., *strong* spin current rectification is predicted. This is due to the asymmetry about the Fe Fermi level of the spin *up* and spin *down* transmission resonances associated with the Fe/molecule interface that is evident also in Figure 6.2(c). For positive bias applied on the Fe contact, the transmission is dominated by the transport of spin *down* electrons through the molecule from the Au into unoccupied states of the Fe contact that are predominantly spin *down*. For similarly large negative bias, the transport is dominated by spin *up* electrons as the occupied states on the Fe contact are predominantly spin *up*. Therefore, for either direction of bias, the net spin *down* electron flux is towards the Fe contact.

6.2.2 Au/ODT/Fe and Pd/OT/Fe Molecular Wires

Calculations for an Au/octane-*di*thiolate(ODT)/Fe molecular wire predict that this system should also function as a *strong* spin current rectifier comparable to Au/OT/Fe. The mechanisms involved are, however, somewhat different for the two systems: Whereas the spin rectification in the Au/OT/Fe system arises from spin-split Fe metallic states at the non-thiolated Fe interface (as in Figure 6.2(c)), *both* contacts are thiol-bonded for Au/ODT/Fe. In this case, the low bias transmission on the Fe contact is dominated by *interface states* at the sulfur-Fe interface (see Figure 4.7(a)) that are also spin-split and occur on opposite sides of the Fe Fermi energy.

Calculations also predict similar spin rectification to that in Figure 6.2(b) if the Au electrode is replaced with Pd. Here, due to the strong hybridization that occurs between the molecular sulfur atom and the *d*-electronic states of the Pd contact (as elucidated in Chapter 5; see Figure 5.1), the moderate bias transmission on the Pd/molecule contact is dominated by interface states that develop within the HOMO-LUMO gap [50]. They are located near the HOMO (below the Fermi energy) and as a result the transmission at the Pd/molecule contact is even more asymmetric about the zero bias Fermi energy than the transmission due to the Au/molecule contact (Figure 6.2(c)).

The calculated total current, I, for the Pd/OT/Fe molecular wire is displayed in Figure 6.4(a). Due to the large transmission asymmetry at the Pd/molecule contact, the current exhibits stronger charge current rectification (the current is more asymmetric under inversion of bias) than that displayed in Figure 6.3(a) for the Au/OT/Fe junction. Also, as is evident from the calculated spin current, I_S, plotted in Figure 6.4(b), the Pd/OT/Fe wire possesses

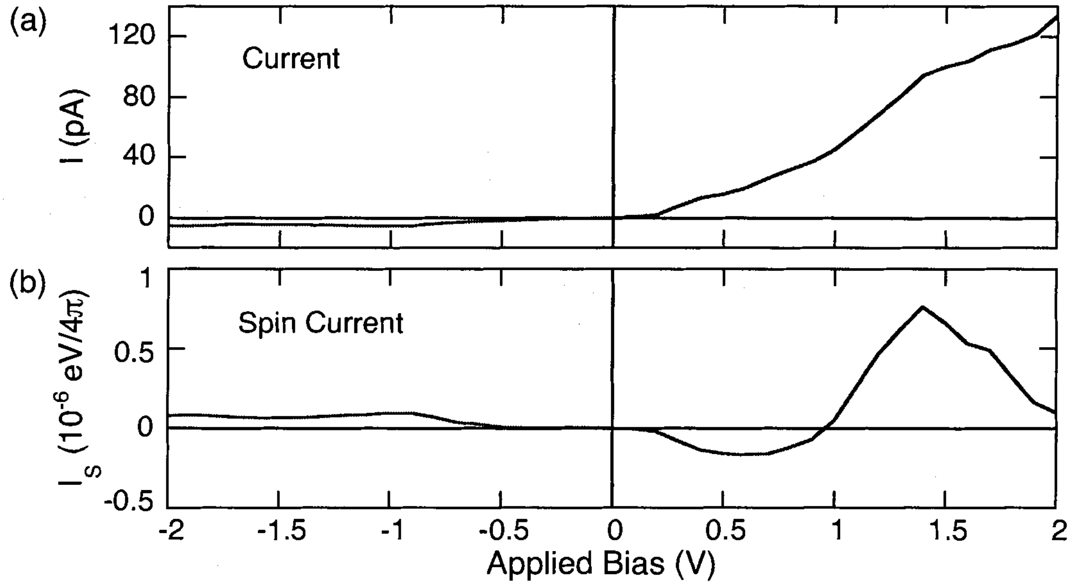

Figure 6.4: Currents exhibiting rectification for the Pd/OT/Fe molecular wire. (a) Calculated charge current-voltage characteristic. (b) Net spin current vs. voltage.

significant *weak* spin rectification beginning for $|V|$ above $0.2V$ and extending to applied biases of $\pm 1V$. Since the transmission at the molecule/Fe contact is unchanged, the *strong* spin current rectification for $|V|$ above $1V$ in Figure 6.4(b) is qualitatively similar to that in Figure 6.3(b).

6.3 Spin Current Rectification in Molecular Wires with Ni Contacts: Au/OT/Ni

Figure 6.5 shows the predicted currents for an Au/OT/Ni molecular wire[4] (with (100) surface orientations). In this case the transmission probabilities for Ni/octane/Ni displayed in Figure 4.10(b) serve to clarify the nature of the transmission at the Ni/molecule interface; Figure 6.2(b) relates to the Au/molecule interface for the Au/OT/Ni system as well.

Since the Ni/molecule transmission resonances are located below the Fermi energy for *both* spin *up* (u) and *down* (d) electrons in Figure 4.10(b), in contrast to the Fe/molecule

---

[4] The Ni-C separation is the same as the Fe-C separation considered in the Section 6.2.1.

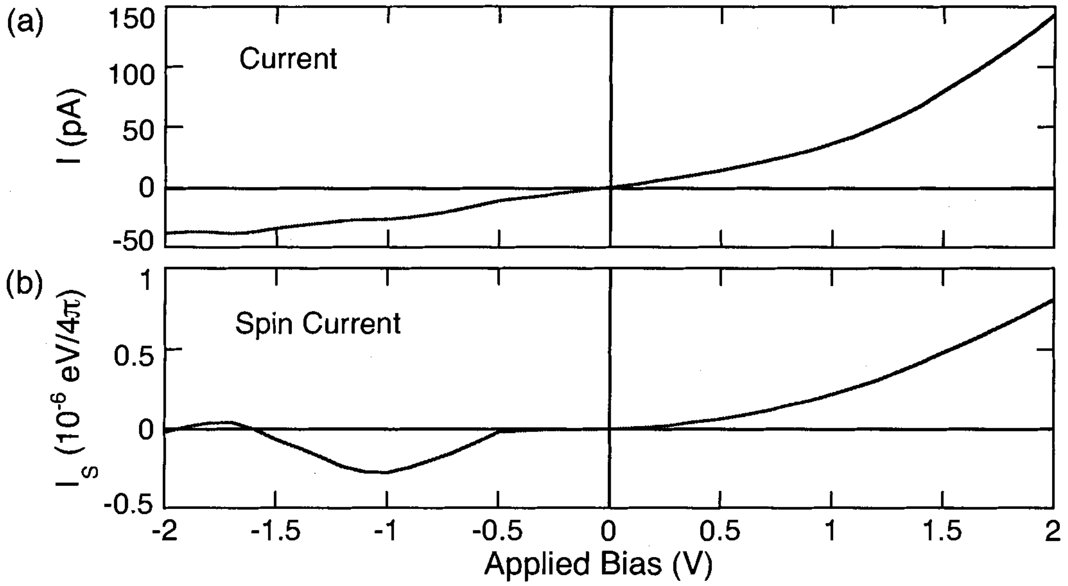

Figure 6.5: Currents for an Au/OT/Ni molecular wire. (a) Calculated current-voltage characteristic for the Au/OT/Ni wire. (b) Net spin current vs. voltage.

transmission resonances in Figure 6.2(c), the current and spin current rectification properties of Au/OT/Ni are predicted to be significantly different than for Au/OT/Fe and Pd/OT/Fe:

The total current, I, for Au/OT/Ni is displayed in Figure 6.5(a). The asymmetry in the magnitude of the current between positive and negative bias voltage is not as strong in Figure 6.5(a) as in Figure 6.3(a) or 6.4(a). This is a result of the transmission resonances associated with the Ni contact being located below the Fermi energy for both spin configurations (Fig. 4.10(b)): As they are located similarly to the resonance for Au/ODT/Au in Figure 6.2(b) (though they are smaller in magnitude), the effective asymmetry between the source and drain contacts is reduced relative to the Au/molecule/Fe systems resulting also in a reduction of the strength of the charge current rectification. For the same reason, as is evident from Figure 6.5(b), spin current rectification is predicted to be a much less pronounced phenomenon in the Au/OT/Ni molecular wire than for either Au/OT/Fe or Pd/OT/Fe: *Weak* spin rectification is predicted to extend over a wider bias range for the Au/OT/Ni molecular wire than for the Fe junctions, and *strong* spin rectification is predicted to be largely or completely suppressed in the Au/OT/Ni wire; while slightly positive, I_S is very close to zero around $-1.75V$ in Figure 6.5(b).

6.4 Conclusions

This chapter has identified that spin current rectification in molecular wires can take two different forms consistent with thermodynamic considerations: A *weak* form in which the spin current reverses direction when the bias applied to the junction is reversed and a *strong* form in which the direction of the spin current is unchanged upon reversal of the bias. Calculations were presented for spin-dependent transport in several molecular wires in which one metal contact is non-magnetic and the other consists of Fe or Ni. Both types of spin current rectification were predicted to occur (depending on the bias voltage) in the molecular wires with Fe, and the weak form to occur for Ni contacts. The results indicate that molecular wires displaying both spin current and charge current rectification should be possible, and may find practical application as nanoscale devices that combine[5] logic and memory functions. Experimental observation and further theoretical studies of the phenomena predicted here would be of interest.

---

[5] Two-terminal logic has been shown possible with molecular rectifying devices [170, 171]. Controllable spin injection and detection are required for memory devices that are based on electron spin [36]. Thus devices combining charge and spin current rectifying properties could in principle combine logic and memory functions.

Chapter 7

Summary and Outlook

This thesis has presented a general theoretical analysis of electron transport in molecular wires with transition metal electrodes. A transport methodology suitable for studying molecular wires with transition metal electrodes was developed on the basis of Landauer theory and *ab initio* and semi-empirical considerations. The electronic current (at moderate bias) in such wires was found to be mediated by electronic states at the metal-molecule interfaces that develop as a result of the strong chemical bonding between molecular sulfur orbitals and transition metal *d*-electron orbitals; strong features in the transition metal electrode densities of states were predicted to enhance the transmission at corresponding energies. Being located mainly within the transition metal contacts and having strong transition metal *d*-orbital character, the energies of the interface states were found to track with the bias voltage applied between the contacts of the molecular wire. Hence, resonant enhancements and reductions of the current under applied bias voltage were predicted, resulting in interesting transport properties and the identification of a number of new, physically important and potentially technologically relevant molecular electronic systems.

Electron transport between iron point contacts bridged by iron atoms was investigated for a range of contact separations. Characteristic trends emerging in the transport predictions as the separation between the contacts is varied were attributed, in part, to the breaking of bonds and associated dangling bond formation resulting in spin-dependent transmission resonances. Spin-dependent transport mechanisms and device characteristics were also explored for molecular wires with ferromagnetic iron contacts, systems that had not been considered previously, either theoretically or experimentally, and bias-dependent and inverse magnetoresistance phenomena were predicted. Relatively large in magnitude and occurring at modest applied bias voltages, the negative magnetoresistance predicted here suggests that iron-molecular wires may be attractive candidates for technological applications in devices based on molecular spintronics, but operated in the negative magnetoresistance regime. Spin-dependent transport was also studied for an asymmetric octane-thiolate molecule bridging nickel contacts. Bias-dependent and negative magnetoresistance was again predicted, suggesting that similar trends observed in experimental data may be *intrinsic* to such molecular tunnel junctions, i.e., not dependent on the presence of impurities within the molecular film. A Julliére model for estimating the magnetoresistance, expressed in terms of *effective* spin polarizations that take into consideration the influence on transport of the metal-molecule interfaces, was introduced to reconcile the results of the quantum transport calculations with the classical theory.

A new, controllable negative differential resistance (NDR) mechanism with potential applications for molecular electronic technology was introduced for simple molecules, such as alkane-thiols, bridging palladium and platinum contacts. Potential avenues for tailoring these non-linear transport phenomena were also considered by replacing one Pd electrode with other transition metals: Integration of a Rh electrode was predicted to yield strongly enhanced negative differential resistance. The strength of the NDR and the range of bias voltage in which it occurs were found to depend strongly on both the specific transition metals used as electrodes and their crystallographic orientations. These findings raise the prospect of designing the NDR of molecular wires for nanoelectronic device applications by appropriate choice of transition metal electrodes and their surface structures. Lastly, spin current rectification in molecular wires was predicted to take two different forms consistent with thermodynamic considerations: A *weak* form in which the spin current reverses direction when the bias applied to the junction is reversed and a *strong* form in which the direction of the spin current is unchanged upon reversal of the bias. Calculations predicting spin current rectification of both types were presented for single molecules bridging several ferromagnetic and non-magnetic contacts. The results indicate that molecular wires displaying both spin current and charge current rectification should be possible, and may find practical application as nanoscale devices that combine logic and memory functions.

Further theoretical studies of the systems identified here and their associated transport phenomena are of interest. In principle, it should be possible for such studies to incorporate additional computational sophistication that permit consideration of effects such as: geometry relaxations (or reconstructions) of the metal contact surfaces, changes in the molecular wire geometry as a function of applied bias voltage, and self-consistent calculations for the potential profile (and contact-potential related fields) that include charging of molecular orbitals and charge transfer effects. However, due to the robustness of the predictions in this work to variations in phenomenological models and model parameters, the *qualitative* predictions presented in this thesis are expected to be model independent. Hence, the qualitative phenomena predicted in this thesis should be accessible to present day experimental techniques and this work is intended to stimulate experiments directed at observing them. Incorporation of additional computational sophistication may be required when attempting quantitative comparison with experiment, however, the large degree of uncertainty about the atomic interface that persists in modern molecule electronics experiments will present a major challenge to such efforts in the near term.

In conclusion, this thesis has developed a methodology and provided a thorough investigation for an emerging and potentially important subfield of molecular electronics: Molecular wires with transition metal electrodes, systems for which interest is growing. The quantitative methodology developed here has yielded a ‘big picture’ approach for the qualitative identification of the transport properties for transition metal-molecular wires that should augment the established general understanding for molecular wires with simpler gold electrodes, that is based on the broadening of molecular orbitals into transmitting states. Based on a general consideration of the densities of states (surface and bulk) of the transition metal contacts (which may differ for source and drain electrodes), their chemical interaction with the anchoring groups of the organic molecule forming the conducting bridge, and a qualitative account of finite applied bias voltage effects, qualitative trends in the current-voltage characteristics should now also be immediately identifiable for molecular wires with transition metal electrodes. Hence, the understanding developed here should be indispensable for identifying systems that may combine transition metal electrodes with the nanoscale sizes and intrinsic functionality of organic molecules for novel nanoelectronic device applications.

Appendix A

Application of Energy Shift for Non-orthogonal Bases

To obtain the procedure by which to adjust matrix elements in a non-orthogonal basis $\{|j\rangle\}$ in response to a shift in energy, consider the Schrödinger equation describing the scattering problem, $H|\Psi\rangle = E|\Psi\rangle$. A constant energy shift C may be simultaneously added and subtracted yielding

$$H|\Psi\rangle = E|\Psi\rangle + C|\Psi\rangle - C|\Psi\rangle. \tag{A.1}$$

The scattering energy E after the shift may be redefined as $E' = E + C$. Writing $|\Psi\rangle = \sum_j \Psi_j |j\rangle$ and bracketing with $\langle i|$ in the non-orthogonal basis, Eqn. (A.1) becomes the matrix equation

$$\sum_j (H_{i,j} + CS_{i,j})\Psi_j = E' \sum_j S_{i,j}\Psi_j. \tag{A.2}$$

Equation (A.2) is the matrix form of the Schrödinger equation with Hamiltonian

$$H'_{i,j} = H_{i,j} + CS_{i,j}. \tag{A.3}$$

Hence, Equation (A.3) provides the procedure by which to adjust not only diagonal matrix elements, but also off-diagonal matrix elements when the basis is non-orthogonal in response to a shift in energy by amount C.

Appendix B

Basis State Orthogonalization by Changing Hilbert Spaces

The transport formalism introduced in Section 2.8 is based on the supposition of an orthogonal basis. Thus the non-orthogonal bases employed in this thesis to model molecular wires require adjustment.

Consider the Schrödinger equation $H|\Psi\rangle = E|\Psi\rangle$ which in the tight-binding approximation introduced in Section 2.3 has the matrix form of Eqn. (2.5)

$$\sum_j H_{i,j}\Psi_j = E\sum_j S_{i,j}\Psi_j \tag{B.1}$$

where $|\Psi\rangle = \sum_j \Psi_j|j\rangle$ expressed in the non-orthogonal basis $\{|j\rangle\}$. Equation (B.1) may be rewritten as

$$\sum_j H^E_{i,j}\Psi_j = E\Psi_i \tag{B.2}$$

where

$$H^E_{i,j} = H_{i,j} - E(S_{i,j} - \delta_{i,j}). \tag{B.3}$$

Equation (B.2) now has the form of a matrix Schrödinger equation in an *orthonormal* basis. Thus it may be viewed as the matrix form of

$$H|\Psi'\rangle = E|\Psi'\rangle \tag{B.4}$$

where $|\Psi'\rangle = \sum_j \Psi_j|j)$ and $\{|j)\}$ is an orthonormal basis. Thus the effect of Equation (B.3) is to transform from a Hilbert space A in which the basis states are non-orthogonal to the

Hilbert space A' in which they are orthonormal [72, 73]. As is evident from Equation (B.2), $|\Psi'\rangle$ has the same coefficients Ψ_j as $|\Psi\rangle$. Also since E is real and $H_{i,j}$, $S_{i,j}$ and $\delta_{i,j}$ are Hermitian, $H^E_{i,j}$ must also be Hermitian.

Thus the Hamiltonian matrix elements in the orthonormal Hilbert space $H^E_{i,j} = \langle i|H^E|j\rangle$ are energy-dependent and must be evaluated at each energy iteration of the transmission spectrum calculation. The energy-dependent Hamiltonian (and coupling) matrices then replace all occurrences of the matrices in Section 2.8.

Appendix C

Green's Functions for Semi-infinite One-dimensional Leads

In addition to simplifying the expanded Lippmann-Schwinger equation and reducing computation requirements, the use of one-dimensional leads allows for analytic calculation of the Green's functions for the electrodes. Since the leads are orthogonal in α, the Green's function for the set of leads that models an electrode follows immediately from the calculation of the Green's function for a single one-dimensional semi-infinite chain on the sites occupied by $n = 1 \ldots \infty$. The lead Green's functions of the source and drain electrodes differ only in their energy parameters that depend on electrode material, applied bias and spin. Hence, their Green's functions do not differ in form.

An electron eigenstate of such a one-dimensional chain α is a sum of rightward and leftward propagating Bloch waves $|\Phi_0^\alpha(k^\alpha)\rangle = \sqrt{\frac{1}{2N}}\sum_{n=1}^{N}(e^{ink^\alpha a} - e^{-ink^\alpha a})|n,\alpha\rangle$ with eigenenergy $E_{k^\alpha} = \varepsilon^\alpha + 2\tau cos(k^\alpha a)$. The normalization factor has been included so that the states $|\Phi_0^\alpha(k^\alpha)\rangle$ are orthonormal in k^α. For a semi-infinite chain, N approaches infinity.

The matrix elements $(G_0^R)_{m,n}^\alpha = \langle m,\alpha|G_0^R|n,\alpha\rangle = \langle m,\alpha|(E - H^R + i\delta)^{-1}|n,\alpha\rangle$ are calculated by inserting complete sets of states

$$(G_0^R)_{m,n}^\alpha = \frac{1}{2N}\sum_k \langle m|\Phi_0^\alpha(k^\alpha)\rangle(E - E_{k^\alpha} + i\delta)^{-1}\langle\Phi_0^\alpha(k^\alpha)|n\rangle \tag{C.1}$$

where the orthogonality of the states $|\Phi_0^\alpha(k^\alpha)\rangle$ has been used along with the fact that they are eigenvectors of the lead Hamiltonian, $H^R|\Phi_0^\alpha(k^\alpha)\rangle = E_{k^\alpha}|\Phi_0^\alpha(k^\alpha)\rangle$.

For a semi-infinite chain $\sum_k \to \frac{L}{2\pi}\int_{-\frac{\pi}{a}}^{\frac{\pi}{a}} dk$ and upon insertion of $|\Phi_0^{\alpha}(k^{\alpha})\rangle$, Equation (C.1) becomes

$$(G_0^R)^{\alpha}_{m,n} = \frac{1}{2N}\frac{L}{2\pi}\int_{-\frac{\pi}{a}}^{\frac{\pi}{a}} dk \frac{(e^{imk^{\alpha}a} - e^{-imk^{\alpha}a})(e^{-ink^{\alpha}a} - e^{ink^{\alpha}a})}{E - E_{k^{\alpha}} + i\delta} \tag{C.2}$$

where $L = Na$. Upon substitution for $E_{k^{\alpha}}$ the contour may be closed and the integral evaluated with residue theory to yield

$$(G_0^R)^{\alpha}_{m,n} = \frac{i}{2\tau}\frac{e^{i|n-m|k_0^{\alpha}a} - e^{i|n+m|k_0^{\alpha}}a}{sin(k_0^{\alpha}a)} \tag{C.3}$$

where the pole satisfies $cos(k_0^{\alpha}a) = \frac{E-\varepsilon^{\alpha}}{2\tau}$. τ is chosen large enough so that all modes are propagating (i.e., k^{α} is real).

The Green's function is required only on sites $m = n = 1$ in the right lead and $m = n = -1$ in the left lead, thus both Green's functions have the form

$$(G_0^R)^{\alpha}_{1,1} = \frac{i}{2\tau}\frac{1 - e^{2ik_0^{\alpha}a}}{sin(k_0^{\alpha}a)} \tag{C.4}$$

differing only in their energy parameters $\varepsilon^{\alpha}, \tau$.

The group velocity of a Bloch state with energy E in channel α is given by $\frac{1}{\hbar}\frac{dE}{dk^{\alpha}}$. Thus $v_{\alpha} = -2\tau a sin(k^{\alpha}a)/\hbar$.

Appendix D

Factorization of Transmission Functions for Asymmetric Molecular Wires and Effective Spin Polarizations

An insulating molecular wire (such as an alkane-thiolate of length L bridging metal electrodes) may be modeled as a simple square tunneling barrier with width L and barrier decay constant κ (see for example Ref. [13]). For sufficiently weak coupling between the two electrodes ($e^{-\kappa L} << 1$, i.e., multiple scattering may be ignored), the probability for an electron incident from the left side of the barrier to be transmitted into the right electrode may be expressed as

$$T(E) = T_1(E)T_2(E)e^{-2\kappa L} \tag{D.1}$$

where T_1 and T_2 are the probabilities for the electron to be transmitted across the left and right metal-molecule interfaces, respectively (unequal transmission probabilities, T_1 and T_2, are included for spatially asymmetric molecular wires). However, since a molecular wire can not be constructed with a *single* metal-molecule interface, the transmission probabilities, T_1 and T_2, will be estimated here by considering two *symmetric* systems, where the metal-molecule interfaces on both sides of the barrier are identical for each of the two systems. The total transmissions in such systems may therefore be expressed as $T^L(E) = T_1(E)^2e^{-2\kappa L}$ and $T^R(E) = T_2(E)^2e^{-2\kappa L}$ (all spatial asymmetry is assumed included in the interface, i.e., in T_1 and T_2; thus both symmetric molecular wires are described with identical tunneling parameters κ and L). Rewriting Eqn. (D.1) in terms of $T^L(E)$ and $T^R(E)$ and generalizing to non-degenerate electron spin yields

$$T_{s,s'}(E,0) = [T^L_{s,s}(E,0)T^R_{s',s'}(E,0)]^{1/2} \tag{D.2}$$

where $T_{s,s'}(E)$ is the transmission through an asymmetric molecular wire for spin orientations s and s' on the source and drain respectively, and $T^L(E)$ ($T^R(E)$) is the transmission through a symmetric molecular wire created by geometrically mirroring the left (right) spatial halves of the asymmetric wire (without further geometry relaxations). The Fermi energy alignment of the contacts is the same in all three model systems, using that of the asymmetric wire as the reference. Thus Equation (D.2) relates the zero-bias transmission probability through a spatially asymmetric molecular wire to the transmission through two symmetric systems. Eqn. (D.2) has been suggested previously for the special case of symmetric molecular junctions with opposite spin orientations (anti-parallel magnetization) on the source and drain electrode [42].

Since the transmission probability for thiolated molecules bridging transition metal electrodes is dominated by interface states that track the electrochemical potentials of the respective contacts under bias, finite bias effects may be included approximately as rigid relative shifts in the zero-bias transmission probabilities:

$$T_{s,s'}(E,V) = [T^L_{s,s}(E-\frac{V}{2},0)T^R_{s',s'}(E+\frac{V}{2},0)]^{1/2}. \tag{D.3}$$

This approximation neglects the changing *strengths* of interface state transmission resonances with bias. Nevertheless it is reasonable for moderate values of applied bias and for ranges of bias that do not sample the molecular HOMO.

The current through the junction for an individual spin channel is given by Eqn. (2.1) and may thus, at zero temperature, be written approximately as

$$I(V) \sim \frac{e}{h}\int_{E_F-eV/2}^{E_F+eV/2} dE\,[T^L_{s,s}(E-\frac{V}{2},0)T^R_{s',s'}(E+\frac{V}{2},0)]^{1/2}. \tag{D.4}$$

For uncorrelated variables X and Y, $\langle XY\rangle = \langle X\rangle\langle Y\rangle$. Thus if $T^L(E-\frac{V}{2})$ and $T^R(E+\frac{V}{2})$ are not strongly correlated over the range of integration in Eqn. (D.4), Equation (D.4) may be replaced approximately with

$$I(V) \sim \frac{1}{hV}\int_{E_F-eV/2}^{E_F+eV/2} dE\,[T^L_{s,s}(E-\frac{V}{2},0)]^{1/2}\int_{E_F-eV/2}^{E_F+eV/2} dE\,[T^R_{s',s'}(E+\frac{V}{2},0)]^{1/2} \tag{D.5}$$

where the factor of $\int dE = eV$ in the denominator arises from normalization.

Therefore the current in a particular spin channel may be written as $I_{s,s'}(V) = i^Ls(V)i^R_{s'}(V)$ where

$$i^L_s(V) = \sqrt{\frac{1}{hV}} \int_{E_F-V}^{E_F} dE\,[T^L_{s,s}(E,0)]^{1/2} \tag{D.6a}$$

and

$$i^R_{s'}(V) = \sqrt{\frac{1}{hV}} \int_{E_F}^{E_F+V} dE\,[T^R_{s',s'}(E,0)]^{1/2}. \tag{D.6b}$$

$i^L_s(V)$ and $i^R_{s'}(V)$ are the bias-dependent effective currents due to the left and right metal-molecule interfaces, respectively.

Bias-dependent *effective spin polarizations*[1] at each interface may therefore be defined as

$$P^{L,R}(V) = \frac{i^{L,R}_{\uparrow}(V) - i^{L,R}_{\downarrow}(V)}{i^{L,R}_{\uparrow}(V) + i^{L,R}_{\downarrow}(V)}. \tag{D.7}$$

Substituting these definitions for spin polarizations into the Julliére Equation (3.4) recovers the definition of magnetoresistance, Eqn (3.1). Thus the partial currents are defined consistently with the magnetoresistance formulae introduced in Chapter 3.

---

[1] Effective spin polarizations have been considered previously at *zero bias* for conventional magnetic tunnel junctions [101].

Appendix E

Two-level Quantum Model of Interface State Transmission

To better understand the systematics of resonant enhancements in the transmission due to interface molecular orbitals shifting under bias (e.g., for Pd/AT4/Pd in Fig. 5.4), it is useful to consider a two-level model constructed in the basis of interface states on the source (L) and drain (R) side of the molecule. Any molecular orbital $|\Psi\rangle$ of the extended molecule can be expressed as a linear combination of orbitals on the left, $|L\rangle$, and on the right, $|R\rangle$, spatial halves of the molecule with some coupling, t_{LR}, between the two sides (consider for example an atomic orbital resolution where every atomic orbital is located either on the left or on the right side of the molecule). When the coupling, t_{LR} between the two sides is very weak[1], much smaller than the spacing between molecular orbital eigenenergies, there is little mixing by the coupling between different orbitals $|L_i\rangle$ and $|R_i\rangle$, and $|L\rangle$ and $|R\rangle$ can be considered eigenvectors of their respective isolated Hamiltonians with eigenvalues, ε_L and ε_R, respectively (a similar two-level analysis has been performed in Ref. [173]). Since the extended molecules in this thesis (e.g., for Pd/AT4/Pd) support a very large number of orbitals, the energy spacing between molecular orbitals is small and this identification of

---

[1] As the interface states are localized on the metal-molecule interface (as opposed to de-localized over the alkane carbon backbone) the magnitude of t_{LR} should reflect the effective coupling through the entire carbon backbone [172], and not just the coupling between the left and right sides due to a single C-C bond; t_{LR} should be small, representative of the coupling between the interface states on the source and drain sides of the molecular junction.

$|L\rangle$ and $|R\rangle$ is approximate. Nevertheless, for simplicity it is assumed that the coupling t_{LR} mixes one orbital $|L\rangle$ with one orbital $|R\rangle$, forming two molecular orbitals of the coupled system

$$|\Psi_{1,2}\rangle = a_{1,2}|L\rangle + b_{1,2}|R\rangle \tag{E.1}$$

where a connection may be drawn between $|L\rangle$ and a source interface molecular orbital (as in Figure 5.4(f)), and $|R\rangle$ and a drain interface molecular orbital (as in Figure 5.4(e))[2]. For energies of the interface states on the source and drain electrodes that are degenerate at zero bias and track rigidly with the source and drain electrochemical potentials under applied bias, V, the energies of the two-level states are shifted accordingly so that $\varepsilon_{L,R} = \varepsilon \pm \frac{eV}{2}$, where ε is the energy location of the interface state resonances at zero bias.

For degenerate energy levels (zero bias) the following two-level Breit-Wigner-like formula [111, 151] for the transmission can be derived from the Lippmann-Schwinger scattering Equation (2.15) and the two-level approximation of Eqn. (E.1):

$$T(E) = \frac{4\Gamma_L\Gamma_R t_{LR}^2}{|(E-\varepsilon_L+i\Gamma_L)(E-\varepsilon_R+i\Gamma_R)-t_{LR}^2|^2}. \tag{E.2}$$

Here Γ_x is the tunneling rate from the electrodes into the two-level molecule of Eqn. (E.1) and is given by $\Gamma_x = t_x^2 Im(G_x^{lead})$, where $x = L,R$ defines the left (source) or right (drain) leads respectively, G_x^{lead} is the Green's function of the source and drain leads on the lead sites coupled to the molecule and t_x is the lead-model molecule coupling parameter[3]. Γ_x provides the broadening of the transmission resonances and is associated with the lead's self-energy. For the purposes of discussion, it is treated as an empirical parameter used to reproduce the relative sharpness and shape of the interface state transmission resonances; in the physical model, Γ represents the coupling between an electronic state deep within the contacts and the interface states and depends on V, E, and details of the entire system Hamiltonian and is difficult to quantify *a priori*. At finite bias, $\varepsilon_{L,R} = \varepsilon \pm \frac{eV}{2}$, the degeneracy is lifted and Equation (E.2) is a reasonable approximation.

---

[2] At any particular bias V, one of the two energetically split levels (e.g., in Fig. 5.4) on each electrode is closer to E_F than the other, and therefore to a first approximation only the closer of the split levels is included reducing the multi-state problem to a two-level one.

[3] Equation (E.2) is exact if the molecular levels are 'renormalized'. I.e., if the term $t_x^2 Re(G_x^{lead})$ is added to $\varepsilon_{L,R}$ [111].

Together with the energy relationships of the interface state resonances (as in Figure 5.5), Equation (E.2) provides an intuitive understanding of the nature of the transmission results (as in Figure 5.4) under bias: At zero bias, the transmission resonances associated with the interface states $|L\rangle$ and $|R\rangle$ overlap, both multiplicative terms in the denominator of Equation (E.2) are small at energies near the interface states, and the transmission is enhanced ($|L\rangle$ and $|R\rangle$ are degenerate and $|\Psi\rangle$ is the molecular orbital displayed in the inset of Figure 5.4(a)). As small bias is applied, the resonances begin to part but appreciable overlap between them remains and both of these states continue to contribute coherently to the transmission. As the bias is increased further, the two resonances become well separated, only one term in the denominator of Equation (E.2) is small at *any* energy, and the transmission is no longer enhanced as negligible overlap remains between their off-resonant transmission tails; each interface state now contributes *separately* to the transmission.

Bibliography

[1] A. Aviram and M. A. Ratner, Chem. Phys. Lett. **29**, 277 (1974).

[2] C. Joachim, J. K. Gimzewski, R. R. Schlittler and C. Chavy, Phys. Rev. Lett. **74**, 2102 (1995); Science **283**, 1683 (1999).

[3] L. A. Bumm, J. J. Arnold, M. T. Cygan, T. D. Dunbar, T. P. Burgin, L. Jones II, D. L. Allara, J. M. Tour and P. S. Weiss, Science **271**, 1705 (1996).

[4] M. A. Reed, C. Zhou, C. J. Muller, T. P. Burgin and J. M. Tour, Science **278**, 252 (1997).

[5] S. Datta, W. Tian, S. Hong, R. Reifenberger, J. I. Henderson and C. P. Kubiak, Phys. Rev. Lett. **79**, 2530 (1997).

[6] Y. Xue, S. Datta, S. Hong, R. Reifenberger, J. I. Henderson and C. P. Kubiak, Phys. Rev. B **59**, R7852 (1999).

[7] J. Chen, M. A. Reed, A. M. Rawlett and J. M. Tour, Science **286**, 1550 (1999); Appl. Phys. Lett. **77**, 1224 (2000).

[8] Z. J. Donhauser, B. A. Mantooth, K. F. Kelly, L. A. Bumm, J. D. Monnell, J. J. Stapleton, D. W. Price, A. M. Rawlett, D. L. Allara, J. M. Tour and P. S. Weiss, Science **292**, 2303 (2001).

[9] D. J. Wold and C. D. Frisbie, J. Am Chem. Soc. **123**, 5549 (2001).

[10] A. M. Rawlett, T. J. Hopson, L. A. Nagahara, R. K. Tsui, G. K. Ramachandran and S. M. Lindsay, Appl. Phys. Lett. **81**, 3043 (2002).

[11] X. D. Cui, A. Primak, X. Zarate, J. Tomfohr, O. F. Sankey, A. L. Moore, T. A. Moore, D. Gust, L. A. Nagahara and S. M. Lindsay, J. Phys. Chem. **106**, 8609 (2002); Nanotechnology **13**, 5 (2002).

[12] J. G. Kushmerick, D. B. Holt, J. C. Yang, J. Naciri, M. H. Moore and R. Shashidhar, Phys. Rev. Lett. **89**, 086802 (2002).

[13] W. Wang, T. Lee and M. A. Reed, Phys. Rev. B **68**, 035416 (2003).

[14] J. R. Heath and M. A. Ratner, Phys. Today **56**, 43 (2003).

[15] A. Salomon, D. Cahen, S. Lindsay, J. Tomfohr, V. B. Engelkes and C. D. Frisbie, Adv. Mat. **15**, 1881 (2003).

[16] S. M. Lindsay, The Electrochemical Society Interface **13**, 26 (2004).

[17] M. C. Hersam and R. G. Reifenberger, MRS Bull. **29**, 285 (2004).

[18] J. Reichert, R. Ochs, D. Beckmann, H. B. Weber, M. Mayor and H. v. Löhneysen, Phys. Rev. Lett. **88**, 176804 (2002).

[19] B. Xu and N. J. Tao, Science **301**, 1221 (2003); Nano Lett. **4**, 267 (2004).

[20] T. Dadosh, Y. Gordin, R. Krahne, I. Khivrich, D. Mahalu, V. Frydman, J. Sperling, A. Yacoby and I. Bar-Joseph, Nature (London) **436**, 677 (2005).

[21] W. Wang, T. Lee. I. Kretzschmar and M. A. Reed, Nano Lett. **4**, 643 (2004).

[22] R. M. Metzger, Macromol. Symp. **212**, 63 (2004).

[23] G. Ho, J. R. Heath, M. Kondratenko, D. F. Perepichka, K. Arseneault, M. Pézolet and M. R. Bryce, Chem. Eur. J. **11**, 2914 (2005).

[24] R. Landauer, IBM J. Res. Dev. **1**, 223 (1957); Phys. Lett. **85A**, 91 (1981).

[25] E. G. Emberly and G. Kirczenow, Phys. Rev. B **58**, 10911 (1998).

[26] E. Emberly and G. Kirczenow, Nanotechnology **10**, 285 (1999).

[27] M. Di Ventra, S. T. Pantelides and N. D. Lang, Phys. Rev. Lett. **84**, 979 (2000); Chem. Phys. **281**, 189 (2002).

[28] L. E. Hall, J. R. Reimers, N. S. Hush and K. Silverbrook, J. Chem. Phys. **112**, 1510 (2000).

[29] P. Damle, A. W. Ghosh and S. Datta, Phys. Rev. B **64**, 201403 (2001); Chem. Phys. **281**, 171 (2002).

[30] E. Emberly and G. Kirczenow, Phys. Rev. Lett. **87**, 269701 (2001); Phys. Rev. B **64**, 235412 (2001).

[31] G. Kirczenow, P. G. Piva and R. A. Wolkow, Phys. Rev. B **72**, 245306 (2005).

[32] P. E. Kornilovitch, A. M. Bratkovsky and R. S. Williams, Phys. Rev. B **66**, 165436 (2002); B. Larade and A. M. Bratkovsky, Phys. Rev. B **68**, 235305 (2003); S. -C. Chang, Z. Li, C. N. Lau, B. Larade and R. S. Williams, Appl. Phys. Lett. **83**, 3198 (2003).

[33] C. P. Collier, G. Mattersteig, E. W. Wong, Y. Luo, K. Beverly, J. Sampaio, F. M. Raymo, J. F. Stoddart and J. R. Heath, Science **289**, 1172 (2000); A. H. Flood, J. F. Stoddart, D. W. Steuerman and J. R. Heath, Science **306**, 2055 (2004).

[34] S. I. Khondaker, Z. Yao, L. Cheng, J. C. Henderson, Y. Yao and J. M. Tour, Appl. Phys. Lett. **85**, 645 (2004).

[35] G. A. Prinz, Science **282**, 1660 (1998).

[36] S. A. Wolf, D. D. Awschalom, R. A. Buhrman, J. M. Daughton, S. von Molnár, M. L. Roukes, A. Y. Chtchelkanova and D. M. Treger, Science **294**, 1488 (2001).

[37] I. Zutic, J. Fabian and S. Das Sarma, Rev. Mod. Phys. **76**, 323 (2004).

[38] E. G. Emberly and G. Kirczenow, Chem. Phys. **281**, 311 (2002).

[39] M. Zwolak and M. Di Ventra, Appl. Phys. Lett. **81**, 925 (2002).

[40] R. Pati, L. Senapati, P. M. Ajayan and S. K. Nayak, Phys. Rev. B **68**, 100407(R) (2003).

[41] W. I. Babiaczyk and B. R. Bulka, J. Phys.: Condens. Matter **16**, 4001 (2004).

[42] A. R. Rocha, V. M. García-Suárez, S. W. Bailey, C. J. Lambert, J. Ferrer and S. Sanvito, Nat. Mater. **4**, 335 (2005).

[43] H. Dalgleish and G. Kirczenow, Phys. Rev. B **72**, 184407 (2005).

[44] D. Waldron, P. Haney, B. Larade, A. MacDonald and H. Guo, Phys. Rev. Lett. **96**, 166804 (2006).

[45] V. Dediu, M. Murgia, F. C. Matacotta, C. Taliani and S. Barbanera, Solid State Commun. **122**, 181 (2002).

[46] Z. H. Xiong, D. Wu, Z. V. Vardeny and J. Shi, Nature (London) **427**, 821 (2004).

[47] J. R. Petta, S. K. Slater and D. C. Ralph, Phys. Rev. Lett. **93**, 136601 (2004).

[48] H. Dalgleish and G. Kirczenow, Phys. Rev. B **72**, 155429 (2005).

[49] H. Dalgleish and G. Kirczenow, Nano Lett. **6**, 1274 (2006).

[50] H. Dalgleish and G. Kirczenow, Phys. Rev. B **73**, 245431 (2006).

[51] H. Dalgleish and G. Kirczenow, Phys. Rev. B **73**, 235436 (2006).

[52] S. Datta, *Electronic Transport in Mesoscopic Systems*, Cambridge University Press, Cambridge (1995).

[53] N. W. Ashcroft and N. D. Mermin, *Solid State Physics*, Holt, Rinehart and Winston, New York (1976).

[54] P. Hohenberg and W. Kohn, Phys. Rev. **136**, B864 (1964).

[55] W. Kohn and L. J. Sham, Phys. Rev. **140**, A113 (1965).

[56] J. Taylor, H. Guo and J. Wang, Phys. Rev. B **63**, 121104(R) (2001); Phys. Rev. B **63**, 245407 (2001).

[57] Y. Xue, S. Datta and M. A. Ratner, Chem. Phys. **281**, 151 (2002).

[58] S. -H. Ke, H. U. Baranger and W. T. Yang, Phys. Rev. B **70**, 085410 (2004).

[59] S. P. McGlynn, L. G. Vanquickenborne, M. Kinoshita and D. G. Carrol, *Introduction to Applied Quantum Chemistry*, Holt, Rinehart and Winston, New York (1972), Chaps. 2-4.

[60] M. Wolfsberg and L. Helmholtz, J. Chem. Phys. **20**, 837 (1952).

[61] G. A. Landrum and W. V. Glassey, bind (ver 3.0). bind is distributed as part of the YAeHMOP extended Hückel molecular orbital package and is freely available on the WWW at; http://sourceforge.net/projects/yaehmop/. bind incoporates numerical parameters based on the work of R. Hoffman[62].

[62] R. Hoffmann and W. N. Lipscomb, J. Chem. Phys. **36**, 2179 (1962); J. Chem. Phys. **36**, 3489 (1962); J. Chem. Phys. **37**, 2872 (1963); R. Hoffmann, J. Chem. Phys. **39**, 1397 (1963); J. Chem. Phys. **40**, 2474 (1964); J. Chem. Phys. **40**, 2480 (1964); J. Chem. Phys. **40**, 2745 (1964).

[63] J. Redinger, C. L. Fu, A. J. Freeman, U. König and P. Weinberger, Phys. Rev. B **38**, 5203 (1988).

[64] D. A. Papaconstantopoulos, *Handbook of the Band Structure of Elemental Solids*, Plenum Press, New York (1986).

[65] The Gaussian 03 package (Rev. B.05) was used with the B3PW91 density functional and the Lanl2DZ basis set.

[66] Experimental values for metal electrode work functions were obtained on the WWW at http://environmentalchemistry.com/yogi/periodic/.

[67] P. A. Derosa and J. M. Seminario, J. Phys. Chem. B **105**, 471 (2001).

[68] E. G. Emberly and G. Kirczenow, Phys. Rev. B **60**, 6028 (1999).

[69] P. L. Pernas, A. Martín-Rodero and F. Flores, Phys. Rev. B **41**, 8553 (1990).

[70] J. J. Palacios, D. Jacob and J. Fernández-Rossier, Phys. Rev. B **71**, 220403(R) (2005).

[71] M. Büttiker, Phys. Rev. B**33**, 3020 (1986).

[72] E. Emberly and G. Kirczenow, Phys. Rev. Lett. **81**, 5205 (1998).

[73] E. G. Emberly and G. Kirczenow, J. Phys.: Condens. Matter **11**, 6911 (1999).

[74] L. E. Ballentine, *Quantum Mechanics: A Modern Development*, World Scientific, Singapore, River Edge, N. J., London (1998), Chap. 16.

[75] R. Meservey, P. M. Tedrow and P. Fulde, Phys. Rev. Lett. **25**, 1270 (1970).

[76] M. Johnson and R. H. Silsbee, Phys. Rev. Lett. **55**, 1790 (1985).

[77] M. Julliére, Phys. Lett. **54A**, 225 (1975).

[78] R. Fiederling, M. Keim, G. Reuscher, W. Ossau, G. Schmidt, A. Waag and L. Molenkamp, Nature (London) **402**, 787 (1999).

[79] Y. Ohno, D. K. Young, B. Beschoten, F. Matsukura, H. Ohno and D. D. Awschalom, Nature (London) **402**, 790 (1999).

[80] G. Tatara, Y. -W. Zhao, M. Muñoz and N. Garcia, Phys. Rev. Lett. **83**, 2030 (1999).

[81] J. Velev and W. H. Butler, Phys. Rev. B **69**, 094425 (2004).

[82] A. Bagrets, N. Papanikolaou and I. Mertig, Phys. Rev. B**70**, 064410 (2004).

[83] A. R. Rocha and S. Sanvito, Phys. Rev. B **70**, 094406 (2004).

[84] H. Oshima and K. Miyano, Appl. Phys. Lett. **73**, 2203 (1998).

[85] N. Garcia, M. Muñoz and Y. -W. Zhao, Phys. Rev. Lett. **82**, 2923 (1999).

[86] T. Ono, Y. Ooka and H. Miyajima, Y. Otani, Appl. Phys. Lett. **75**, 1622 (1999).

[87] M. Viret, S. Berger, M. Gabureac, F. Ott, D. Olligs, I. Petej, J. F. Gregg, C. Fermon, G. Francinet and G. Le Goff, Phys. Rev. B **66**, 220401 (2002); Phys. Rev. B **69**, 100401 (2004).

[88] C. Untiedt, D. M. T. Dekker, D. Djukic and J. M. van Ruitenbeek, Phys. Rev. B **69**, 081401(R) (2004).

[89] M. R. Sullivan, D. A. Boehm, D. A. Ateya, S. Z. Hua and H. D. Chopra, Phys. Rev. B **71**, 024412 (2005).

[90] N. Garcia, M. Muñoz and Y. -W. Zhao, Appl. Phys. Lett. **76**, 2586 (2000).

[91] D. J. Monsma and S. S. P. Parkin, Appl. Phys. Lett. **77**, 720 (2000).

[92] J. S. Moodera and G. Mathon, J. Magn. Magn. Mater. **200**, 248 (1999).

[93] M. B. Stearns, J. Magn. Magn. Mater. **5**, 167 (1977).

[94] J. Mathon, Phys. Rev. B **56**, 11810 (1997).

[95] J. Mathon and A. Umerski, Phys. Rev. B **63**, 220403(R) (2001).

[96] W. H. Butler, X. -G. Zhang, T. C. Schultness and J. M. MacLaren, Phys. Rev. B **63**, 054416 (2001).

[97] J. Mathon, J. Phys. D: Appl. Phys. **35**, 2437 (2002).

[98] E. Y. Tsymbal, O. N. Mryasov and P. R. LeClair, J. Phys.: Condens. Matter **15**, R109 (2003).

[99] J. C. Slonczewski, Phys. Rev. B **39**, 6995 (1989).

[100] J. M. MacLaren, X. -G. Zhang and W. H. Butler, Phys. Rev. B **56**, 11827 (1997).

[101] X. -G. Zhang and W. H. Butler, J. Phys.: Condens. Matter **15**, R1603 (2003).

[102] E. Yu Tsymbal and D. G. Pettifor, J. Phys.: Condens. Matter **9**, L411 (1997).

[103] M. Sharma, S. X. Wang and J. H. Nickel, Phys. Rev. Lett. **82**, 616 (1999).

[104] J. M. De Teresa, A. Barthélémy, A. Fert, J. P. Contour, R. Lyonnet, F. Montaigne, P. Seneor and A. Vaurès, Phys. Rev. Lett. **82**, 4288 (1999).

[105] J. Moodera, J. Nowak, L. R. Kinder, P. M. Tedrow, R. J. M. van de Veerdonk, B. A. Smits, M. van Kampen, H. J. M. Swagten and W. J. M. de Jonge, Phys. Rev. Lett. **83**, 3029 (1999).

[106] P. LeClair, J. T. Kohlhepp, H. J. M. Swagten and W. J. M. de Jonge, Phys. Rev. Lett. **86**, 1066 (2001).

[107] C. Tiusan, J. Faure-Vincent, C. Bellouard, M. Hehn, E. Jouguelet and A. Schuhl, Phys. Rev. Lett. **93**, 106602 (2004).

[108] M. Klaua, D. Ullmann, J. Barthel, W. Wulfhekel, J. Kirschner, R. Urban, T. L. Monchesky, A. Enders, J. F. Cochran and B. Heinrich, Phys. Rev. B **64**, 134411 (2001).

[109] J. Mathon, A. Umerski and M. Villeret, Phys. Rev. B **55**, 14378 (1997).

[110] J. C. Cuevas, A. Levy Yeyati and A. Martín-Rodero, Phys. Rev. Letters. **80**, 1066 (1997); Phys. Rev. B **56**, 10369 (1997).

[111] J. C. Cuevas, J. Heurich, F. Pauly, W. Wenzel and G. Schön, Nanotechnology **14**, R29 (2003).

[112] P. Bruno, Phys. Rev. Lett. **83**, 2425 (1999).

[113] S. Ohnishi and A. J. Freeman, M. Weinert, Phys. Rev. B **28**, 6741 (1983).

[114] O. Šipr, M. Kosuth and H. Ebert, Phys. Rev. B **70**, 174423 (2004).

[115] S. Pleutin, H. Grabert, G. Ingold and A. Nitzan, J. Chem. Phys. **118**, 3756 (2003).

[116] L. I. Glazman and A. V. Khaetskii, Europhys. Lett. **9**, 263 (1989).

[117] E. G. Emberly and G. Kirczenow, Phys. Rev. B **61**, 5740 (2000).

[118] V. Mulica, A. E. Roitberg and M. Ratner, J. Chem. Phys. **112**, 6834 (2000).

[119] P. E. Laibinis, G. M. Whitesides, D. L. Allara, Y. T. Tao, A. N. Parikh and R. G. Nuzzo, J. Am. Chem. Soc. **113**, 7152 (1991).

[120] Y. Hu, Y. Zhu, H. Gao and H. Guo, Phys. Rev. Lett. **95**, 156803 (2005).

[121] L. Cheng, S. L. Bernasek and A. B. Bocarsly, Chem. Mater. **7**, 1807 (1995).

[122] H. Sellers, A. Ulman, Y. Shnidman and J. E. Eilers, J. Am. Chem. Soc. **115**, 9389 (1993).

[123] E. Kobayashi, Y. Terada, T. Ohashi and J. Furukawa, Polymer Journal **23**, 267 (1991).

[124] E. Y. Tsymbal, A. Sokolov, I. F. Sabirianov and B. Doudin, Phys. Rev. Lett. **90**, 186602 (2003).

[125] P. Fenter, A. Eberhardt, K. S. Liang and P. Eisenbeger, J. Chem. Phys. **106**, 1600 (1997).

[126] M. E. Castro, S. Ahkter, A. Golchet and J. M. White, Langmuir **7**, 126 (1991).

[127] D. R. Mullins, T. Tang, X. Chen, V. Shneerson, D. K. Saldin and W. T. Tysoe, Surf. Sci. **372**, 193 (1997).

[128] K. Konstadinidis, P. Zhang, R. L. Opila and D. L. Allara, Surf. Sci. **338**, 300 (1995).

[129] A. Fernandez, J. P. Espinos, A. R. Gonzalex-Elipe, M. Kerkar, P. B. J. Thompson, J. Lüdecke, G. Scragg, A. V. de Carvalho, D. P. Woodruff, M. Fernandez-Garcia and J. C. Conesa, J. Phys.: Condens. Matter **7**, 7781 (1995).

[130] T. S. Rufael, D. R. Huntley, D. R. Mullins and J. L. Gland, J. Phys. Chem. **99**, 11472 (1995); D. R. Mullins, D. R. Huntley, T. Tang, D. K. Saldin and W. T. Tysoe, Surf. Sci. **380**, 468 (1997).

[131] C. J. Fisher, D. P. Woodruff, R. G. Jones, B. C. C. Cowie and V. Formoso, Surf. Sci. **496**, 73 (2002).

[132] J. M. Seminario, C. E. De La Cruz and P. A. Derosa, J. Am. Chem. Soc. **123**, 5616 (2001).

[133] P. E. Kornilovitch and A. M. Bratkovsky, Phys. Rev. B **64**, 195413 (2001); Phys. Rev. B **67**, 115307 (2003).

[134] J. Taylor, M. Brandbyge and K. Stokbro, Phys. Rev. Lett. **89**, 138301 (2002).

[135] Y. Xue and M. A. Ratner, Phys. Rev. B **68**, 115407 (2003); Phys. Rev. B **69**, 085403 (2004).

[136] C. Kaun and H. Guo, Nano Lett. **3**, 1521 (2003).

[137] S. N. Yaliraki, M. Kemp and M. A. Ratner, J. Am. Chem. Soc. **121**, 3428 (1999).

[138] W. T. Geng, J. Nara and T. Ohno, Thin Solid Films **464-465**, 379 (2004); Appl. Phys. Lett. **85**,5992 (2004); Phys. Rev. B **72**, 125421 (2005).

[139] T. Futschek, M. Marsman and J. Hafner, J. Phys.: Condens. Matter **17**, 5927 (2005).

[140] E. R. Brown, J. R. Söderström, C. D. Parker, L. J. Mahoney, K. M. Molvar and T. C. McGill, Appl. Phys. Lett. **58**, 2291 (1991).

[141] T. P. E. Broekaert, B. Brar, J. P. A. van der Wagt, A. C. Seabaugh, F. J. Morris, T. S. Moise, E. A. Beam III and G. A. Frazier, IEEE J. Solid State Cir. **33**, 1342 (1998).

[142] R. H. Mathews, J. P. Sage, T. C. L. G. Sollner, S. D. Calawa, C. -L. Chen, L. J. Mahoney, P. A. Maki and K. M. Molvar, Proc. IEEE **87**, 596 (1999).

[143] N. Gergel, N. Majumdar, K. Keyvanfar, N. Swami, L. R. Harriott, J. C. Bean, G. Pattanaik, G. Zangari, Y. Yao and J. M. Tour, J. Vac. Sci. Technol. A **23**, 880 (2005).

[144] J. M. Seminario, A. G. Zacarias and J. M. Tour, J. Am. Chem. Soc. **120**, 3970 (1998); J. Am. Chem. Soc. **122**, 3015 (2000); J. Phys. Chem. A **105**, 791 (2001).

[145] E. G. Emberly and G. Kirczenow, Phys. Rev. B **64**, 125318 (2001).

[146] M. Di Ventra, S. T. Pantelides and N. D. Lang, Phys. Rev. Lett. **88**, 046801 (2002).

[147] J. Cornil, Y. Karzazi and J. L. Brédas, J. Am. Chem. Soc. **124**, 3516 (2002).

[148] J. Taylor, M. Brandbyge and K. Stokbro, Phys. Rev. B **68**, 121101(R), (2003).

[149] C. N. Lau, D. R. Stewart, R. S. Williams and M. Bockrath, Nano Lett. **4**, 569 (2004).

[150] L. H. Yu and D. Natelson, Nanotechnology **15**, S517 (2004).

[151] B. Larade and A. M. Bratkovsky, Phys. Rev. B **72**, 035440 (2005).

[152] J. Gaudioso, L. J. Lauhon and W. Ho, Phys. Rev. Lett. **85**, 1918 (2000).

[153] S. Lakshmi and S. K. Pati, J. Chem. Phys. **121**, 11998 (2004).

[154] M. Galperin and M. A. Ratner, A. Nitzan, Nano Lett. **5**, 125 (2005).

[155] N. D. Lang, Phys. Rev. B **55**, 9364 (1997).

[156] T. Rakshit, G. -C. Liang, A. W. Ghosh and S. Datta, Nano Lett. **4**, 1803 (2004); Phys. Rev. B **72**, 125305 (2005).

[157] V. Mujica, M. Kemp, A. Roitberg and M. Ratner, J. Chem. Phys. **104**, 7296 (1996); Chem. Phys. **281**, 147 (2002).

[158] A. Dhirani, P. -H. Lin, P. Guyot-Sionnest, R. W. Zehner and L. R. Sita, J. Chem. Phys. **106**, 5249 (1997).

[159] C. Zhou, M. R. Deshphande, M. A. Reed, L. Jones II and J. M. Tour, Appl. Phys. Lett. **71**, 611 (1997).

[160] C. Krzeminski, C. Delerue, G. Allan, D. Vuillaume and R. M. Metzger, Phys Rev. B **64**, 085405 (2001).

[161] F. Zahid, A. W. Ghosh, M. Paulsson, E. Polizzi and S. Datta, Phys. Rev. B **70**, 245317 (2004).

[162] H. Sellers, Surf. Sci. **264**, 177 (1992).

[163] S. S. Kim, Y. Kim, H. I. Kim, S. H. Lee, T. R. Lee, S. S. Perry and J. W. Rabalais, J. Chem. Phys. **109**, 9574 (1998).

[164] J. J. Lee, C. J. Fisher, C. Bittencourt, D. P. Woodruff, A. S. Y. Chan and R. G. Jones, Surf. Sci. **516**, 1 (2002).

[165] J. G. Gay, J. R. Smith, F. J. Arlinghaus and T. W. Capehart, Phys. Rev. B **23**, 1559 (1981).

[166] Y. Yourdshahyan, H. K. Zhang and A. M. Rappe, Phys. Rev. B **63**, 081405(R) (2001).

[167] Y. Yourdshahyan and A. M. Rappe, J. Chem. Phys. **117**, 825 (2002).

[168] R. E. Peierls, *Quantum Theory of Solids*, Oxford University Press, London (1956), Chap. 4.7.

[169] X. Li, J. He, J. Hihath, B. Xu, S. M. Lindsay and N. Tao, J. Am. Chem. Soc. **128**, 2135 (2006).

[170] J. C. Ellenbogen and J. C. Love, Proc. IEEE **88**, 386 (2000).

[171] R. Stadler, S. Ami, M. Forshaw, and C. Joachim, Nanotechnology **14**, 722 (2003).

[172] J. W. Evenson and M. Karplus, J. Chem. Phys. **96**, 5272 (1992).

[173] P. Delaney, M. Nolan and J. C. Greer, J. Chem. Phys. **122**, 044710 (2205).